



# LUND UNIVERSITY

## Powertrain Optimization for Electric Vehicles

Lu, Meng

2024

[Link to publication](#)

*Citation for published version (APA):*

Lu, M. (2024). *Powertrain Optimization for Electric Vehicles*. Lund University.

*Total number of authors:*

1

### General rights

Unless other specific re-use rights are stated the following general rights apply:

Copyright and moral rights for the publications made accessible in the public portal are retained by the authors and/or other copyright owners and it is a condition of accessing publications that users recognise and abide by the legal requirements associated with these rights.

- Users may download and print one copy of any publication from the public portal for the purpose of private study or research.
- You may not further distribute the material or use it for any profit-making activity or commercial gain
- You may freely distribute the URL identifying the publication in the public portal

Read more about Creative commons licenses: <https://creativecommons.org/licenses/>

### Take down policy

If you believe that this document breaches copyright please contact us providing details, and we will remove access to the work immediately and investigate your claim.

LUND UNIVERSITY

PO Box 117  
221 00 Lund  
+46 46-222 00 00

# Powertrain Optimization for Electric Vehicles



# Powertrain Optimization for Electric Vehicles

by Meng Lu



**LUND**  
UNIVERSITY

Thesis for the degree of Doctor Philosophy in Engineering  
Thesis advisors: Prof. Mats Alaküla, Dr. Gabriel Domingues  
Dr. Francisco Marquez, Dr. Avo Reinap  
Faculty opponent: Prof. Chris Gerada

To be presented, with the permission of the Faculty of Engineering of Lund University, for public criticism in  
the M:A lecture hall (M-huset, western foyer) at the Division of Industrial Electrical Engineering and  
Automation on Friday, the 18th of October 2024 at 09:00.

<b>Organization:</b> LUND UNIVERSITY Division of Industrial Electrical Engineering and Automation Box 118 SE-221 00 LUND, Sweden		<b>Document name:</b> DOCTORAL DISSERTATION	
<b>Author(s):</b> Meng Lu		<b>Date of disputation:</b> 2024-10-18	
		<b>Sponsoring organization:</b>	
<b>Title and subtitle:</b> Powertrain Optimization for Electric Vehicles			
<b>Abstract:</b> This thesis presents a comprehensive powertrain optimization methodology that effectively captures the key design trade-offs impacting vehicle performance, both within individual components and across them. The method relies on detailed performance and cost models for all the powertrain components considered, including the electrical machine, power electronics converter, and mechanical transmission. By optimizing the entire system rather than individual components, this approach is able to identify optimal powertrain solutions within a specific set of constraints. The proposed methodology has been applied to compare various machine topologies for a specific application, evaluate the advantages of platform-level versus vehicle-level powertrain optimization, and optimize 4-Wheel Drive powertrains with multiple traction machines.			
<b>Key words:</b> Electric powertrain, Optimization, Electrical machine			
Classification system and/or index terms (if any)			
Supplementary bibliographical information		<b>Language:</b> English	
ISSN and key title		ISBN: 978-91-985110-0-0 (pdf) 978-91-985110-1-7 (print)	
Recipient's notes		<b>Number of pages:</b> 166	Price
		Security classification	

I, the undersigned, being the copyright owner of the abstract of the above-mentioned dissertation, hereby grant to all reference sources permission to publish and disseminate the abstract of the above-mentioned dissertation.

Signature

Date .

# Powertrain Optimization for Electric Vehicles

by Meng Lu



**LUND**  
UNIVERSITY

Cover illustration front: A masterpiece from Yibei's painting class, the author's 6-year-old son

© Meng Lu 2024

Faculty of Engineering, Division of Industrial Electrical Engineering and Automation

ISBN: 978-91-985110-0-0 (pdf)

ISBN: 978-91-985110-1-7 (print)

CODEN: LUTEDX/(TEIE-1098)/1-166/(2024)

Printed in Sweden by Media-Tryck, Lund University

Lund 2024



Media-Tryck is a Nordic Swan Ecolabel certified provider of printed material. Read more about our environmental work at [www.mediatryck.lu.se](http://www.mediatryck.lu.se)

**MADE IN SWEDEN** 

*Dedicated to my beloved wife and son*





# Contents

Acknowledgements.....	i
Abbreviations .....	iii
Popular summary in English.....	x
Contribution Statement .....	xi
<b>Chapter 1 Introduction.....</b>	<b>1</b>
1.1. Background .....	1
1.2. Objectives of the Thesis .....	5
1.3. Contributions .....	6
1.4. Thesis Layout.....	6
1.5. List of publications.....	7
<b>Chapter 2 Electrical Machine Design .....</b>	<b>9</b>
2.1 EM Modelling Settings .....	11
2.1.1 Geometry Parametrization .....	11
2.1.2 Winding design .....	15
2.2 Modelling of PMSM and PMaSynRM.....	18
2.2.1. FE simulation initialization .....	18
2.2.2. Loss estimation .....	19
2.2.3. Performance evaluation.....	28
2.3 Modelling of IM .....	30
2.3.1. FE simulation initialization .....	30
2.3.2. Loss estimation .....	31
2.3.3. Performance evaluation.....	31
2.4 EM Scaling .....	32
2.5 PM demagnetization analysis .....	36
2.6 EM performance validation.....	40
2.7 EM thermal model.....	42
2.6.1. Thermal model for PM machines.....	43
2.6.2. Thermal model for IM.....	44
2.8 EM Cost model .....	45
<b>Chapter 3 Transmission and PEC Modeling.....</b>	<b>51</b>

3.1.	Inverter design .....	51
3.1.1	Electro-thermal model .....	52
3.1.2	Cost Model.....	54
3.2.	Transmission design.....	55
3.2.1.	MT Modelling.....	56
3.2.2.	Desired gear ratio determination .....	59
3.2.3.	Cost model .....	60
<b>Chapter 4</b>	<b>Optimization Methodology .....</b>	<b>63</b>
4.1.	Optimization inputs .....	65
4.1.1.	Powertrain configuration .....	65
4.1.2.	EV requirements.....	67
4.1.3.	EM database .....	69
4.2.	Objective function .....	71
4.2.1.	Powertrain cost .....	72
4.2.2.	Operating cost .....	72
4.3.	Optimizer .....	74
<b>Chapter 5</b>	<b>Comparison analysis for PMSM, PMSynRM and IM from system level</b>	<b>77</b>
5.1.	Vehicle Specifications and optimization targets .....	77
5.2.	Results .....	80
5.3.1.	Optimization results for all types of EMs .....	80
5.3.2.	Demagnetization analysis for PMSynRM .....	91
5.3.	Conclusions .....	96
<b>Chapter 6</b>	<b>Platform-based System Optimization .....</b>	<b>97</b>
6.1.	Optimization process .....	98
6.2.	Vehicle specifications for EV platform .....	99
6.3.	Objective function .....	102
6.4.	Results .....	103
<b>Chapter 7</b>	<b>4WD optimization.....</b>	<b>109</b>
7.1.	Vehicle configuration.....	110
7.2.	Methodology .....	112
7.3.	Results .....	115
<b>Chapter 8</b>	<b>Conclusion and Future work.....</b>	<b>121</b>
8.1.	Conclusion .....	121

8.2. Future work.....	122
<b>Appendice .....</b>	<b>125</b>
<b>Appendix A .....</b>	<b>127</b>
<b>Reference .....</b>	<b>131</b>



# Acknowledgements

Writing the acknowledgment section of my PhD thesis has evoked a bit of anxiety for me. I worry that my command of language may not convey my deep gratitude to those who have accompanied, assisted, and encouraged me throughout these years.

First and foremost, I would like to express my deepest gratitude to my supervisor, Mats Alaküla, for the invaluable opportunity for me to continue exploring the electrification field. The memory of receiving the invitation for an on-site interview in Lund over five years ago remains in my heart. Throughout these years, Mats has provided consistent guidance and comprehensive support, both in research direction and technical details. His support extended beyond the scope of science, particularly during the challenging time when my child was born prematurely due to my wife's pre-eclampsia. The firm support from Mats helped us get through that difficult time.

I am also grateful to my co-supervisors, Gabriel Domingues, Francisco Márquez, and Avo Reinap. Gabriel, thank you for the 20% of your time at IEA, though I suspect I may have taken more than 10%. Your insightful discussions about the automotive industry have provided me with a broader view on this area. Fran, the regular supervision meeting with you were always enlightening, and your in-depth knowledge of electrical machines inspired and helped me a lot. Avo, whenever I encountered a problem that had troubled me for a long time, I would step out, turn right (when we were in the KC building), and bring the problems to you. and then get something valuable. Your answers, though not always straightforward solutions, consistently provided valuable insights that ultimately resolved my issues.

I would also like to thank Ulf Jeppsson and Ulrika Westerdahl for their help in cleaning up the messes I made. Ulf, your birthday emails are heartwarming, even though I celebrate according to the lunar calendar—two birthdays are always welcome!

Furthermore, I would like to thank Getachew Darge, Olof Samuelsson, Carina Lindström, Gunnar Lindstedt, Henriette Weibull, Maira Einarsson, who have all provided excellent support throughout my journey.

To my colleagues in the 'aquarium' - Samuel, Hannes and Leonardo, I'm really enjoying every time talking with you guys. I also extend my gratitude to all my colleagues at IEA for their generous sharing of their knowledge and life. Akanksha, Huan, Philip, Anton, David, Alice, Edvin, Martin, Mattias, Max, Imran, Hamoun, Ramesh, Gabriel Malmer, Amir, the knowledge you've generously shared and the moments we've enjoyed together will be cherished memories, thank you all! It's hard to believe that my time at IEA is coming to an

end. As someone without many local connections, I've come to see you not just as colleagues but as friends.

I would like to express my gratitude to our partners at BorgWarner, Aleksandar Mateski, and Gabriel Turesson, for their valuable contributions. I am also thankful to Pontus Fyhr, whose contributions have greatly enriched my research.

A big thank you to my friends in Uppsala and Lund, whose company during weekend dinners and conversations helped me get through the long winters, especially the first one during the COVID.

Last but certainly not least, the special thanks go to my wife, Ying Guo (郭影), who has stood by my side since our undergraduate days and supported me unwaveringly throughout this journey. To my son, Yibei (亦北), who makes our life meaningful: We love you! I am also deeply grateful to the doctors and nurses in Lund and Malmö for their exceptional care and support during the birth of our son.

I reserve my final thanks for Lund, this charming southern town that has become our second home. Every time I return from China or a vacation, I feel a sense of peace in my heart.

Meng Lu / 鹿猛

Lund, Sweden, 2024

# Abbreviations

2D	Two-dimension
2WD	Two-Wheel Drive
4WD	Four Wheel Drive
AC	Alternating current
ASC	Active short circuit
BEV	Battery electric vehicle
DC	Direct current
EESM	Electrically excited synchronous machine
EV	Electric vehicle
EM	Electrical machine
EMF	The electro-motive force
FEM	Finite element method
IM	Induction machine
IEA	Industrial Electrical Engineering and Automation
KPI	Key performance indicator
MT	Mechanical transmission
MTPA	Maximum torque per ampere
NVH	Noise, Vibration, and Harshness
OEM	Original equipment manufacturer
PEC	Power electronics controller
PHEV	Plug-in hybrid electric vehicle
PMSM	Permanent magnet synchronous machine
PMaSynRM	Permanent magnet assisted synchronous reluctance machine
PSO	Particle swarm optimization



R&D	Research and development
SRM	Switched reluctance machine
$\alpha$	The temperature coefficient of resistivity
$\alpha_1$	The power rating factor for the 4WD system
$\alpha_2$	The torque distribution factor between two powertrains
$\beta$	Magnet placement angle
$\theta$	Slope angle of the road
$\rho_0$	The copper resistivity at temperature $T_0$
$\rho_{Cu}$	The copper resistivity
$\rho$	The density of the transmission gears
$\sigma$	The copper winding conductivity
$\sigma_{yield}$	The yield strength of the laminations
$\omega_e$	The electrical angular speed of the flux
$\omega$	The synchronous speed
$\omega_r$	The rotor mechanical speed
$\omega_s$	The slip frequency
$\varphi_m$	Flux linkage for permanent magnet
$\omega_{inertia}$	The inertia factor of PSO
$A_{bar}$	Ratio between the total area of rotor bars and the rotor area
$A_s$	Area of single slot
$A_v$	The frontal area of the vehicle
<b><math>B</math></b>	The flux density
$\hat{B}$	The magnitude of the flux density
$B_m$	The amplitude of the m-order harmonics for the leakage flux
$C_1$	The cognitive coefficient

$C_2$	The social coefficient
$C_r$	The rolling resistance coefficient
$C_d$	The air drag coefficient
$C_{PT}$	The powertrain cost
$C_{EM}$	The EM cost
$C_{PEC}$	The PEC cost
$C_{MT}$	The MT cost
$C_{RD\_tot}$	The total R&D cost for one EM product
$C_{OP}$	The operating cost
$c_{hyst}$	Coefficient for the hysteresis losses
$c_{eddy}$	Coefficient for the eddy current losses
$c_{ex}$	Coefficient for the excess losses
$d_{mi}$	Distance between magnet edge and rotor inner radius
$d_{pn}$	Distance between magnet edges of the neighbour pole magnets
$d_{rib}$	The width of the iron ribs
$EC$	The energy consumption over the drive cycle
$E_{ref}$	The energy losses from product datasheet of semiconductor
$F_{\varphi\_RWD}$	The adhesive force for RWD EV
$F_{\varphi\_FWD}$	The adhesive force for FWD EV
$F_{\varphi\_4WD}$	The adhesive force for 4WD EV
$e_1$	The volume coefficient of pinion
$e_2$	The volume coefficient of wheel
$f$	The EM electrical frequency
$f_m$	The frequency of the m-order harmonics of the magnetic field
$f_{sw}$	The switching frequency of PEC
$G$	The thermal conductivity matrix
$g$	The gravity

$gr$	The desired gear ratio for the whole transmission gear,
$gr_n$	The gear ratio for each stage
$h$	The height of each conductor
$h_{tt}$	Height of tooth tip
$h_{pm}$	Height of the magnets
$h_{cg}$	The height of the centroid of the vehicle
$ins$	The insulation thickness
$i_{eddy}$	The eddy current induced in the winding conductor
$i_d$	Current in direct axis
$i_q$	Current in quadrature axis
$I_a$	Current for phase A
$I_b$	Current for phase B
$I_c$	Current for phase C
$I_r$	The induced current in the rotor bars
$J_{ini}$	Initial current density in slot
$k_a$	The ratio between length of scaled machine and the base machine
$k_{ov}$	The ratio between peak and nominal current.
$k_{0n}$	The allowable load intensity factor
$k_f$	Winding filling factor
$k(x, N)$	The cost of a part of the EM under certain manufacturing stage
$K_A$	The investment cost in tooling
$K_B$	The cost of material
$K_{CP}$	The cost during production
$K_{CS}$	The cost during standstill
$K_D$	The wage cost
$K_{iron}$	Factor to adjust $W_{yk}$ and $W_{th}$
$k_{0n}$	The allowable load intensity factor

$K_v$	The voltage compensation constant
$l_{ag}$	Air gap length
$L_1$	Relative magnets position
$L_d$	Inductance in direct axis
$L_q$	Inductance in quadrature axis
$l_{act}$	The active length of the stator
$l_{end}$	The length of end turns
$l_w$	The wheelbase
$l_f$	The length between the centroid and front wheel
$l_r$	The length between the centroid and rear wheel
$m_{act}$	The total mass of materials between the magnets and the airgap
$m_u$	The friction coefficient
$M_v$	The total mass of the vehicle
$M_{tot}$	The total mass of the transmission
$n_{max,EM}$	The maximum speed of EM
$n_{max,wheel}$	The maximum speed on wheel side
$n_{hl}$	Number of magnet layers
$N$	the number of EM units
$N_{bar}$	Number of rotor bars
$N_c$	The number of conductors per slot
$N_p$	Number of poles
$N_{pp}$	The number of parallel paths
$N_t$	The number of turns
$p$	The number of pole pairs
$P$	The losses of each node
$P_b$	The bearing loaded losses of MT
$P_{cu\_AC}$	The AC copper losses for hairpin winding

$P_{cu\_bar}$	The copper losses of the rotor bars
$P_{cu\_er}$	The end ring losses
$P_{sw}$	The switching losses for PEC
$P_{gr}$	The mesh power losses of MT
$P_{GW1}$	The windage losses of MT
$P_{GW2}$	The oil churning losses of MT
$P_{Fe}$	The iron losses
$P_{max}$	The maximum power of EM
$q$	The number of slots per pole per phase
$q_Q$	the quality loss
$q_s$	The standstill fraction
$r_{act}$	The distance to the center of gravity of $m_{act}$
$r_{ce}$	The electrical resistance for the power modules
$r_{ro}$	Rotor outer radius
$r_{ri}$	Rotor inner radius
$r_{so}$	Stator outer radius
$R_{s\_DC}$	The stator DC resistance
$R_{AC}$	The stator AC resistance
$s$	The slip
$t_0$	The cycle time per operation
$t_{ACC\_4WD\_lim}$	The limit for acceleration time for 4WD EV
$t_{ov}$	The overloading time of EM
$\Delta T$	The temperature rise of each node
$T_0$	Fixed reference temperature
$T_c$	The temperature compensation constant
$T_j$	The operating temperature of the semiconductor
$T_{p,n}$	The allowable torque on the shaft

$T_{max,wheel}$	The maximum torque on wheel side
$T_{max,EM}$	The maximum torque of EM
$T_{PM}$	Total torque of the PM machines
$T_{rel}$	Reluctance torque
$T_{mag}$	Magnet torque
$T_{wind}$	The temperature of the winding
$T_{ref}$	Reference temperature of the winding
$T_r$	The reference temperature at which the semiconductor energy losses are defined in the datasheet
$U_{smax}$	The maximum induced voltage
$U_{DC}$	The DC-link voltage
$V_{cc}$	The blocking voltage of the semiconductor
$V_{ref}$	The reference voltage at which the semiconductor energy losses are defined in the datasheet
$w$	The width of each conductor
$W_{so}$	Width of slot opening
$W_{th}$	Width of the narrowest stator tooth
$W_{yk}$	Width of the stator yoke

## Popular summary in English

The ongoing transition towards electrification in the automotive industry is clear and accelerating in most of the regions of the world. The electric powertrain, which propels the electric vehicle, plays a vital role in this wave of electrification. The powertrain's primary function is the conversion of electrical energy into mechanical energy. The powertrain significantly influences the key attributes of electric vehicles, including performance, overall system efficiency, and sustainability. For instance, powertrain design impacts the utilization of rare-earth materials for vehicles who utilize PMSM and metals such as lithium, cobalt, and nickel for batteries, whose extraction poses environmental concerns.

However, the electric powertrain encounters numerous demands and challenges from various perspectives, making its design a complex and multidisciplinary task. This complexity arises from the necessity to integrate expertise in mechanical engineering, electromagnetics, thermal management, and cost analysis.

In most cases, designing and optimizing powertrain components in isolation and subsequently integrating them does not typically yield an optimal powertrain design. The interactions between components are often underestimated. For example, the energy consumption of an EV is significantly influenced by the efficiency of all powertrain components. Consequently, additional expenditure on more efficient electrical machines or inverters can result in a more competitive powertrain design. However, due to the system's complexity, it is infeasible for an expert to consider all relevant correlations and achieve a better trade-off among all the key performance indicators (KPI) for a holistic design that meets vehicle-level requirements. The optimal powertrain design should balance diverse and sometimes conflicting considerations. Designers should navigate these trade-offs to identify optimal solutions.

Therefore, a system-level powertrain optimization methodology is imperative to achieve the optimal powertrain design for a selected application with certain constraints.

This thesis undertakes a comprehensive exploration aimed at addressing key issues in powertrain system design by modelling all primary components, including the EM, PEC, and transmission. This approach seeks to identify and capture as many influential factors as possible to evaluate how each affects the powertrain performance. By optimizing the powertrain system rather than individual components, it is feasible to achieve a better powertrain solution within given constraints.

# Contribution Statement

Dissertation title: Powertrain optimization for electric vehicles

Author: Meng Lu

Affiliation: Division of Industrial Electrical Engineering and Automation (IEA), Faculty of Engineering (LTH), Lund University, Sweden

Defense date: 2024-10-18

Listed below are all the publications of the PhD work, followed by a description of the contributions from the other authors:

1. **Electric Drivetrain Optimization for a Commercial Fleet with Different Degrees of Electrical Machine Commonality**

M. Lu, G. Domingues-Olavarria, F. J. Márquez-Fernández, P. Fyhr and M. Alaküla

Energies 2021, 14, 2989.

Author Contributions: Conceptualization, M.A.; Data curation, M.A.; Methodology, M.L., G.D.-O., F.J.M.-F., P.F. and M.A.; Project administration, G.D.-O.; Software, M.L., G.D.-O. and P.F.; Supervision, G.D.-O., F.J.M.-F. and M.A.; Visualization, M.L.; Writing—original draft, M.L.; Writing—review & editing, G.D.-O., F.J.M.-F. and M.A. All authors have read and agreed to the published version of the manuscript.

2. **Optimization of Induction Machine Design for Electric Vehicle Powertrain**

M. Lu, G. Domingues-Olavarria, F. J. Márquez-Fernández, H. Bydén and M. Alaküla

IEEE International Electric Machines & Drives Conference (IEMDC), San Francisco, USA, 2023

Author Contributions: Conceptualization, M.L.; Data curation, M.L.; Methodology, M.L., G.D.-O., F.J.M.-F., H.B. and M.A.; Software, M.L. and H.B.; Supervision, G.D.-O., F.J.M.-F. and M.A.; Visualization, M.L.; Writing—original draft, M.L.; Writing—review & editing, G.D.-O., F.J.M.-F., H.B. and M.A. All authors have read and agreed to the published version of the manuscript.

3. **Optimization of Powertrain Platform for Electric Passenger Vehicles**

M. Lu, G. Domingues-Olavarria, H. Bydén, M. Aleksandar and M. Alaküla



IEEE Transportation Electrification Conference & Expo (ITEC), Detroit, MI, USA, 2023

Author Contributions: Conceptualization, M.L. and G.D.-O.; Data curation, M.L. and M.Alek.; Methodology, M.L., G.D.-O. and M.A.; Software, M.L. and H.B.; Supervision, G.D.-O. and M.A.; Visualization, M.L.; Writing—original draft, M.L.; Writing—review & editing, G.D.-O., H.B., M.Alek. and M.A. All authors have read and agreed to the published version of the manuscript.

**4. Comparison of PMSM versus PMA-SynRM and IM from an Optimized Electric Vehicle Powertrain Perspective**

M. Lu, G. Domingues-Olavarria and M. Alakula

26th International Conference on Electrical Machines and Systems (ICEMS), Zhuhai, China, 2023

Author Contributions: Conceptualization, M.L. and G.D.-O.; Data curation, M.L.; Methodology, M.L., G.D.-O. and M.A.; Software, M.L.; Supervision, G.D.-O. and M.A.; Visualization, M.L.; Writing—original draft, M.L.; Writing—review & editing, G.D.-O. and M.A. All authors have read and agreed to the published version of the manuscript.

**5. Platform-based Powertrain Optimization for Electric Passenger Vehicles**

M. Lu, G. Domingues-Olavarria, H. Byden, and M. Alakula

IEEE Transactions on Transportation Electrification, submitted.

Author Contributions: Conceptualization, M.L. and G.D.-O.; Data curation, M.L.; Methodology, M.L., G.D.-O. and M.A.; Software, M.L. and H.B.; Supervision, G.D.-O. and M.A.; Visualization, M.L.; Writing—original draft, M.L.; Writing—review & editing, G.D.-O., H.B. and M.A. All authors have read and agreed to the manuscript.

**6. Holistic Optimization of Electric Powertrains**

Domingues, G., Turesson, G., Lu, M. et al.

MTZ Worldwide, 84, 16–25 (2023)

Author Contributions: Methodology, M.L. and G.D.-O.; Software, M.L. and G.D.-O.; Writing—review & editing, M.L. and T.G. All authors have read and agreed to the published version of the manuscript.

7. **Impacts of using different semiconductor technologies on drivetrain optimization**

H. Bydén, G. Domingues-Olavarria, M. Lu, and M. Alaküla  
ESARS-ITEC 2024, submitted

Author Contributions: Methodology, M.L. and H.B.; Software, H.B.; M.L. and G.D.-O.; Writing—review & editing, M.L., G.D.-O. and M.A.; All authors have read and agreed to the manuscript.



# Chapter 1 Introduction

## 1.1. Background

The ongoing shift in the automotive industry towards electrification is evident, with notable acceleration observed in regions such as Europe and China. According to [1], a total of 6 million new battery electric vehicles (BEVs) and plug-in hybrid electric vehicles (PHEVs) were delivered during the first half of 2023, an increase of 40% compared to the first half year of 2022. Of these, 4.27 million were BEVs and 1.76 million were PHEVs. A detailed examination of regional trends indicates a 37% increase in EV sales in China for the first half of 2023, compared to 82% in 2022 vs 2021. Sales in Europe were up 28% in 2023 compared to just 15% in 2022. Additionally, the market in the USA and Canada experienced a 50% increase in EV sales compared to the previous year.

The market share of EVs has shown a consistent increase across all major markets. In the first half of 2023, BEVs accounted for 10%, and PHEVs for 4.1%, cumulatively comprising 14.1% of global light vehicle sales. Norway had the highest market share of EVs in the first 6 months of 2023, 75% for BEVs and 6% for PHEVs. China had 30.5%, Europe 19.7% and USA 8.7%. For the full year of 2023, sales of up to 14 million EVs are expected all over the world, a growth of 33% over 2022. By the end of 2023, 40 million EVs in operation are expected. When it comes to the future, according to [2][3], it is suggested that the global EV stock will reach nearly 240 to 380 million, accounting for over 10% of the total vehicle stock and representing over 35%-60% of all vehicle sales in 2030.

The automotive industry has reached a consensus regarding the irreversibility of electrification and has intensified its investments in this area. This shift is driven by several key factors.

Policy consideration is one of the primary driving forces. Facing the looming threat of climate change, governmental authorities all over the world have implemented a series of policy measures aimed at supporting vehicle electrification [4][5]. The EU has the strongest regulatory pressure and shows the highest ambition to phase out the sale of petroleum fuel based internal combustion engine vehicles by 2035 [6].

Technological progress for EVs is another driving force behind the rapid development of the electric vehicle industry. It is well known that battery technology has always been crucial for electric vehicles. The energy density of batteries has been consistently on the rise, while costs have gradually decreased [7] [8]. These improvements have led to extended electric vehicle range and increased price competitiveness.

At the same time, the rapid development of the EV market has geared up the expansion of charging infrastructure [9]. This development is critical, as the widespread construction of additional charging stations has markedly enhanced the convenience of charging EVs. Such infrastructural advancements have played a pivotal role in alleviating the ‘range anxiety’ among consumers.

The evolution of electric vehicle research and development (R&D) has been another noteworthy phenomenon in recent years. Initially, EVs were commonly developed as retrofits on existing gasoline vehicle platforms. However, a significant shift has occurred in the industry, with all original equipment manufacturers (OEMs) now transitioning to dedicated electric vehicle platforms. This shift has not only enhanced the performance of EVs but has also contributed to their increased price competitiveness in the automotive market.

While the advancements in battery technology and other aforementioned aspects are pivotal for the development of electric vehicles, the role of the electric powertrain, which propels the EV, is equally critical in the ongoing wave of electrification. The powertrain converts electrical energy into mechanical energy. This system significantly influences the key attributes of electric vehicles such as performance, overall system efficiency and sustainability. For example, the powertrain design affects the resource use of rare-earth material for electrical machines and lithium, cobalt, nickel, and other metals for batteries whose extraction have environmental impacts.

As it is shown in Figure 1.1, the electric powertrain confronts numerous demands and challenges from various perspectives. One potential strategy to address some of these challenges is through the downsizing of the powertrain system [10]. Downsizing offers several advantages. Firstly, a smaller electric powertrain system enables more efficient use of space. This aspect is particularly crucial in the context of EV design, where spatial flexibility is a key consideration. Additionally, a smaller powertrain requires fewer materials and resources, which can significantly contribute to reducing the overall manufacturing costs and environmental impact of electric vehicles. This approach, while offering substantial benefits, must be carefully balanced against potential impacts, such as system thermal management.

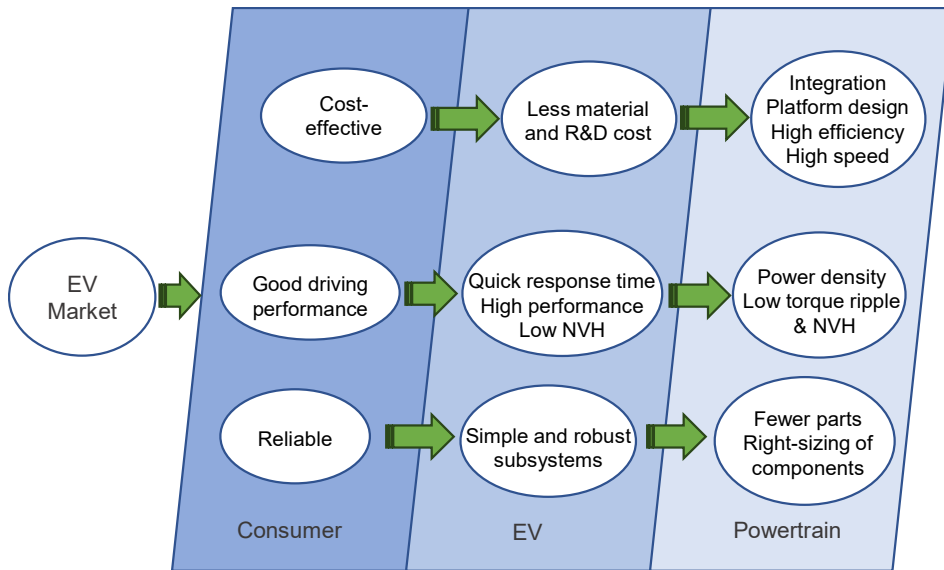


**Figure 1.1** Trends of electric powertrain technology

Another attempt to address these challenges is the high-speed electrical machine (EM). Increasing the maximum mechanical speed of the EM can enable it to deliver equivalent power at a reduced torque. This adjustment potentially allows for a reduction in the electrical machine size. However, this technique requires careful consideration of associated trade-offs. One significant consequence of higher machine speeds is the increase in speed-dependent losses and mechanical stresses. Additionally, a higher maximum speed of EM requires a higher switching frequency in the power electronics converter (PEC), leading to increased losses within the PEC. The higher EM speed also brings higher transmission ratios and increased mechanical transmission (MT) complexity and losses on the transmission side. These factors must be carefully weighed in the design and optimization for EV powertrains.

In the realm of electric powertrain development, there is also a significant emphasis on improving the efficiency of the powertrain. This emphasis has led to the widespread adoption of permanent magnet synchronous machines (PMSMs) with rare earth magnets [11], which is the predominant choice in the automotive industry. Concurrently, the introduction of new winding techniques, such as hairpin windings, which improves the winding filling factor, has led to reduced copper losses and higher torque density. However, these advancements are not without their challenges. One notable issue is the increase of AC (alternating current) copper losses, particularly at high operational speeds, alongside the increase of manufacturing costs [12].

While numerous other innovative techniques in the field remain unmentioned, it is clear that the design of the electric powertrain is a complex and multidisciplinary task. This complexity stems from the requirements to integrate various fields of expertise, including mechanical engineering, electromagnetics, thermal management, and cost analysis. The optimal design of electric powertrains, therefore, requires a holistic approach that carefully balances these diverse and sometimes conflicting considerations. For example, the selection of EM topology and geometry, material use, winding layout, PEC semiconductor selection and design, transmission gear design and gear ratio selection, etc. will contribute to the system performance and system cost-effectiveness. Designers must carefully navigate these trade-offs to arrive at the optimal solutions.

To meet this challenge, powertrain optimization for EVs has emerged as a significant area of research. Many efforts have focused on improving the modelling and scalability of different powertrain components. For example, a methodology to rapidly estimate the performance of a scaled EM by varying the axial length, outer radius and number of turns of a base EM design is introduced in [13][14][15]. The scaling of EM allows for quick performance evaluations, making it feasible to conduct powertrain optimization.

Moreover, the performance of PEC is equally crucial in the powertrain optimization. In [16], an analytical model for calculating losses in IGBT-based inverters has been developed and integrated into system-level optimization. In [17], a scalable electro-thermal model for PEC is implemented to estimate the losses and optimize semiconductor size.

Mechanical transmission also plays a vital role in determining the efficiency and performance of the electric powertrain. In [18], the impact of the MT topology on powertrain overall efficiency is carried out. Approach to size the gears and estimate the losses of gears and bearings is discussed in [19]. These studies highlight the MT's influence on the overall powertrain performance.

As mentioned before, cost estimation is another critical component of powertrain optimization, as it directly impacts the feasibility and scalability of EV technologies. In [20], a detailed cost model for EM considering the material cost and the cost occurred during the manufacturing process is implemented. Additionally, a model has been proposed to estimate the overall powertrain cost using fixed material prices and empirical formulas, resulting in computationally efficient models [21].

In this research, the work is built upon the work done by [22], where the modeling of PMSM with traditional winding configurations is explored. This thesis extends this foundation by incorporating hairpin winding in PMSM and conducting a detailed evaluation of AC losses. Furthermore, the estimation of iron losses with taking harmonic into account is performed. In addition to PMSM modeling, this thesis also encompasses the modeling of induction machine (IM) and Permanent Magnet-assisted Synchronous

Reluctance Machine (PMaSynRM), with a particular focus on the demagnetization of ferrite magnets. The inverter model, which is detailed in [17], has been integrated into the powertrain system as part of this work. Furthermore, the transmission model designed by [19] is incorporated into the powertrain optimization process, facilitating the determination of an optimal gear ratio to minimize energy consumption.

This thesis presents a comprehensive powertrain optimization methodology that effectively captures the key design trade-offs impacting vehicle performance, both within individual components and across them. The method relies on detailed performance and cost models for all the powertrain components considered, including the electrical machine, power electronics converter, and mechanical transmission. By optimizing the entire system rather than individual components, this approach is able to identify optimal powertrain solutions within a specific set of constraints. The proposed methodology has been applied to compare various machine topologies for a specific application, evaluate the advantages of platform-level versus vehicle-level powertrain optimization, and optimize 4-Wheel Drive (4WD) powertrains with multiple traction machines.

## 1.2. Objectives of the Thesis

Based on the overview in section 1.1, the following research questions motivate the work in this thesis:

- What are the most relevant design trade-offs affecting powertrain performance and cost?
- How can these trade-offs be captured, and their effects considered in the design of electric powertrains for different applications?

The main objectives of this thesis are:

- Optimize powertrains of electric road vehicles in terms of both upfront and operating costs, considering most relevant design parameters.
- Analyze and compare the suitability of three types of EMs from an optimized powertrain perspective.
- Optimize the system level design and a suitable control for a 4-Wheel Drive (4WD) EV comprised of two powertrains.
- Develop an optimization methodology for an electric powertrain platform and explore the benefits of system commonality.



## 1.3. Contributions

The main contributions of this thesis are:

- Further development of the powertrain optimization framework introduced in [22], integrating cost and performance (electromagnetic and thermal) models for IMs and PMaSynRMs.
- A detailed comparison of PMSM, IM and PMaSynRM for the optimization of a representative EV powertrain, in terms of investment and operational cost.
- A design and optimization methodology for 4WD EVs comprising several traction machines.
- A platform-based powertrain design and optimization methodology to quantify the system benefits and drawbacks of standardization across different vehicle segments.

## 1.4. Thesis Layout

This thesis has eight chapters.

Chapter 1 provides an overview of the current state of the EV market, highlighting the critical role and design challenges of the electric powertrain. It also outlines the objectives and significant contributions of this thesis.

Chapter 2 introduces the method to generate an EM database with a parametrized geometry space. Then, the electromagnetic performance evaluation, thermal analysis, scaling methods and cost estimation for the studied EMs are discussed.

Chapter 3 provides an overview of the design process for the mechanical transmission and the power electronic converter.

Chapter 4 illustrates the system optimization methodology for electric powertrains , focusing on system efficiency and powertrain cost considerations.

Chapter 5 presents the comparison study for PMSM, PMaSynRM and IM from an optimized powertrain perspective.

Chapter 6 explores platform-based powertrain optimization for electric passenger cars.

Chapter 7 extends the EV topology from 2WD to 4WD and performs preliminary exploration on the system optimization for 4WD configuration.

Chapter 8 summarizes the conclusions that can be drawn from previous studies and suggests several interesting topics for future work.

## 1.5. List of publications

Part of the work presented in this thesis is also reported in the publications listed below:

1. **M. Lu**, G. Domingues-Olavarria, F. J. Márquez-Fernández, P. Fyhr and M. Alaküla, "Electric Drivetrain Optimization for a Commercial Fleet with Different Degrees of Electrical Machine Commonality," *Energies* 2021, 14, 2989.
2. **M. Lu**, G. Domingues-Olavarria, F. J. Márquez-Fernández, H. Bydén and M. Alaküla, "Optimization of Induction Machine Design for Electric Vehicle Powertrain," 2023 IEEE International Electric Machines & Drives Conference (IEMDC), San Francisco, CA, USA, 2023, pp. 1-6, doi: 10.1109/IEMDC55163.2023.10238871.
3. **M. Lu**, G. Domingues-Olavarria, H. Bydén, M. Aleksandar and M. Alaküla, "Optimization of Powertrain Platform for Electric Passenger Vehicles," 2023 IEEE Transportation Electrification Conference & Expo (ITEC), Detroit, MI, USA, 2023, pp. 1-6, doi: 10.1109/ITEC55900.2023.10187120.
4. **M. Lu**, G. Domingues-Olavarria and M. Alaküla, "Comparison of PMSM versus PMa-SynRM and IM from an Optimized Electric Vehicle Powertrain Perspective," 2023 26th International Conference on Electrical Machines and Systems (ICEMS), Zhuhai, China, 2023, pp. 4075-4080, doi: 10.1109/ICEMS59686.2023.10344646.
5. **M. Lu**, G. Domingues-Olavarria, H. Bydén, and M. Alaküla, "Platform-based Powertrain Optimization for Electric Passenger Vehicles," *IEEE Transactions on Transportation Electrification*, submitted.
6. Domingues, G., Turesson, G., **Lu, M.** et al. Holistic Optimization of Electric Powertrains. *MTZ Worldwide*, 84, 16–25 (2023). <https://doi.org/10.1007/s38313-023-1532-6>
7. H. Bydén, G. Domingues-Olavarria, **M. Lu**, and M. Alaküla, "Impacts of using different semiconductor technologies on drivetrain optimisation" ESARS-ITEC 2024, submitted



# Chapter 2 Electrical Machine Design

The design of EMs for electric vehicles depends on specific requirements, including demands such as desired acceleration performance, top speed, gradeability, etc. PMSMs, which utilize rare earth magnets, are often preferred due to their high efficiency and power density [23]. This translates into lower energy consumption and extended driving ranges, coupled with the capability to provide high torque density, making them suitable for most passenger EV applications. However, the automotive industry faces challenges with PMSMs, primarily due to significant fluctuations in the cost of rare earth materials and concerns about supply chain stability [24].

Alternatively, IMs may offer a cost benefit over PMSMs as they do not require rare earth magnets and are not susceptible to demagnetization. However, the notable drawbacks of IMs include their relatively lower efficiency compared to PMSM and lower power factor, which requires a higher inverter current and typically pronounced drop in peak power as speed increases. This could increase overall energy consumption, potentially offsetting the benefits of initial cost savings.

In light of these considerations, the PMSynRM [25] has emerged as a promising alternative for various applications, including EVs. PMSynRMs utilize permanent magnets that require fewer or no rare earth materials in comparison to PMSMs. This attribute is advantageous in mitigating concerns related to the availability and environmental impact of rare earth materials, making PMSynRMs an increasingly viable option in the context of sustainable automotive development. However, PMSynRM's use of weaker magnets implies a lower torque and power density as well as a higher risk of permanent demagnetisation

In this thesis, three types of machines have been considered, due to their suitability for EV traction applications. Figure 2.1 shows examples of the geometry layouts for all three EM types.

The process of EM design is affected by many criteria and various considerations should be made. Achieving an optimal EM design for a given geometry is far from straightforward, as the ideal configuration is heavily dependent on the specific requirements of the application. For instance, an EM designed for a passenger EV, which typically operates at higher speeds,

would have different characteristics (size, geometrical proportions, amount of magnets if applicable, etc...) than an EM intended for a commercial truck used in city distribution.

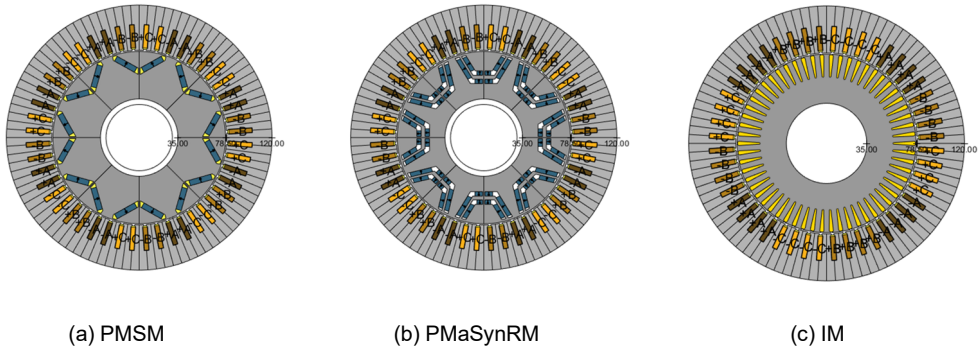


**Figure 2.1.** Electrical machine geometries for (a) PMSM, (b) PMaSynRM and (c) IM

The EM design is fundamentally an interdisciplinary endeavor, requiring a comprehensive assessment that incorporates aspects of electromagnetics, thermal performance, mechanical constraints, and cost considerations. A critical work of this process is the understanding of electromagnetic behavior. This includes the analysis of the magnetic field, stator windings, and materials to achieve desired performance characteristics such as torque, speed, losses, and efficiency.

In addition, the thermal management of EM is crucial to prevent overheating, thereby ensuring the EM's reliability. Thermal analysis in EM design enables designers to identify the machine's operational limitations and enhance its potential through effective heat management strategies.

Furthermore, the cost analysis for EM guides decision-making, ensures products' competitiveness in the market, and supports the overall goal of making EVs more accessible and affordable to consumers.

This chapter introduces the methods to address the questions and challenges in EM design. It lays the foundation for the subsequent powertrain optimization. Building upon this groundwork, a comparative analysis for the three types of machines from an optimized powertrain perspective will be thoroughly explored in Chapter 5.

## 2.1 EM Modelling Settings

### 2.1.1 Geometry Parametrization

The electromagnetic design of the EM takes advantage of a powertrain design and optimization tool developed at the department of Industrial Electrical Engineering and Automation (IEA) [26] and it is improved in this thesis with more EM topologies. The tool makes use of FEMM [27], which is an open source 2D finite element (FE) modelling software controlled with a script that is generated in MATLAB. The integration facilitates the execution of FE simulations directly from MATLAB. Essential model and simulation characteristics such as material properties, boundary conditions, meshing size and convergence criteria can be adjusted in the script. This leverages parametrized EM geometry to enable more nuanced and precise designs.

This section introduces four distinct rotor topologies spanning across three types of EMs. The first type, PMSM, is explored through two specific magnet arrangements for the rotor topologies: the single-V shape and double-V shape. These topologies are widely utilized in various EV applications due to their high efficiency performance and high power density.

The second machine type under consideration is the PMSynRM. Its rotor features a unique arrangement of multi-layered cavities with deeply embedded permanent magnets. This configuration is particularly noteworthy for its ability to enhance the reluctance torque while simultaneously reducing costs by employing non-rare-earth magnets.

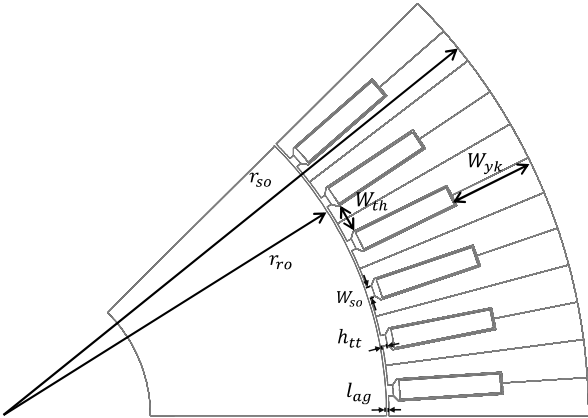
The third type is the IM, characterized by a squirrel cage rotor, showing high robustness and cost competitiveness. It is important to note that other EM topologies, such as the Switched Reluctance Machine (SRM) [28] and Electrically Excited Synchronous Machine (EESM) [29][30], can also be accommodated within this tool.

The parametrization of these different topologies is illustrated in Figure 2.2, which helps in understanding the structural differences among the topologies.

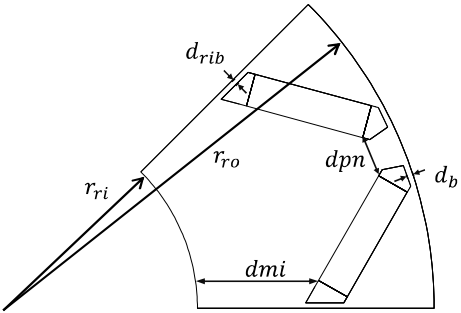
As it can be seen in Figure 2.2, to implement the FE model in FEMM automatically, the stator and rotor are fully parametrized. The slot configuration can be defined as parallel, accommodating hairpin winding, or the stator teeth can be set parallel to adapt traditional round wire winding. The slot size can be adjusted by varying the stator yoke width and the tooth width. For permanent magnet (PM) machines, the magnet size and placement are variable parameters. Additionally, the rib width is predetermined based on mechanical safety considerations.

As for IMs, the model allows for variation in the number of rotor bars and the total bar area, which are two crucial parameters in generating the IM database.

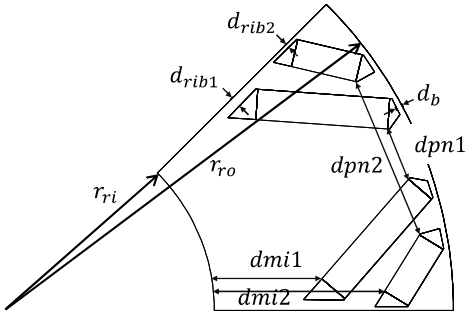
However, during the IM design process, a proper selection of stator slots and rotor bar number is always a challenge [31]. There are several empirical rules that should be followed when selecting the number of rotor bars to reduce torque ripple and avoid undesired operations [32], as expressed in (2.1)-(2.4).



(a) Stator geometry



(b) Single-V shape rotor geometry



(c) Double-V shape rotor geometry

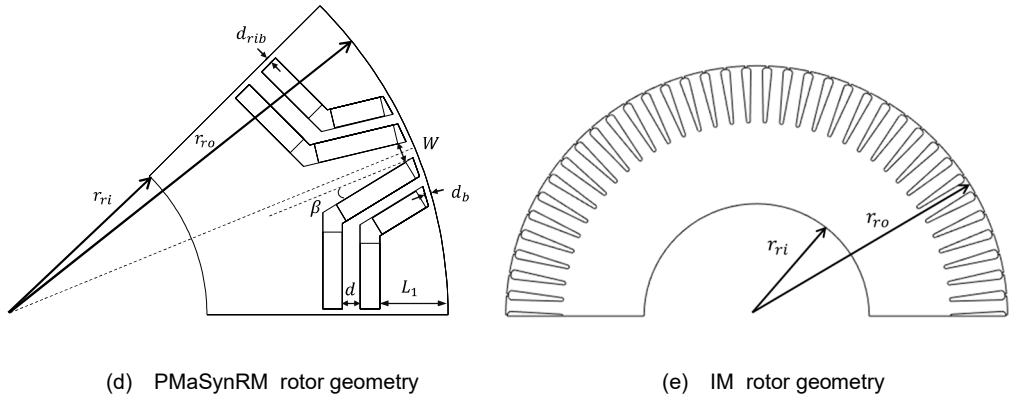


**Figure 2.2** Parametrization of different topologies for three types of EMs

$$N_{bar} \neq N_s \quad (2.1)$$

$$N_{bar} \neq 3nN_p \quad (2.2)$$

$$N_{bar} \neq 3nN_p \mp N_p \quad (2.3)$$

$$N_{bar} \neq N_s \mp N_p \quad (2.4)$$

where  $n$  is an integer,  $N_s$  is the number of stator slots,  $N_p$  is the number of poles and  $N_{bar}$  is the number of rotor bars. Furthermore, only even numbers of rotor bars are considered in order to avoid unbalanced magnetic pull between the stator and rotor [33].

The following table introduces the definitions of all parameters depicted in the figure.

**Tabel 2.1. Parameter definitions for all EMs**

Parameter		Definition
<b>Stator</b>	$r_{so}$	Stator outer radius
	$q$	Number of slots per pole per phase
	$W_{yk}$	Width of the stator yoke
	$W_{th}$	Width of the narrowest stator tooth
	$K_{iron}$	Factor to adjust $W_{yk}$ and $W_{th}$
	$W_{so}$	Width of slot opening
	$h_{tt}$	Height of tooth tip
<b>Interface</b>	$l_{ag}$	Air gap length



<b>Rotor</b>	$r_{ro}$	Rotor outer radius
	$r_{ri}$	Rotor inner radius
	$N_p$	Number of poles
	$d_{pn}$	Distance between magnet edges of the neighbour pole magnets
	$d_{mi}$	Distance between magnet edge and rotor inner radius
	$h_{pm}$	Height of the magnets
	$n_{hl}$	Number of magnet layers
	$\beta$	Magnet placement angle
	$L_1$	Relative magnets position
	$N_{bar}$	Number of rotor bars
	$A_{bar}$	Ratio between the total area of rotor bars and the rotor area

The maximum mechanical speed of the EMs plays a crucial role in evaluating their performance. It is determined by various factors, including EM geometry and layout of the rotor, and yield strength of the material (electrical steel). The rotor should withstand the centrifugal forces that arise at high speeds.

In this thesis, an analytical way to estimate the maximum mechanical stress for EMs [34] is presented in (2.5), where  $\omega_{max\_ms}$  is the maximum mechanical speed determined by mechanical stress,  $\sigma_{yield}$  is the yield strength of the laminations,  $d_{rib}$  is the width of the iron ribs,  $h_m$  is the machine active length,  $m_{act}$  is the total mass of the magnets and the rotor between the magnets and the airgap, and  $r_{act}$  is the distance to the center of gravity of  $m_{act}$ , all expressed for one pole of the machine.

$$\omega_{max\_ms} = \sqrt{\frac{\sigma_{yield} \cdot d_{rib} \cdot h_m}{m_{act} \cdot r_{act}}} \quad (2.5)$$

Besides the constraints by mechanical stress limitation, there are two extra constraints introduced when estimating the speed, as shown in (2.6) and (2.7).

$$\omega_{max\_ps} = 60v_{ps}/2\pi r_{ro} \quad (2.6)$$

$$\omega_{max\_fs} = 60f/p \quad (2.7)$$

Where  $\omega_{max\_ps}$  is the maximum speed determined by the predefined maximum peripheral speed of rotor ( $v_{ps}$  is set to 120 m/s).  $\omega_{max\_fs}$  is the maximum speed determined by the predefined maximum electrical frequency ( $f$ ).  $p$  is the number of pole pairs.

The maximum mechanical speed is then determined by selecting the lowest maximum speed, as expressed in (2.8).

$$\omega_{max} = \min [\omega_{max\_ms}, \omega_{max\_ps}, \omega_{max\_fs}] \quad (2.8)$$

### 2.1.2 Winding design

The requirement for maximizing the EMs' power and torque density has led to a revolution in winding technology [35]-[40]. A critical aspect of this evolution is to increase the slot filling factor by replacing the traditional round-wound wires with rectangular conductors, usually implemented as hairpins.

Hairpin winding is a configuration used in the stator of EMs, particularly in high-performance EMs. The name of this winding configuration derives from its resemblance to U-shaped loops or hairpins. It is designed to improve the efficiency and power density of the electrical machine by reducing losses and improving the filling factor.

In contrast to traditional stator windings, where the coils are created using continuous wire leading to longer end-turns and increased resistance, hairpin windings utilize many shorter conductors, typically rectangular or square in shape, connected (welded) side by side. This design significantly reduces the gaps between conductors compared to traditional round-wire windings, resulting in a higher slot filling factor and lower thermal resistance. Additionally, the shorter end turns of hairpin windings contribute to a reduction in the direct current (DC) resistance of the winding. However, it is important to note that the skin and proximity effect [40]-[43] at high speeds introduces a higher frequency dependent loss, which will be discussed later.

The lower thermal resistance of hairpin windings facilitates more efficient cooling within the stator. This allows heat generated by the winding to be more effectively dissipated, thereby enhancing the thermal performance of the EM. As a result, hairpin windings enable the EM to sustain higher current load without overheating. This capability translates into either a higher power output for a given machine size or the possibility of designing a more compact EM that can deliver the intended power compared to EM with traditional windings.

Figure 2.3 shows a rectangular slot for hairpin windings with 8 conductors/layers.

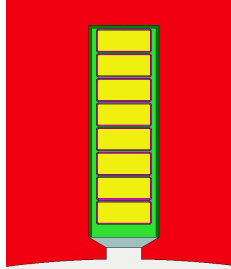


**Figure 2.3** Hairpin winding with 8 layers

When generating the EM model, the winding design is not determined. Simulating the same EM with different winding layouts (different number of layers) will increase the simulation time dramatically. In this study, the hairpin winding is modeled as one single conductor, as shown in Figure 2.2 (a). To explore more design possibilities, such as 4, 6 and 8-layer hairpin winding, a feasibility check for hairpin winding designs is implemented for future winding exploration and the losses are evaluated for each feasible case.

For the EMs generated with FEMM, the default number of turns per phase can be determined using the expression (2.9).

$$N_t = pqN_c/N_{pp} \quad (2.9)$$

Where  $N_t$  represents the number of turns,  $p$  denotes the number of pole pairs,  $q$  is the number of slots per pole per phase,  $N_c$  indicates the number of conductors per slot (with a default value of 1) and  $N_{pp}$  is the number of parallel path (also with a default value of 1).

Although hairpin windings exhibit advantages in certain aspects, they have limited flexibility in terms of feasible winding configurations. Consequently, it becomes imperative to implement extra design guidelines. These guidelines verify the practicability of arranging the conductors within the stator slots based on specific slot/pole combinations and determine the number of viable parallel paths [39][45].

As the hairpin windings are formed with lap-winding topology, the number of conductors in the slot should be even (There are ways of having an uneven number of conductors, but this adds manufacturing complexity and increases the number of unique conductors needed).

The series connection ( $N_{pp} = 1$ ) is always feasible since all the phases have the same impedance. However, when multiple parallel paths are required, it is crucial to ensure that each parallel path exhibits the same impedance to avoid current unbalance and additional

copper losses. To achieve this, the hairpin winding should be transposed, meaning each winding path needs to be located in every layer of the slot. This is because the impedance of the conductors in each layer is also different [35][39]. In order to ensure this, the following rules need to be followed:

**Rule 1:** the conductors that belong to the same parallel path have to cover all the layers of the slot (ensure the same inductance for each parallel path).

When the number of slots per pole per phase,  $q$ , is higher than 1, the electro-motive force (EMF) induced in the conductors of the adjacent slots is different.

Then the second rule is introduced as:

**Rule 2:** The conductors that belong to the same parallel path should be distributed in all slots per pole of that phase (ensure the same back EMF for each parallel path).

The design rules can be converted to the analytical expressions as below:

$$\frac{\text{number of conductors per parallel path}}{\text{number of layers}} = \frac{2pq \frac{N_c}{N_{pp}}}{N_c} = \frac{2pq}{N_{pp}} = \text{integer} \quad (2.10)$$

$$\frac{\text{number of conductors per parallel path}}{\text{number of slots per pole per phase}} = \frac{2pq \frac{N_c}{N_{pp}}}{q} = \frac{2pN_c}{N_{pp}} = \text{integer} \quad (2.11)$$

An example of feasible number of turns for 3 different number of layers is shown in Figure 2.3 (b). It is worth noticing that in both the automotive industry [44] and academic research [45], significant efforts are underway to model and analyze the 10-layer hairpin windings. Table 2.3 presents a detailed illustration of feasible number of turns with specific pole/slot combination.

**Tabel 2.3. Feasible number of turns**

$p = 3, q = 2$				
$N_{pp} \backslash N_c$	1	2	3	6
4	24	12	8	4
6	36	18	12	6
8	48	24	16	8

## 2.2 Modelling of PMSM and PMaSynRM

### 2.2.1. FE simulation initialization

The EM performance evaluations are initiated with the FE models generated based on the predefined parametrized EM geometry. A set of magnetostatic FE simulations for PM machines are implemented with different current combinations and rotor positions, as can be seen in Figure 2.4. Although the characteristics of PMSM and PMaSynRM differ significantly, these two machine types can be described with the same equations.

For PM machines,  $i_d$  and  $i_q$ , which represent the direct and quadrature axis currents respectively, are introduced to decouple the applied stator current from the rotor position. This simplifies the control and performance mapping on the machine [46]. enabling the EM to operate more efficiently under various load conditions.

With this in mind, the normalized  $i_d$  and  $i_q$ , which will be explained in the following section, are taken as the FE simulation inputs for further EM efficiency optimization.

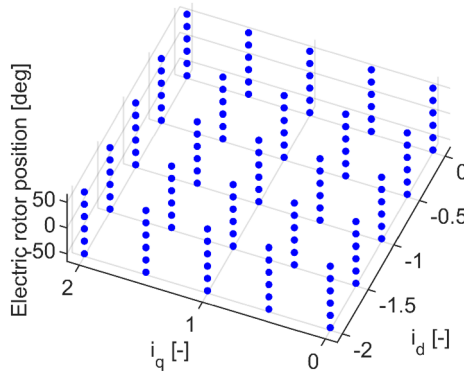


**Figure 2.4** FE simulation inputs for PM machines

In the FE model, peak phase current values need to be assigned to each of the phases. These values can be calculated as:

$$\begin{bmatrix} \widehat{I}_a \\ \widehat{I}_b \\ \widehat{I}_c \end{bmatrix} = \sqrt{\frac{2}{3}} k_f A_s \begin{bmatrix} \sin(\theta) & \cos(\theta) & 1 \\ \sin(\theta - \frac{2\pi}{3}) & \cos(\theta - \frac{2\pi}{3}) & 1 \\ \sin(\theta + \frac{2\pi}{3}) & \cos(\theta + \frac{2\pi}{3}) & 1 \end{bmatrix} \begin{bmatrix} i_d \\ i_q \\ 0 \end{bmatrix} J_{ini} \quad (2.12)$$

Where  $i_d$  and  $i_q$  are normalized values from the current vectors,  $\theta$  is the electrical rotor position. The whole operation plane illustrated in Figure 2.4 should be scanned during the FE simulation.  $k_f$  is the winding filling factor,  $A_s$  is the slot area and  $J_{ini}$  is the initial current density, which will be re-evaluated with the thermal model.  $\sqrt{\frac{2}{3}}$  is the power invariant factor to keep the power identical during the Park and Clarke transformation.

## 2.2.2. Loss estimation

### DC copper losses

The stator DC copper losses are determined by the DC resistance of the winding. The DC resistance is determined by (2.13).  $\rho_{Cu}$  is the resistivity of copper,  $l_{act}$  is the active length of the winding and  $l_{end}$  is the length of the end turns.

$$R_{s\_DC} = \rho_{Cu} \frac{l_{act} + l_{end}}{A_s k_f} \quad (2.13)$$

The copper resistivity is temperature dependent and determined by (2.14).

$$\rho_{Cu} = \rho_0 (1 + \alpha(T_{ref} - T_0)) \quad (2.14)$$

where  $\alpha$  is the temperature coefficient of resistivity,  $T_{ref}$  is the reference temperature of the winding to estimate the losses,  $T_0$  is a fixed reference temperature (usually room temperature), and  $\rho_0$  is the resistivity at temperature  $T_0$ .

The length of the end turns for hairpin winding is estimated by (2.15)

$$l_{end} = \frac{\pi(r_{so} + r_{ro})}{p} + 4q w_s c_{ew} \quad (2.15)$$

Where  $w_s$  is the width of the conductor in the slot,  $c_{ew}$  is a coefficient ( $c_{ew} = 1.2$ ) to compensate not considering the end winding extension and the distance between each conductor.

Then the stator DC losses are estimated by (2.16)

$$P_{cu\_DC} = R_{s\_DC} (i_d^2 + i_q^2) \quad (2.16)$$

## AC copper losses

For an EM with hairpin windings, the AC copper losses in the winding cannot be neglected as they can be significantly increased due to skin and proximity effects [47][48]. A major part of these AC losses is primarily caused by the current induced by time-varying leakage flux in the slots.

A homogenized approach based on [34][49] is utilized with the assumption that the leakage flux acting on the conductors in the slot flows in tangential direction, and 19 points are selected to extract the data of flux density along the slot, which is shown in Figure 2.5.

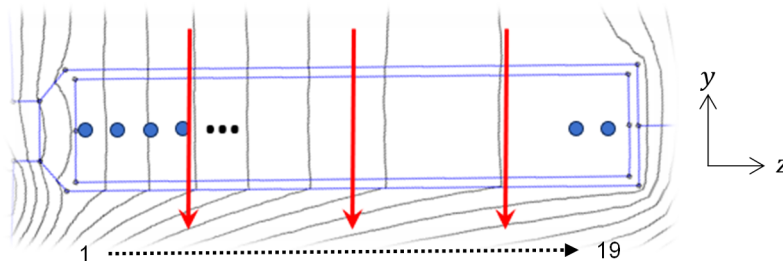


**Figure 2.5** Leakage flux distribution in the slot

The magnetic field varies at different positions along the slot, and the leakage flux close to the air gap is more significant compared with that at other positions, which can be seen in Figure. 2.6.

The leakage flux can be expressed as a sinusoidal waveform along the  $y$  axis, expressed as in (2.17).

$$\mathbf{B} = \hat{B} \cdot \sin(\omega_e t) \quad (2.17)$$

Where  $\hat{B}$  is the peak flux density and  $\omega_e$  is the electrical angular speed.

A more accurate way to define the leakage flux is to include the harmonics of the leakage flux. In that case, the flux density can be expressed as in (2.18).

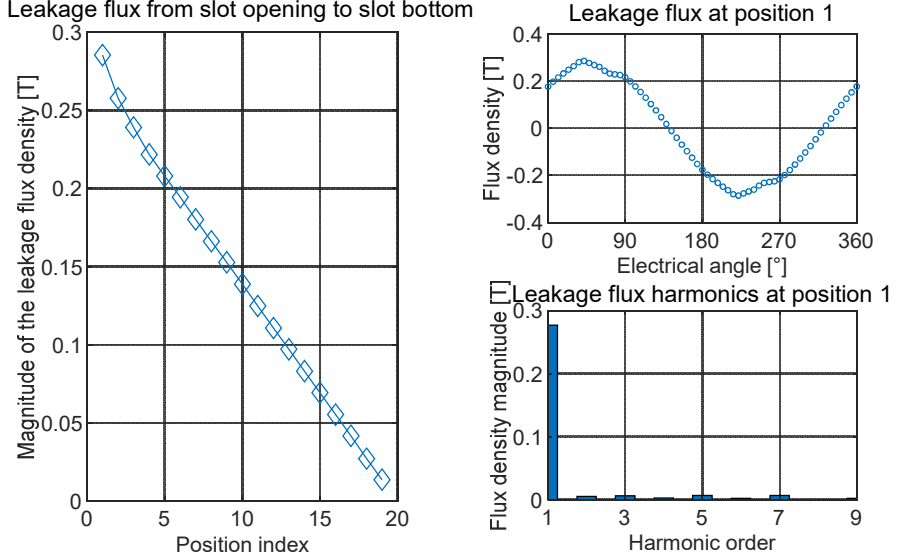


**Figure 2.6** Leakage flux in the slot under certain operating condition

$$\mathbf{B} = \sum_{m=1,3,5,\dots}^{\infty} B_m \cdot \sin(m\omega_e t) \quad (2.18)$$

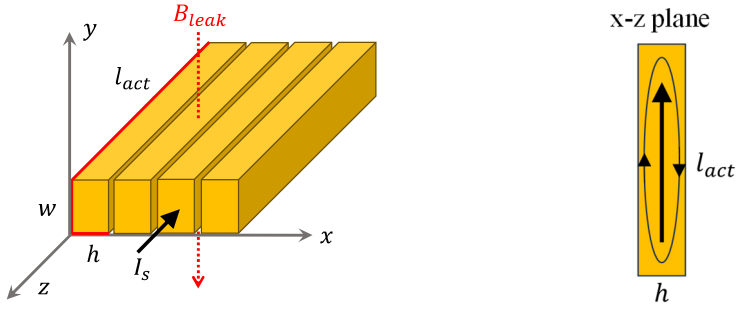
Where  $B_m$  and  $\omega_e$  are the amplitude of the  $m$ -order harmonics for the leakage flux and electrical angular speed of the first order harmonics of the leakage flux for this conductor, respectively.

To illustrate how the AC losses are generated and estimated, a four-layer hairpin winding is assumed, as shown in Figure 2.7 (a).  $w$  is the width of each conductor,  $h$  denotes the height of each conductor and  $l_{act}$  is the conductor length in the slot. The leakage flux,  $B_{leak}$ , travels through the slot along the  $y$  axis. Based on the Maxwell-Faraday equation, expressed as (2.19).

$$\nabla \times \mathbf{E} = -\frac{\partial \mathbf{B}}{\partial t} \quad (2.19)$$

There will be eddy currents (electric field) generated in the conductor, causing current unbalance along the  $x$  axis, which can be seen in Figure 2.7 (b).





(a) Leakage flux in the stator slot

(b) Circulating current in one conductor

**Figure 2.7** AC losses due to the external magnetic field

When equation (2.19) is solved, it yields:

$$\mathbf{E} = B \cdot \omega_e \cdot x \cdot \cos(\omega_e t) \hat{z} \quad (2.20)$$

The AC losses in the conductor can be developed to a function of conductivity and electric field according to (2.21)

$$P_{cu\_AC} = R_{AC} \cdot i_{eddy}^2 = \rho \cdot J^2 = \frac{1}{\sigma} \cdot (\sigma \cdot E)^2 = \sigma \cdot E^2 \quad (2.21)$$

Then the average power loss can be determined with (2.22) where the average loss density is integrated over a quarter of the conductor and multiplied by four.

$$P_{cu\_AC} = 4 \int_{z=0}^{l_{act}} \int_{y=0}^{w/2} \int_{x=0}^{h/2} \sigma E^2 dx dy dz \quad (2.22)$$

When solving the integration in (2.21), the average power loss in one conductor becomes (2.23).

$$P_{cu\_AC} = \frac{1}{24} \cdot \sigma \cdot B^2 \cdot \omega_e^2 \cdot h^3 \cdot w \cdot l_{act} \quad (2.23)$$

It can be concluded that the AC losses depend on a square relation to the electrical angular frequency and leakage flux in the slot. As the EM speed increases, the corresponding stator electrical frequency also increases, leading to higher AC losses. The hairpin winding layout also plays an important role in decreasing the AC losses. With more layers in the slot, the

height for each conductor is decreased, which can dramatically reduce the AC losses. However, with increasing the number of winding layers, considering the total insulation for all conductors, the filling factor will decrease, which in turn affects the total copper losses.

The insulation prevents electrical short circuits between adjacent windings or between the windings and the stator cores [50]. The insulation thickness can be set as in (2.24) and the liner thickness is set to 0.25mm.

$$ins = \begin{cases} 0.085\text{mm}, U_{dc} = 400\text{V} \\ 0.17\text{mm}, U_{dc} = 800\text{V} \end{cases} \quad (2.24)$$

The DC and AC copper losses are assessed for different number of layers in the slot under two rotational speeds, as shown in Figure 2.8. This comparison demonstrates how the configuration of the hairpin winding and the EM speed influence the copper losses. It can be seen that with more layers in the slot, the total insulation takes more space compared to that with fewer layers, leading to a lower filling factor and thus higher DC copper losses. The total copper losses at low speed may be higher with more layers. Taking the winding complexity and cost into account, the selection of the number of layers for hairpin windings should be considered from a system perspective.

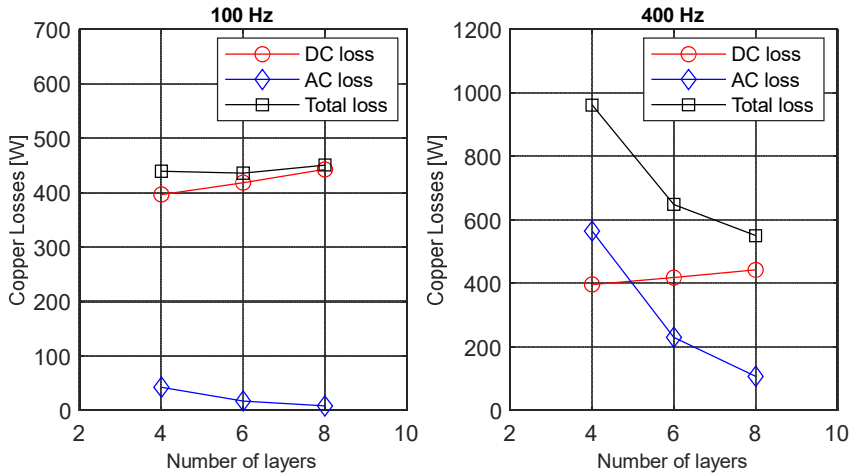


**Figure 2.8** AC and DC losses with various settings

## Iron losses

Iron losses mainly occur within the magnetic cores due to the variation of magnetic flux [51]. The losses found in the iron core are related to magnetic flux density  $B$  and magnetizing frequency  $f$  as well as material parameters. The flux density data is collected from the middle point of the stator tooth and yoke, which is displayed in Figure 2.9.

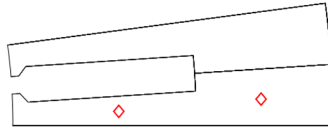


**Figure 2.9** The positions where the flux density for tooth and yoke are collected

The flux waveforms for stator tooth and yoke are shown in Figure 2.10. As the flux waveform is not sinusoidal, the harmonics of each waveform are derived.

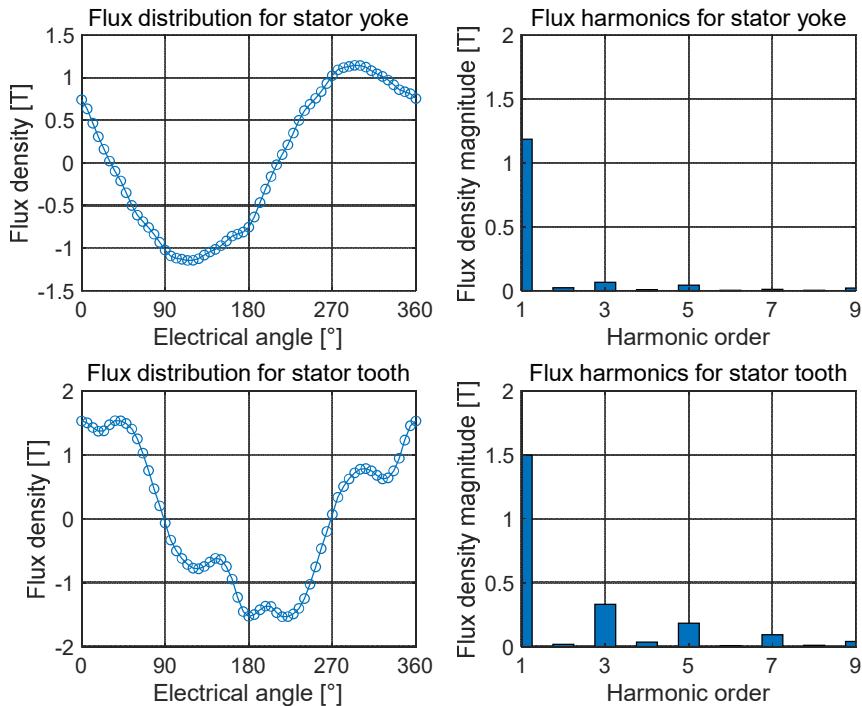


**Figure 2.10** Flux distribution and harmonics for stator tooth and yoke under certain condition

The estimation of iron losses is always challenging and can be influenced by various factors, including the degradation of the magnetic properties, the harmonics of the magnetic field, etc. In this thesis, the iron losses are estimated with the method proposed by Steinmetz and Bertotti [51][52][53].

$$P_{Fe} = \left( c_{hyst} \cdot \sum_{m=1,3,5,\dots}^{\infty} B_m^2 f_m + c_{eddy} \cdot \sum_{m=1,3,5,\dots}^{\infty} B_m^2 f_m^2 \right. \\ \left. + c_{ex} \cdot \sum_{m=1,3,5,\dots}^{\infty} B_m^{1.5} f_m^{1.5} \right) m_{Fe} k_{cf} \\ f_m = mf \quad (2.25)$$

Where  $B_m$  is the amplitude of the  $m$ -order harmonics for stator and yoke,  $f$  is the frequency of the fundamental harmonic of the magnetic field,  $f_m$  is the frequency of the  $m$ -order harmonic of the magnetic field,  $m$  is the index for the harmonics order, and  $m_{Fe}$  is the mass of the core. The coefficients for the hysteresis ( $c_{hyst}$ ), eddy current ( $c_{eddy}$ ) and excess losses ( $c_{ex}$ ) can be derived from the datasheet of the core material.

As the laminations are being processed throughout manufacturing, the loss characteristics are affected. This includes the material structure close to the edges after cutting or punching, as well as creating unwanted axially directed conducting paths when stacking the iron core [34][54]. A correction factor  $k_{cf}$  is introduced ( $k_{cf} = 1.8$  in this thesis) to account for the manufacturing effects on iron losses estimation.

### Magnet losses

In permanent magnets, the losses are mainly caused by the eddy currents induced in the magnets. A magnet can be seen as a conducting cuboid in the rotor. The magnetic field is in the  $z$  direction, as shown in Figure 2.11. The eddy currents induced in the magnet are illustrated as the circulating electric field in the  $xy$ -plane.

The magnetic field in the  $z$  direction under various operating conditions is shown in Figure 2.12. The static magnetic field doesn't contribute to the losses in the magnet. The alternating magnetic field can be seen as the sum of its harmonics.

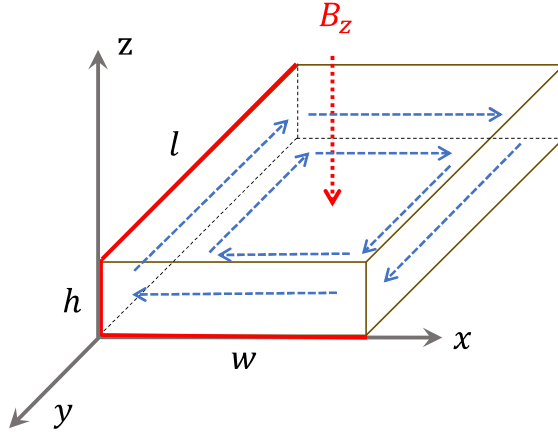


**Figure 2.11** Induced electric field by external magnetic

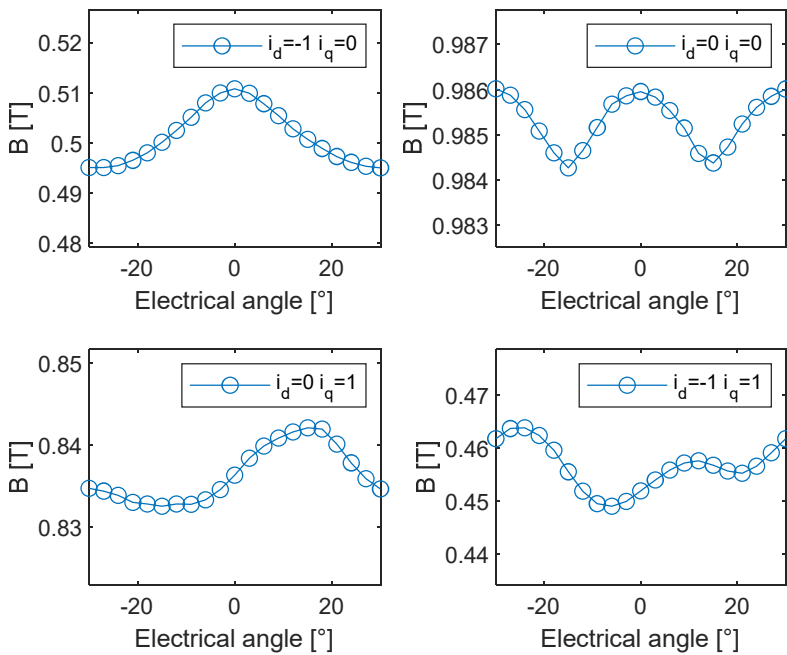


**Figure 2.12** Magnetic field in magnets under various operating conditions

The induced electrical field in the magnet in the  $xy$ -plane can be derived from Faraday's law.

$$-\frac{\partial \mathbf{B}_z}{\partial t} = \begin{vmatrix} \hat{x} & \hat{y} & \hat{z} \\ \frac{\partial}{\partial x} & \frac{\partial}{\partial y} & \frac{\partial}{\partial z} \\ E_x & E_y & E_z \end{vmatrix} \quad (2.26)$$

The magnet losses can be estimated for one frequency component with (2.27) and finally determined as in (2.28).

$$P_{mag} = \int_{z=0}^h \int_{y=0}^l \int_{x=0}^w \sigma (E_x^2 + E_y^2) dx dy dz \quad (2.27)$$

$$P_{mag} = lhw \sum_{m=1,3,5\dots}^{\infty} \sum_{n=1,3,5\dots}^{\infty} \frac{\sigma \omega^2 B_{mn}^2}{8(\bar{m}^2 + \bar{n}^2)} \quad (2.28)$$

Where  $\sigma$  is the electrical conductivity of magnets,  $l$  is the length of the magnet,  $h$  is the thickness/height of the magnet,  $w$  is the width of the magnet,  $\omega$  is the electrical angular speed of the external magnetic field.  $B_{mn}$ ,  $\bar{m}$  and  $\bar{n}$  are values related with magnitude of magnetic field and the order of harmonics.

A detailed derivation of (2.28) is given in Appendix A.

### Mechanical losses

The mechanical losses of EMs are primarily due to bearing friction and windage. Bearing friction losses originate from the friction between the balls and inner and outer rings. They cannot be eliminated entirely even if lubrication is used to minimize these losses. Windage losses are related to the friction between moving (rotating) parts and the surrounding air.

The estimation of the mechanical losses is also challenging. There are analytical ways using fluid properties [34][55] to estimate the windage losses. Experiments using a non-magnetized dummy rotor [56] to predict the mechanical losses are the most reliable. However, it is not feasible in this study since a very high number of EMs are evaluated. In this thesis, an approach based on analytical and empirical methods is proposed to estimate the losses, which can be expressed in (2.29) and (2.30).

$$P_{fric} = P_{fric0} \left( \frac{n}{n_0} \right)^{k_{fric}} \quad (2.29)$$

$$P_{wind} = P_{wind0} \left( \frac{n}{n_0} \right)^{k_{wind}} \quad (2.30)$$

Where  $P_{fric}$  is the friction losses,  $P_{fric0}$  is the friction losses at reference speed ( $n_0$ ),  $P_{wind}$  is the windage losses,  $P_{wind0}$  is the windage losses at reference speed ( $n_0$ ),  $n$  is the mechanical speed,  $k_{fric}$  and  $k_{wind}$  are the coefficients to estimate each loss ( $k_{fric} = 1$  and  $k_{wind} = 2.6$  in this thesis).

### 2.2.3. Performance evaluation

Once the FE simulations are completed, the data for electromagnetic torque, flux linkage, flux density under different current combinations and rotor positions are collected for the loss estimation. In this work, the maximum torque per ampere (MTPA) strategy, which can ensure maximum torque generation and minimum copper loss (current) in the stator winding, is selected to derive the optimal current combination for each operation point, considering voltage and current limitations.

For PMaSynRM the same d-q reference frame system as for PMSM is used. Fig 2.13 (a) and (c) show the phasor diagrams obtained for PMSM and PMaSynRM in steady state condition, while Fig 2.13 (b) and (d) depict the iso-torque and iso-flux linkage contour lines together with the loci of the MTPA and the maximum stator current lines.

The total torque of the PMSM and PMaSynRM is expressed by (2.31).

$$T_{PM} = \frac{3}{2} p ((L_d - L_q) I_d I_q + \varphi_m I_q) \quad (2.31)$$

Where  $L_d$  and  $L_q$  are the  $d$  and  $q$  components of the inductances,  $\varphi_m$  is the flux linkage from the magnets. This equation shows the reluctance and magnet torque, which is given by (2.32-2.33).

$$T_{rel} = \frac{3}{2} p (L_d - L_q) I_d I_q \quad (2.32)$$

$$T_{mag} = \frac{3}{2} p \varphi_m I_q \quad (2.33)$$

It is clear that due to weaker magnets used in the PMA<sub>Syn</sub>RM, the magnet torque is lower than that of PMSM for the same current rating. As the unique rotor structure of the PMA<sub>Syn</sub>RM (lower  $L_d$  than PMSM), the reluctance torque takes more proportion of the total electromagnetic torque.

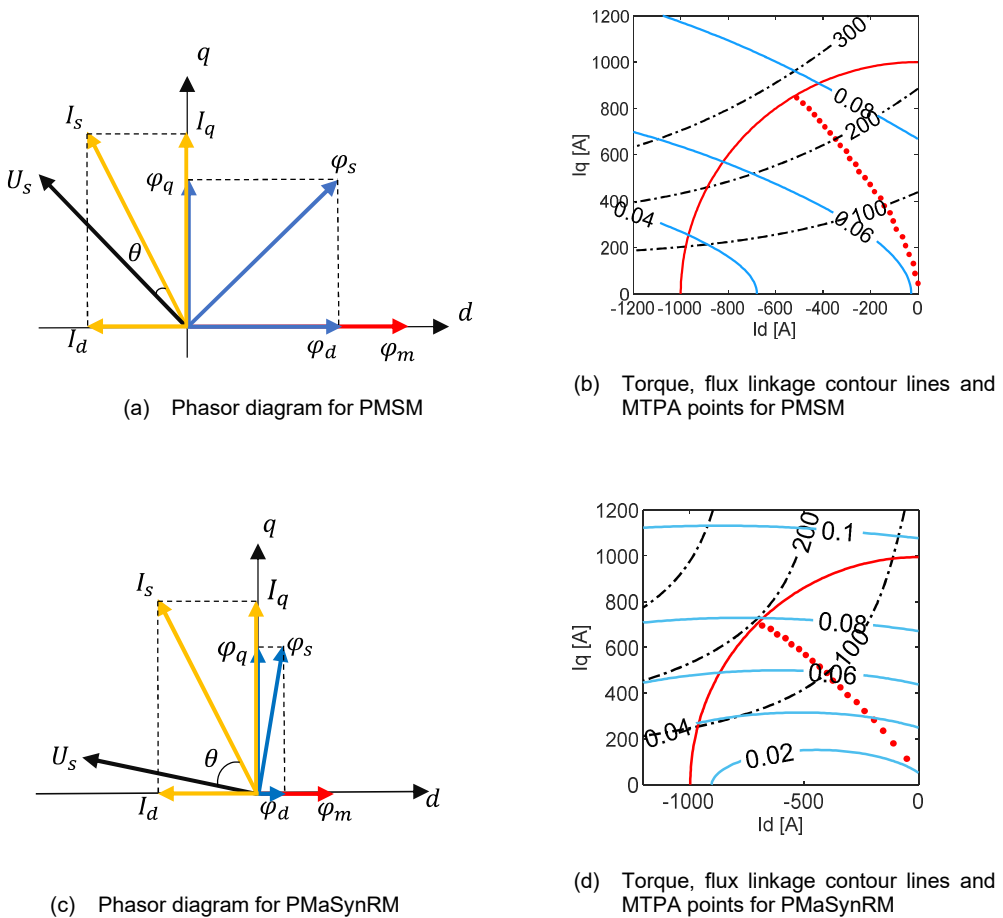


**Figure 2.13** Phasor diagram and MTPA points for PMSM and PMA<sub>Syn</sub>RM



## 2.3 Modelling of IM

### 2.3.1. FE simulation initialization

For induction machines, the relationship between synchronous speed ( $\omega$ ), rotor mechanical speed ( $\omega_r$ ), slip frequency ( $\omega_s$ ), slip ( $s$ ) and the number of pole pairs ( $p$ ) can be expressed as follows:

$$\omega_s = \omega - p\omega_r \quad (2.34)$$

$$\omega_s = s\omega \quad (2.35)$$

When performing the FE simulations, the rotor is kept fixed, meaning  $\omega_r = 0$ , hence the slip frequency  $\omega_s$  is identical to the synchronous speed ( $\omega_s = \omega$ ). FE simulations for IMs are conducted with different current and slip frequency combinations, as can be seen in Figure 2.14.

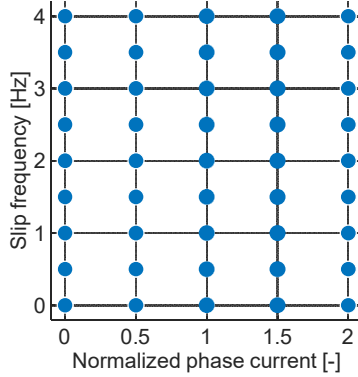


**Figure 2.14** FE simulation input for IM

As for IM, the peak phase current can be calculated as below.

$$I_{phase\_pk} = k_f A_s J_{ini} \quad (2.36)$$

The active length of all simulated EMs is set to a fixed value. Due to symmetry considerations, only  $1/N_p$  of the EM needs to be modelled.

### 2.3.2. Loss estimation

For the IM, as the current induced in the rotor bars is calculated in the FE simulations, the copper losses for the rotor bars ( $P_{cu\_bar}$ ) can be derived from the FE simulation directly. And the losses for the rotor end ring can be estimated with the assumption that the current density in rotor bars and end ring are kept the same [50][59]. Then the end ring losses are expressed by (2.37).

$$P_{cu\_er} = \frac{4I_r^2 \rho_{cu} r_{ro} N_{bar}}{N_p A_{bar}} \quad (2.37)$$

Where  $I_r$  is the induced current in the rotor bars,  $\rho_{cu}$  is the resistivity of copper,  $r_{ro}$  is the outer radius of the rotor,  $N_{bar}$  is the number of rotor bars,  $N_p$  is the number of poles,  $A_{bar}$  is the cross-sectional area of a single rotor bar and  $P_{cu\_er}$  represents the copper losses of the end ring.

### 2.3.3. Performance evaluation

For IM, the stator phase current and slip frequency are used as inputs of the FE simulations. The FE model is designed to perform a comprehensive parameter scan encompassing all predefined input combinations. The FE model then outputs several key variables, including torque, flux linkage, and flux density, among others. These outputs provide a quantitative measure of the IM's performance under varying conditions. The torque and flux linkage contour map are then generated as a function of the stator phase current and slip frequency, as illustrated in Figure 2.15.

It can be seen that the points conforming the MTPA correspond to the minimum stator phase current for each torque level (i.e. the lowest point in each iso-torque line). Each of these optimal operating points is characterized by unique stator phase current and slip frequency values. The research objective of this thesis is to optimize the powertrain based on the different EMs. Therefore, the estimation of IM parameters and current decoupling are beyond the scope of this research. With this method, it is possible to directly extract the electromagnetic data from FE simulations and perform the loss estimation.

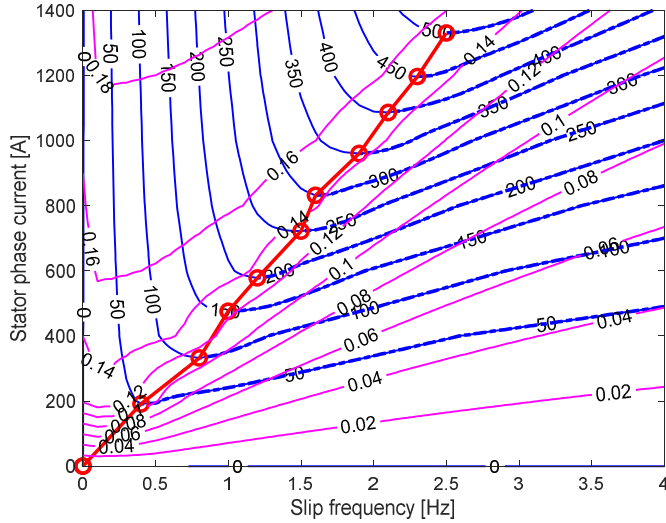


**Figure. 2.15** Torque (blue) and flux linkage (pink) maps, MTPA points (red circle)

## 2.4 EM Scaling

When performing the powertrain optimization, one of the main objectives is to find the most appropriate EM solution with multiple constraints and targets. This requires a large search-space of EMs for the optimizer to explore. During the optimization, a huge number of EM evaluations are made, leading to a high requirement on the computational efficiency to perform the full optimization within a reasonable time. Meanwhile, the EM models in the search-space should be accurate enough. In this work, one or more databases containing thousands of EMs with different 2D geometries are generated as one of the inputs of the powertrain optimization process. Each of these EM models is formulated using finite element method, which ensures the model accuracy.

Within the pre-defined database, certain EM models, termed as "base machine", act as machine primitives or starting points. These base machines come with specific parameters. One key feature of these base EMs is the active length, which is set as 200 *mm* in this thesis. Additionally, they have a consistent number of turns, symbolized as  $N_t^*$  ( $N_t^* = pq$ ), and they operate with a pre-specified current density.

However, challenges arise when dealing with the complex and diverse requirements of real-world applications. For instance, a specific application may require an EM solution with different physical dimensions or winding layout, depending on the vehicle requirements: a high acceleration requirement will translate into a high torque requirement, leading to

potentially larger machines and higher currents. A high speed requirement will affect the winding layout for a given traction battery voltage.

Considering the wide range of requirements, creating EM models with finite element method to explore the optimal design is not only resource-intensive but also impractical. Therefore, the scaling method [62][63] is introduced. Instead of building new EM models with different variations with distinct dimensions and winding layouts, a scaling method enables to adjust the existing base EMs to expand the design space and finally derive the optimal design with the specific application requirements. By adopting such an approach, the optimization process becomes significantly more efficient.

The base motor in the database can be scaled with three factors:  $k_a$ , the ratio between axial length of the scaled machine and the base machine,  $N_t$ , the desired number of turns, and  $k_{ov}$ , the ratio between peak and nominal current.

The first scaling factor is used to proportionally scale the axial active length of the base EM. When changing the EM active length, the flux density remains consistent, and the torque has a proportional relation with the relative scaling factor  $k_a$ . This linear proportional relationship also applies to flux linkage, active copper losses and core losses. However, the losses from the end windings will not be affected as the length of the end winding is not affected.

As the flux linkage has a proportional relation to  $N_t$ , scaling the number of turns can change the back EMF for a given DC-link voltage to adjust the EM base speed. As the total current in one slot is kept the same, the phase current of the EM and the PEC rating is affected when the number of turns is changed.

The influences of scaling factors on the machine behaviors are shown in Table 2.4.

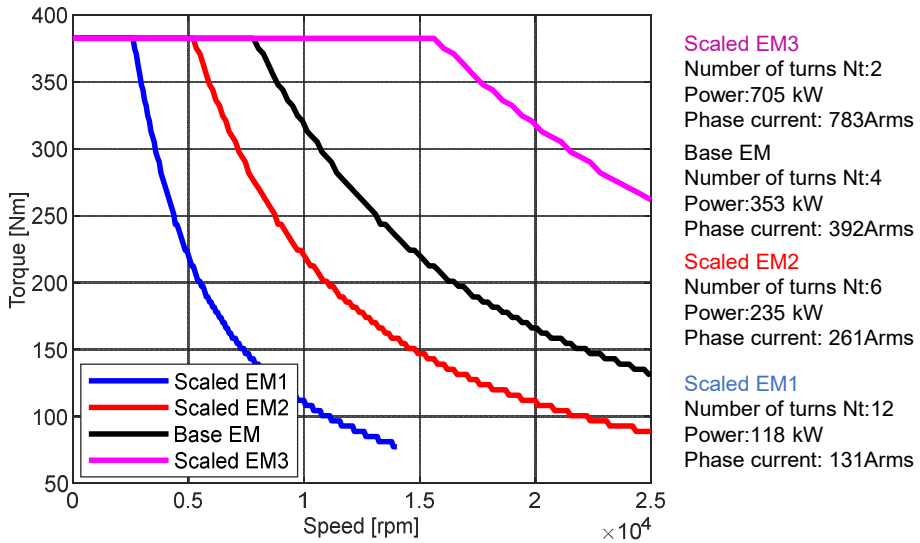
**Table 2.4. Parameters of EM in the database**

Variable	Definition	Scaling rules
$T_{vec}^*$	Torque vector	$T_{vec} = T_{vec}^* \cdot k_a$
$\psi_{dq}^*$	Flux linkage	$\psi_{dq} = \psi_{dq}^* \cdot k_a \cdot (N_t/N_t^*)$
$R_{s,act}^*$	Resistance inside the slot	$R_{s,act} = R_{s,act}^* \cdot k_a$
$R_{s,end}^*$	Resistance in the end windings	$R_{s,end} = R_{s,end}^*$
$I_{dq}^*$	Stator current	$I_{dq} = I_{dq}^*/(N_t/N_t^*)$
$U_d^*$	Induced voltage in d axis	$U_d^* = R_s^* I_d^* - \omega_e^* \psi_q^*$
$U_q^*$	Induced voltage in q axis	$U_q^* = R_s^* I_q^* - \omega_e^* \psi_d^*$

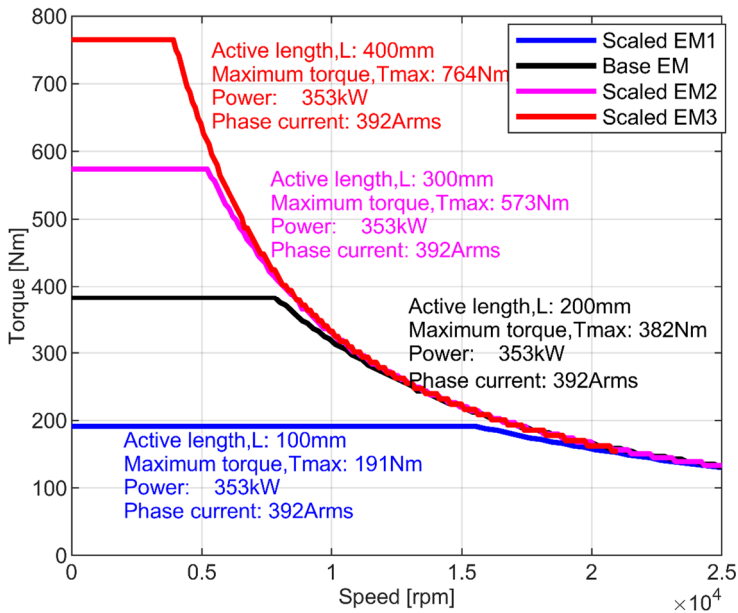
$U_{smax}^*$	Maximum induced voltage of base EM	$U_{smax}^* = \max(\sqrt{U_d^{*2} + U_q^{*2}})$
$N_{t,ideal}$	Ideal number of turns with given DC-link voltage	$\frac{m_a U_{dc}}{\sqrt{2} U_{smax}^*} N_t^*$
$k_{nt}$	Change in number of turns	$k_{nt} = \frac{N_{t,ideal}}{N_t}$
$\omega_{vec}^*$	Speed vector	$\omega_{vec} = \omega_{vec}^* \cdot k_{nt}$
$R_{r\_er}^*$	Resistance in the rotor end ring	$R_{r\_er} = R_{r\_er}^*$
$R_{r\_bar}^*$	Resistance in the rotor bars	$R_{r\_bar} = R_{r\_bar}^* \cdot k_a$
$P_{cu\_s\_act}^*$	Copper loss in the stator slot	$P_{cu\_s\_act} = P_{cu\_s\_act}^* \cdot k_a$
$P_{cu\_s\_end}^*$	Copper loss in the end winding	$P_{cu\_s\_end} = P_{cu\_s\_end}^*$
$P_{cu\_r\_bar}^*$	Copper loss in the rotor bar	$P_{cu\_r\_bar} = P_{cu\_r\_bar}^* \cdot k_a$
$P_{cu\_r\_er}^*$	Copper loss in the end ring	$P_{cu\_r\_er} = P_{cu\_r\_er}^*$
$P_{yk\_hys}^*$	Hysteresis loss in the stator yoke	$P_{yk\_hys} = P_{yk\_hys}^* \cdot k_a \cdot k_{nt}$
$P_{yk\_eddy}^*$	Eddy current loss in the stator yoke	$P_{yk\_eddy} = P_{yk\_eddy}^* \cdot k_a \cdot k_{nt}^2$
$P_{yk\_exc}^*$	Excess loss in the stator yoke	$P_{yk\_exc} = P_{yk\_exc}^* \cdot k_a \cdot k_{nt}^{1.5}$
$P_{th\_hys}^*$	Hysteresis loss in the stator tooth	$P_{th\_hys} = P_{th\_hys}^* \cdot k_a \cdot k_{nt}$
$P_{th\_eddy}^*$	Eddy current loss in the stator tooth	$P_{th\_eddy} = P_{th\_eddy}^* \cdot k_a \cdot k_{nt}^2$
$P_{th\_exc}^*$	Excess loss in the stator tooth	$P_{th\_exc} = P_{th\_exc}^* \cdot k_a \cdot k_{nt}^{1.5}$
$Pf^*$	Power factor	$Pf = Pf^*$

The variables with stars represent the values from the base EM,  $m_a$  is the modulation index (0.95 in this thesis),  $U_{DC}$  is the DC-link voltage. Taking all the variables from the base EM and the scaling rules into consideration, a new scaled EM can be calculated.

Figure 2.16 demonstrates how the EM performance is affected with different number of turns and active length for a given DC link voltage while the current density is assumed to remain constant.



(a) Scaled EMs with different  $N_t$  and same active length



(b) Scaled EMs with different active length and same  $N_t$

**Figure 2.16** Scaling rules applied on an EM example

## 2.5 PM demagnetization analysis

Demagnetization in PM machines, whether induced by demagnetization magnetomotive force (MMF) or high temperature (rare-earth magnet), is a significant concern as it can escalate EM losses and degrade the system performance, particularly under high performance conditions [64][65].

Once demagnetization has occurred, a higher current is needed to achieve the same torque, which may increase the demagnetization MMF and potentially result in further demagnetization.

The PMSynRM is often designed with multilayer flux barriers with embedded ferrite magnets to improve its saliency and reluctance torque, as shown in Figure 2.2 (d). However, ferrite magnets exhibit a relatively low coercivity and remanence compared to their rare-earth counterparts. This makes ferrite magnets more susceptible to demagnetization under certain conditions. Furthermore, the behavior of these magnets under different temperatures differs significantly. Rare-earth magnets typically maintain their magnetic properties over a broader temperature range compared to ferrite magnets. Ferrite magnets experience a more significant decrease in magnetic performance at lower temperatures, leading to a higher risk of irreversible demagnetization [66].

The demagnetization curve depicted in Figure 2.17 illustrates the behavior of a ferrite magnet. When the flux density in the magnet falls below the flux density of the knee point, the magnet will suffer irreversible demagnetization.

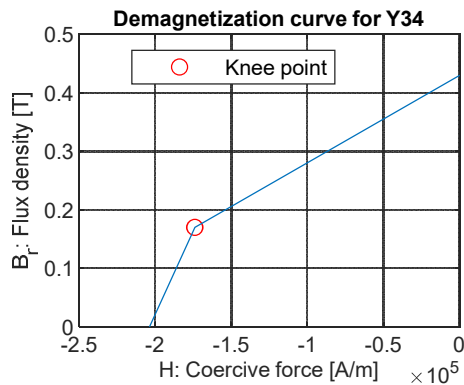


Figure 2.17 Demagnetization curves for Y34 @ 20 °C

The flux density distribution for PMSynRM models under different currents and rotor

positions is obtained through the FEA simulation. Two examples of the flux density distribution obtained for a particular PMASynRM are shown in Figure 2.18.

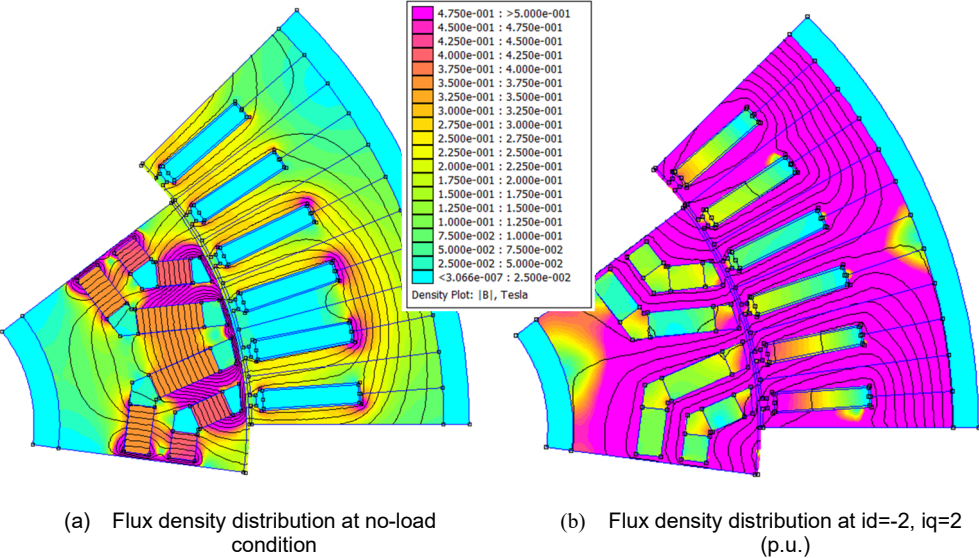


Figure 2.18 Flux density distribution under different operating conditions

It can be seen that the positions located at the edge of the magnets in the sides of the flux barrier are more susceptible to demagnetization under demagnetization MMF. Thus, the flux density data is collected on regions susceptible to irreversible demagnetization during the FEA simulations. The positions where the data is collected are presented in Figure 2.19.

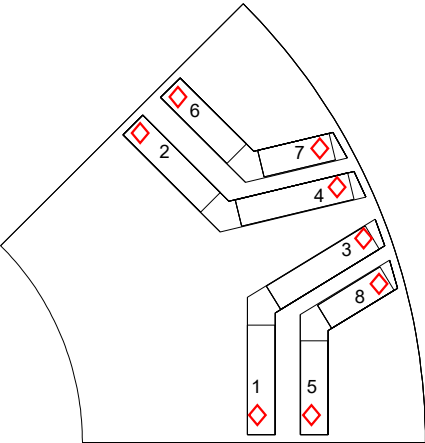


Figure 2.19 PMASynRM rotor with the data collecting positions



Figure 2.20 illustrates the flux density for all magnets at the selected positions under all current combinations for the PMSynRM example.

The yellow surface represents the flux density of the knee point at a temperature of 20°C, where the flux density threshold for irreversible demagnetization is 0.18 T. It's evident that the current in  $d$ -axis is the primary source of demagnetizing MMF. Additionally, due to cross coupling, the current in the  $q$ -axis also affects the demagnetization [67].

To prevent the irreversible demagnetization across all magnets, it is assumed that the maximum current for the stator is determined when the current operating point is below the knee point surface in Figure 2.18, denoted as  $I_{max}$ , representing the worst operating condition in this study.

That being said, in many applications surviving Active Short Circuit (ASC) is a key requirement for the EM. This operating condition can result in significantly higher  $-d$  currents (sometimes between 2-4 times higher than the peak operational current) which results into a higher risk of demagnetization. Such requirement can be included using the same procedure as above, but it is not considered for this thesis.

Considering the default number of turns for the base EMs as  $N_t^* = q * p$ , the maximum demagnetization MMF for each machine can be defined as follows.

$$MMF_{max} = N_t^* * I_{max} \quad (2.38)$$

Subsequently, the maximum allowed demagnetization MMF, ensuring the magnets remain free from the risk of irreversible demagnetization, is set as the maximum MMF of the stator. The process of demagnetization check is shown in Figure 2.21.

By incorporating the stator MMF limitation into the optimization process for PMSynRM, the analysis of the impact of demagnetization on powertrain performance can be initiated.

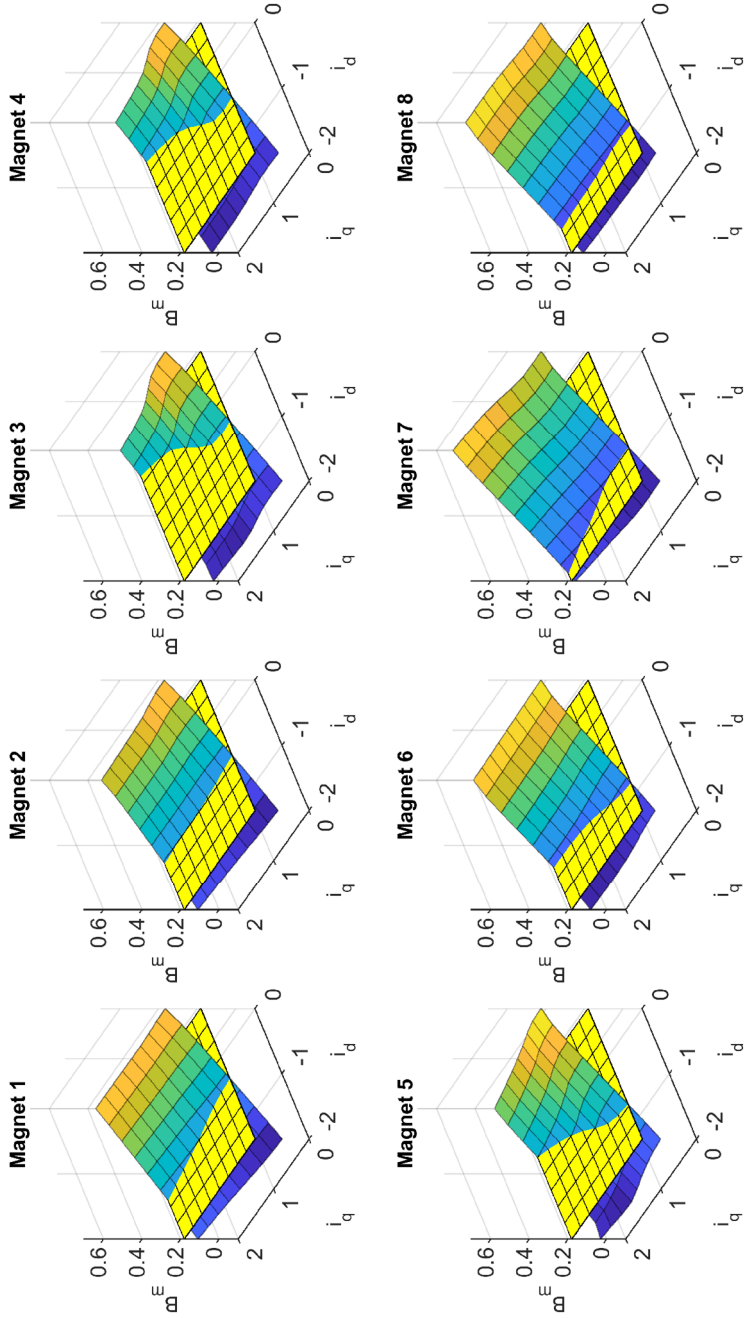


**Figure 2.20** Flux density for all magnets at the selected positions under all current combinations (p.u.)

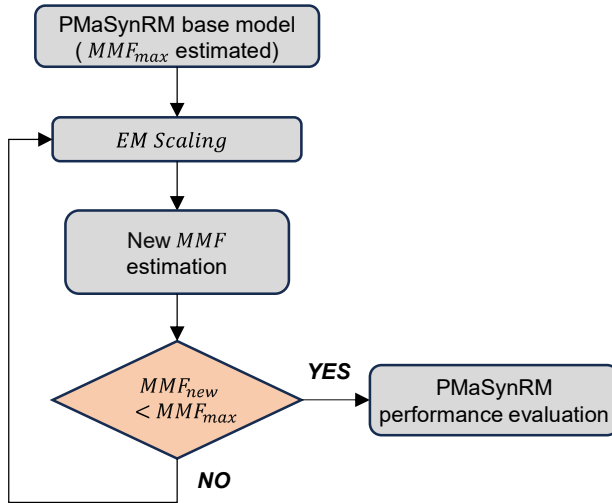


**Figure 2.21** Process of demagnetization analysis

## 2.6 EM performance validation

MotorCAD is a professional software dedicated to thermal and electromagnetic analysis for a wide range of machine types. To validate the proposed EM model based on FEMM, a double-V PMSM model with the same geometry and winding settings is created in MotorCAD as shown in Figure 2.22.

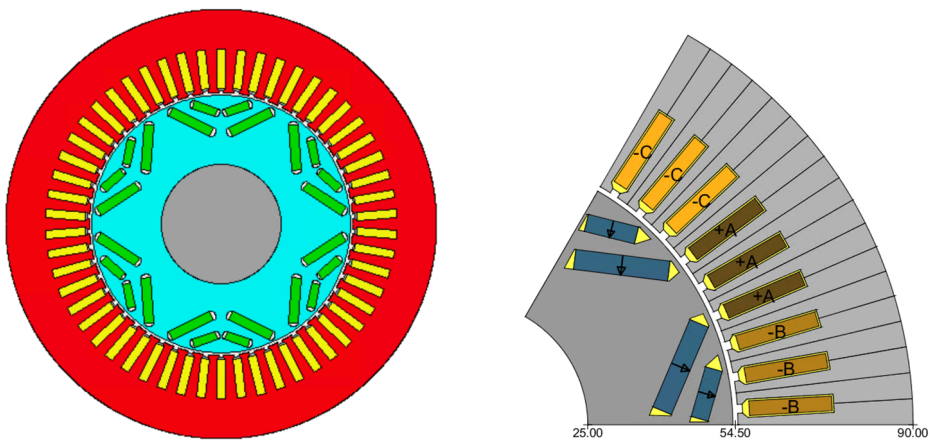


**Figure 2.22** EM geometry in MotorCAD and FEMM

Both EM models utilize identical material model parameters and maintain the same current rating. The EM model settings are listed in Table 2.5.

**Table 2.5. Model settings for selected EM**

<b>Parameters</b>	<b>Value</b>
DC-link voltage (V)	800
Peak current (Arms)	246
Lamination stack (m)	104
Num. of conductors in slot	8
Parallel path	2
Magnet material	N42UH
Lamination	M250-35A

As depicted in Figure 2.23, the peak torque achieved with the FEMM model reaches 199 Nm, whereas the MotorCAD simulation produces a peak torque of 196 Nm.

In the FEMM model, the method to estimate iron losses involves a simplified approach by collecting flux density data from the midpoint of the stator tooth and yoke. This method may not capture the complete picture of the iron losses throughout the EM stator, due to the flux density not being uniformly distributed in stator tooth and yoke. On the other hand, MotorCAD utilizes FEA technique to estimate the iron losses, offering a more precise evaluation. Consequently, the minor discrepancy in EM efficiency observed between the two models is largely attributed to the difference in iron losses.

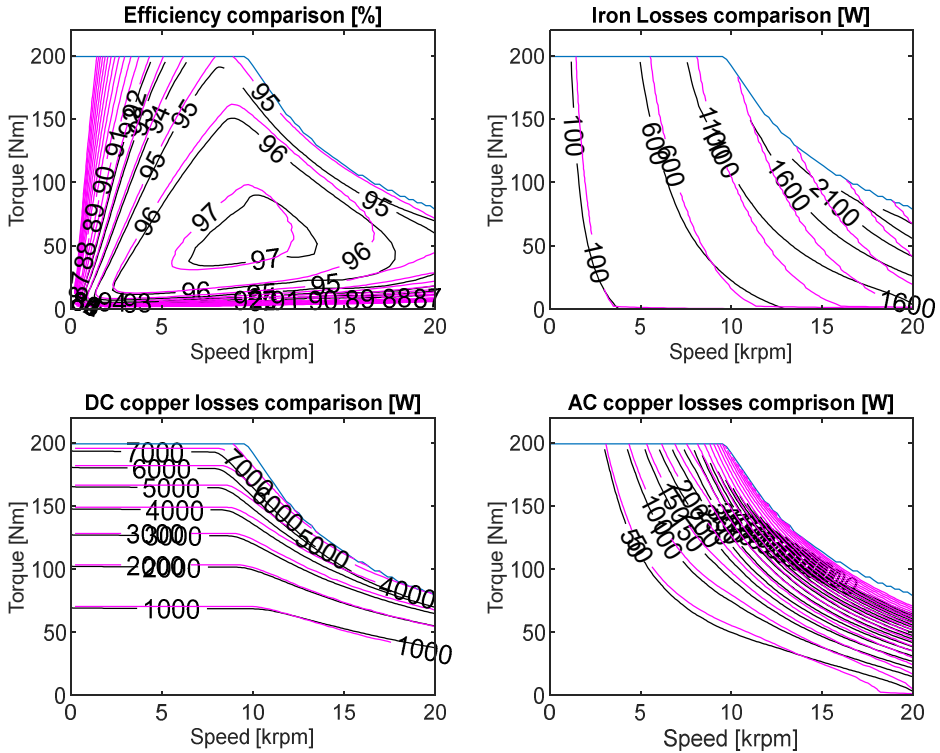


**Figure 2.23** Efficiency and losses comparison between FEMM (purple) and MotorCAD (black).

## 2.7 EM thermal model

In this study, 2D FE simulations are utilized and thus the end winding is not taken into consideration. However, from the thermal management perspective, it is crucial to note that the end winding is predominantly affected by the heat produced both by the winding in the slot and by the end winding itself, often leading to the end winding reaching the temperature limitation first. What is more, the thermal limitation determines the operational constraints for the EM. Exceeding these boundaries not only reduces the EM's lifespan but also poses a risk of failure. Conversely, maintaining a significant margin from these limits leads to an underutilization of the EM's potential. Thus, thermal modelling for EMs is essential in the process of EM design. When it comes to the powertrain optimization, which requires fast and accurate estimation of thermal performance for thousands of EMs with different geometries, the lumped parameter thermal model [68][69][70] is introduced.

The lumped parameter model employs a thermal network structure. Within this network, the components in the EM that tend to have similar temperatures are grouped (lumped) into a node. These nodes are connected with thermal resistances, which can be derived with the heat transfer mechanisms of conduction, convection, and/or radiation between different parts of EM.

### 2.6.1. Thermal model for PM machines

The thermal model for PM machines adopted in this study is depicted in Figure 2.24. This model exemplifies the thermal network of a PMSM equipped with a 6-layer hairpin winding. This example consists of 15 nodes which correspond to the outer case, the stator yoke and teeth, the conductors inside the slot (C1 to C6) and the end turns (EW1 to EW3), the magnets, shaft and bearings. The thermal resistances and capacitances are estimated based on the geometrical parameters and material properties.

The input parameters for the thermal model include iron losses for the stator yoke and teeth, as well as copper losses for each conductor within the slot and each end turn. Then the steady-state temperature and time to reach the temperature limitations can be estimated.

Then the temperature rise due to the heat generated by the losses can be calculated with (2.39),

$$\Delta T = G^{-1}P \quad (2.39)$$

Where  $\Delta T$  is the temperature rise of each node,  $P$  is the losses of each node and  $G$  represents the thermal conductivity matrix.

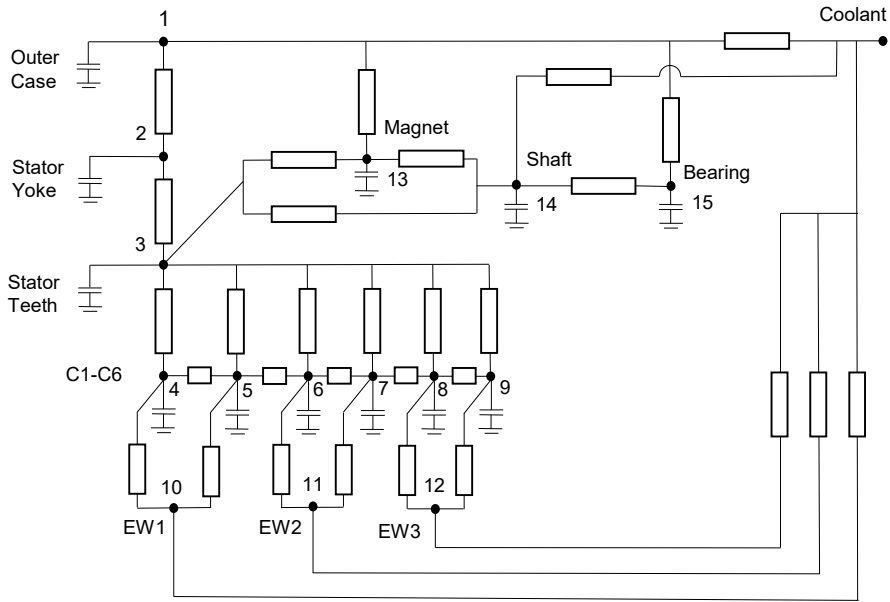


**Figure 2.24** Thermal lumped parameter model for PM machines

### 2.6.2. Thermal model for IM

Regarding the IM, the thermal model excludes the magnets, instead introducing the rotor bars and end ring into the analysis. It is important to note that the heat generation within the IM occurs on both the rotor and stator sides. As a result, an additional cooling method has been introduced specifically for the end ring. To simplify the model, the hairpin winding inside the dashed ellipse is not illustrated in Figure 2.25 but it is the same as the one presented in Figure 2.24.

In PM machines, the end windings are likely to be the first components that reach the maximum allowed temperature, while for IM, it is normally the rotor cage. The maximum operating temperature for the end windings in PM machines is set as 180°C. For the rotor cage in IMs, this thermal threshold is also set at 180°C. Regarding the heat dissipation, the heat transfer coefficient on the stator jacket of these machines is assumed to be 1400 W/m<sup>2</sup>K and 400 W/m<sup>2</sup>K for the shaft, 400 W/m<sup>2</sup>K for the end windings in PM machines, and 200 W/m<sup>2</sup>K for the end ring in IMs. It should be noticed that these can be easily altered to reflect different cooling solutions.

By utilizing this thermal model with the predefined thermal settings such as coolant temperature, heat transfer coefficient of the cooling system, and maximum allowed

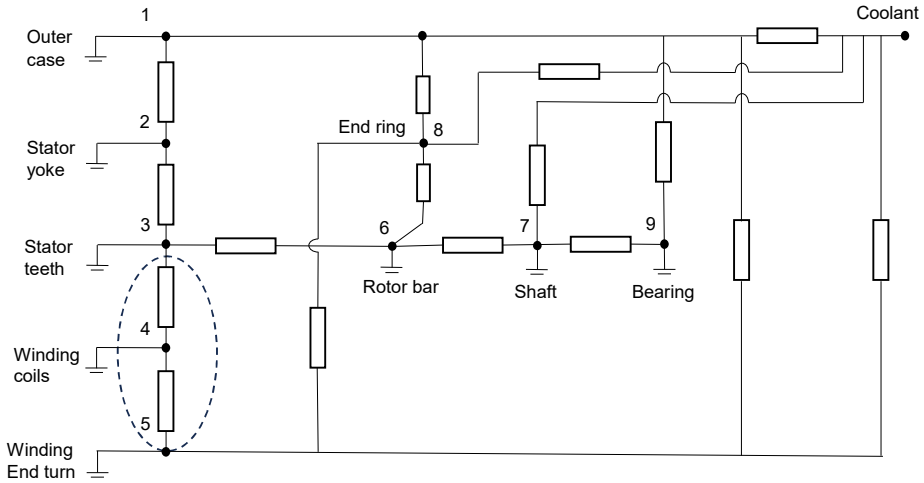


**Figure 2.25** Thermal lumped parameter model for IM

temperature, the current density of each scaled EM at nominal operating point can be estimated. With these data, the third scaling factor,  $k_{ov}$ , which is a value greater than 1, is used to determine the peak current of the EMs. This factor is essential in assessing the EMs' ability to handle transient or peak load conditions, which are often encountered in real-world, such as accelerating and overtaking.

It should be noted that the chosen heat transfer coefficient values serve as representative benchmarks to illustrate the impact of the thermal model. These coefficients are subject to several variations, including the flow rate of the coolant [70][71] and the specific structure of the cooling system. Despite these, the implementation of a thermal model facilitates a comparative analysis across EMs with diverse topologies. The introduction of the thermal model brings us better understanding of the intricate relationship between the EM topology and its thermal performance.

## 2.8 EM Cost model

The EM cost model is critical in the powertrain optimization process. It is important in optimizing material usage, which is particularly crucial in applications where the cost of materials contributes significantly to overall costs. Moreover, the cost model can help in quantifying trade-offs between various EM designs, enabling a good balance between performance and cost. High-performance EM designs may bring higher costs, however, with a comprehensive cost model, it becomes possible to identify the point at which the benefits of enhanced performance outweigh the additional cost.



Once the selected base EM is scaled, the EM cost model is used to estimate its manufacturing cost. The EM cost is determined by two primary factors: the cost of materials used in the EM and the cost of the major manufacturing operations involved in generating and assembling the physical components of the EM. The materials used in constructing the EM are significant determinants of its cost. For PMSMs, the cost of rare earth magnets constitutes a significant portion, often exceeding one third of the total cost of the EM. This is particularly significant considering the fluctuating and sometimes steep increases in rare earth material prices [72], as depicted in Figure 2.26.

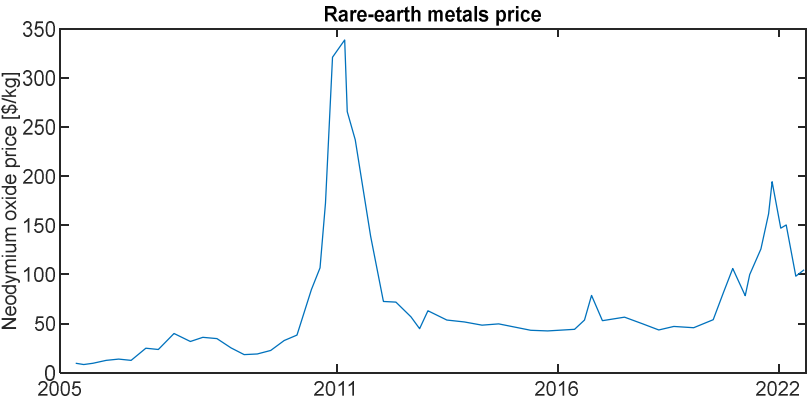


Figure 2.26 Rare earth material price trends [73]

The material price used for PM machines and IM in this thesis is listed in Table 2.5.

Table 2.5. Parameters of EM in the database

Material	Price (€/kg)
Lamination (M250-35A)	2.15
Copper	8.45 [74]
NdFeB (N42UH)	91
Ferrites (Y34)	5

In this thesis, the cost model is implemented based on the work in [20][75]. The cost of the EM is determined by summing up the expenses associated with each manufacturing process involved in its production. The cost evaluations for all manufacturing processes are represented by (2.40), a simplified version originally introduced in [76].

$$\begin{aligned}
k(x, N) = & \frac{K_A(x)}{N} + K_B(x) \frac{1}{1 - q_Q} + K_{CP}(x) \frac{t_0(x)}{1 - q_Q} \\
& + K_{CS}(x) \frac{t_0(x)q_s}{(1 - q_Q)(1 - q_s)} \\
& + K_D(x) \frac{t_0(x)}{(1 - q_Q)(1 - q_s)}
\end{aligned} \tag{2.40}$$

$k(x, N)$  represents the cost of a part of the selected EM under a certain manufacturing stage. This cost depends on the process itself  $x$  and the number of units  $N$  it produces. For each process, different input parameters are required to estimate its corresponding cost. They are investment cost in tooling  $K_A$ , cost of material  $K_B$ , quality loss  $q_Q$  (value between 1-0 representing rejection rate due to quality issues), cost during production  $K_{CP}$ , cycle time per operation  $t_0$ , cost during standstill  $K_{CS}$ , standstill fraction  $q_s$  (value between 1-0 representing the share of stand still time), and wage cost  $K_D$ .

The costs of parts produced in a process are counted as input materials when used in subsequent processes. The input materials for these operations can be sourced from one or more processes. For example, when inserting the conductors into the stator, the stacked stator and formed conductors are needed. Then the cost of material,  $K_B$  at process ‘conductor insertion’ should be the accumulated cost from the previous process conductor forming and the stacked stator, which can be expressed in (2.41).

$$K_B(x_{\gamma,0}, N) = \sum_{u=0}^v k(x_{\gamma-1,u}, N) \tag{2.41}$$

$x_{\gamma}$  and  $x_{\gamma-1}$  denotes the present and previous process order. The second index  $u$  denotes the number of process inputs needed to perform the present process.

Then the final cost can be expressed as (2.42):

$$\begin{aligned}
k(x_\gamma, N) = & \frac{K_A(x)}{N} + \sum_{u=0}^v k(x_{\gamma-1,u}, N) \frac{1}{1-q_Q} + K_{CP}(x_\gamma) \frac{t_0(x)}{1-q_Q} \\
& + K_{CS}(x_\gamma) \frac{t_0(x_\gamma)q_s}{(1-q_Q)(1-q_s)} \\
& + K_D(x_\gamma) \frac{t_0(x_\gamma)}{(1-q_Q)(1-q_s)}
\end{aligned} \tag{2.42}$$

Figure 2.27 shows the manufacturing process for both PM machines and IMs. The cost evaluation initiates with the detailed EM geometry and cost data. The cost data includes the tooling investment, cycle time, personnel, operational cost and yield data (material waste and quality) for each process.

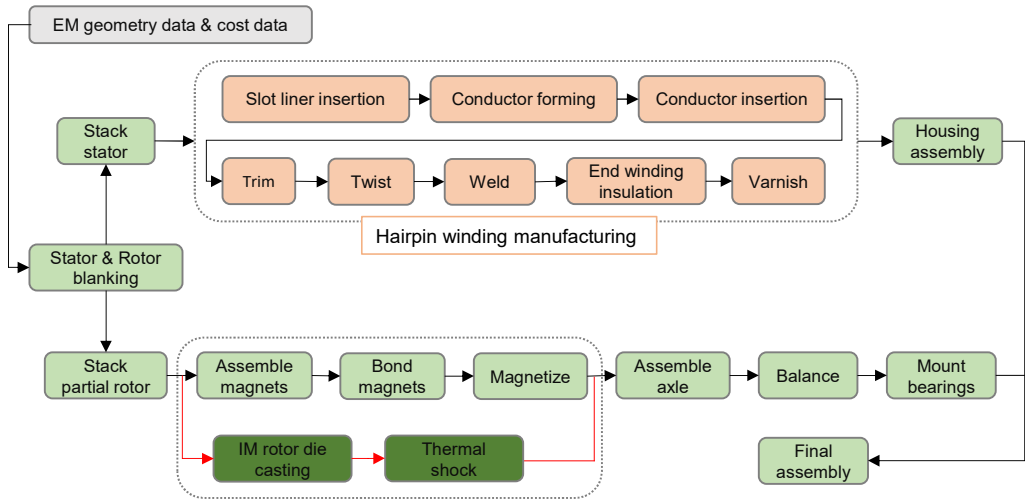


**Figure 2.27** Manufacturing process for EM

In contrast to conventional windings, hairpin windings are crafted from rectangular conductors that are shaped into a ‘hairpin’ configuration. These conductors are then inserted axially into the stator slots. The process is completed by twisting and welding their terminals to those of other coils.

For IM, the process related to magnets is disregarded. Instead, this is substituted by the die casting process for the rotor cage. Rotor die casting is a technique where melted metal is injected into a mold to form the rotor cage [78][79]. The material for the rotor cage varies

between copper and aluminium. IMs have been utilizing aluminium die cast due to its relatively low manufacturing costs. However, the cost advantage comes at a significant efficiency loss compared to the copper die cast. This is crucial in the automotive industry, where the powertrain system efficiency is highly valued. In this thesis, the copper die cast is applied with detailed cost information to estimate the IM total cost.

Figure 2.28 shows the material cost distribution and the EM cost distribution which includes both the material cost and manufacturing cost for a PMSM with a production volume of 10,000 units.

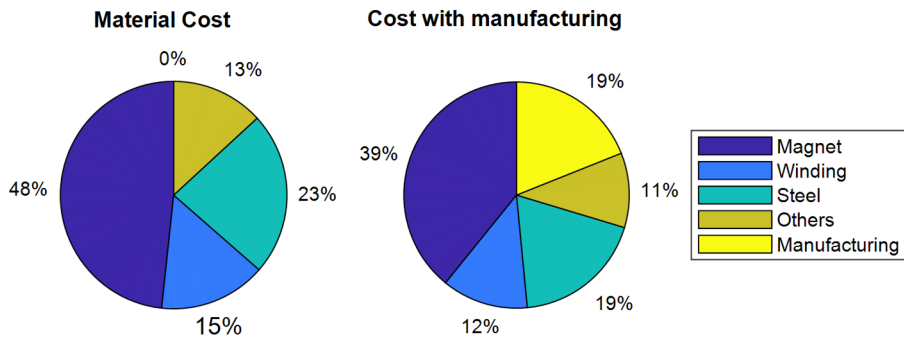


**Figure 2.28.** EM cost distribution with production volume of 10,000 units

As the fixed investment  $K_A$ , can be amortized by the total EM production, the EM cost is highly dependent on the production volumes. Figure 2.29 explores the relationship between the EM total cost and the production volumes. It highlights a critical insight: as production volume increases, the EM total cost decreases due to the larger economies of scale. However, it is important to note that the marginal reduction in EM cost begins to fade away beyond a certain production volume threshold.

Additionally, the EM cost model can effectively demonstrate the impact of varying the number of layers in hairpin winding on the overall EM cost. The winding configuration using eight conductors per slot exhibits a lower total copper mass due to their reduced filling factor compared to the same EM, with four- and six-conductor configurations. However, it is crucial to consider that the manufacturing process for 8-layer hairpin winding is more complex and time-consuming, translating into longer cycle times, subsequently escalating the manufacturing costs, which can be also seen in Figure 2.29.

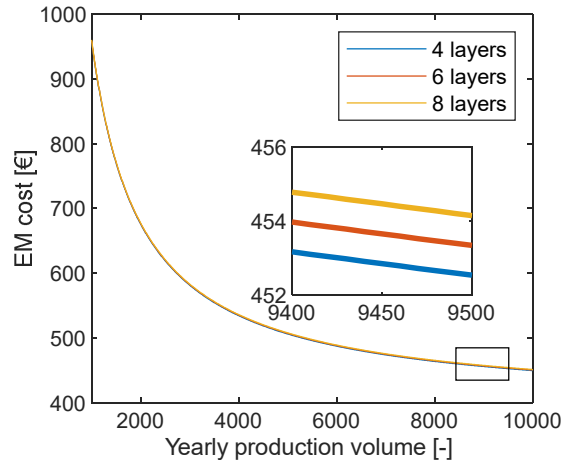


**Figure 2.29.** EM cost vs production volume

# Chapter 3 Transmission and PEC Modeling

When designing the electric powertrain for the EVs, achieving an optimal solution requires a broader perspective than simply evaluating the EM. This chapter explores deeper into the other two components in the powertrain, mechanical transmission and power electronics converter. This not only enhances our understanding about the powertrain but also paves the way for a more precise and comprehensive evaluation of its performance. By integrating these two components, it is possible to capture a holistic view of the overall system, shedding light on associated costs, efficiencies, and other important characteristics that might be overlooked.

## 3.1. Inverter design

In the electric powertrain, the inverter plays a crucial role in modulating and converting the direct current (DC) from the battery or energy storage system into alternating current (AC) required by the EM. In this study, the model of PEC should be computational efficiency to ensure that the powertrain optimization can be performed within a reasonable time. What is more, the model should be accurate enough in terms of losses estimation and component sizing. The main objective of the PEC model and internal optimization target is to find the optimum size, number of chips in the power module, as well as the DC-link capacitor and estimate their corresponding losses.

For EV applications, silicon (Si) and silicon carbide (SiC) power device are the two main choices for inverter applications. While Si is a traditional choice due to its cost-effectiveness and good performance in a range of conditions, SiC is increasingly favored in high-power and high-efficiency applications due to its superior properties, especially in terms of lower losses and its ability to handle higher temperatures and switching frequencies [80].

### 3.1.1 Electro-thermal model

This thesis employs the inverter model developed by Hannes Bydén, which is detailed in [17]. This model provides a comprehensive framework for the inverter design and optimization. The inverter model is adapted to be integrated within the powertrain optimization procedure presented in this thesis.

The inverter evaluation is based on a scalable electro-thermal model of power modules. For each PEC, the minimum semiconductor chip size is calculated with an iterative process by firstly calculating the semiconductor losses at the most challenging operating point (the peak current condition). The thermal resistance is estimated based on the power module materials and the chip size together with assumptions of heat spreading and chip-chip interaction. The junction temperature is then calculated from the losses and thermal resistance. SiC-MOSFET are used for the studies performed in this thesis, the power modules are assumed to be liquid cooled with a heat transfer coefficient of  $8 \text{ kW}/\text{m}^2\text{K}$ , the maximum allowed chip temperature is  $175^\circ\text{C}$  and the temperature of the coolant is set to  $65^\circ\text{C}$ . The capacitor is sized following the design rules presented in [81].

The scalable resistance, on-state voltage and switching losses are estimated by extracting data from manufacturer datasheets of several power modules from same generation and with the same packaging. Linear coefficients are used to compensate the turn-on, turn-off and on-state resistance dependence on junction temperature. The inverter design process is shown in Figure 3.1.

The design process begins with an assumption of the initial chip size ( $A_{chip}$ ). The voltage, current and power factor data derived from the EM model, combined with the calculated on-state resistance and voltage drop, allow for the calculation of semiconductor losses. The thermal resistance is estimated through an analytical model which has been validated against a 3D FEM model, enabling the estimation of chip temperature with execution time (several milliseconds) much shorter than 3D FEM. If the estimated temperature exceeds the maximum allowed temperature ( $T_{j,max}$ ), the chip size is increased. However, if the chip size exceeds a certain threshold, the number of chips ( $N_{chip}$ ) should be increased and placed in parallel until the junction temperature falls below the limitation. It is important to note that the losses at all operating points will be estimated to facilitate further system optimization.

The switching and conduction losses for the semiconductor (SiC-MOSFET) can be estimated by (3.1) and (3.2).

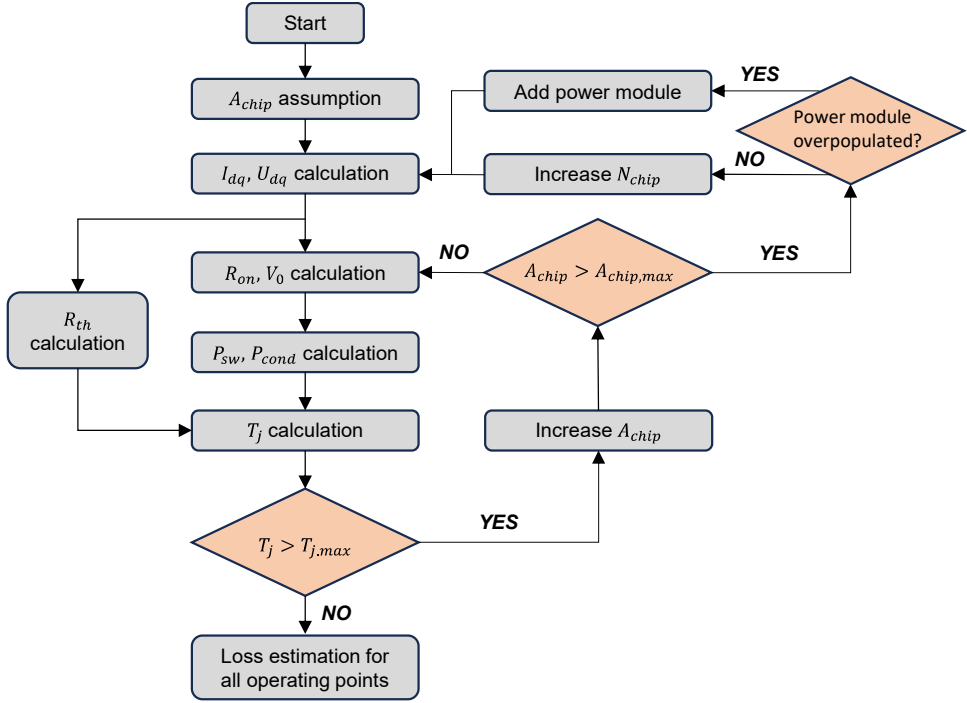


Figure 3.1: Flowchart of inverter design

$$P_{sw} = f_{sw} \cdot E_{ref}(I, A_{chip}) \cdot \left(\frac{V_{cc}}{V_{ref}}\right)^{K_v} \cdot \left(1 + T_c \cdot (T_j - T_r)\right) \quad (3.1)$$

$$P_{cond, fw(T)} = \left(\frac{1}{8} + \frac{m_a \cdot \cos(\phi)}{3\pi}\right) \cdot r_{on, fw}(A_{chip}, T_j) \cdot \hat{I}^2 \quad (3.2)$$

$$P_{cond, rv(T)} = \left(\frac{1}{8} - \frac{m_a \cdot \cos(\phi)}{3\pi}\right) \cdot r_{on, rv}(A_{chip}, T_j) \cdot \hat{I}^2 \quad (3.3)$$

In equation (3.1), the switching losses are estimated. The switching frequency is denoted as  $f_{sw}$ . The operating temperature and blocking voltage are represented by  $T_j$  and  $V_{cc}$ , respectively.  $T_r$  and  $V_{ref}$  are the reference values at which the energy losses are defined in the datasheet.  $T_c$  and  $K_v$  are the temperature and voltage compensation constant. The energy losses from the datasheet are represented by  $E_{ref}$ .



The conduction losses for MOSFET are computed by (3.2) and (3.3). MOSFET is assumed to be actively conducting in reverse during the freewheeling period. The losses are generated from both forward and reverse conduction, but with different on-state resistance  $r_{on, fw}$  and  $r_{on, rv}$ ,  $m_a$  is the modulation index,  $\cos(\phi)$  is the power factor of the EM,  $\hat{I}$  is the phase peak current of the EM.

### 3.1.2 Cost Model

After the main components of the inverter have been selected and optimized, the production cost of the inverter is calculated. The total PEC cost consists of the cost of subcomponents and the manufacturing related cost. The cost of many of these subcomponents is not sensitive with the power rating of the converter and then assumed to be fixed values [82]. The main cost driver is the semiconductors, and its cost is proportional to the chip area. The cost models for both the components and the manufacturing steps are developed based on the cost evaluation method for the EM and in close collaboration with experts from the automotive industry. The process to manufacture a PEC is shown in Figure 3.2.

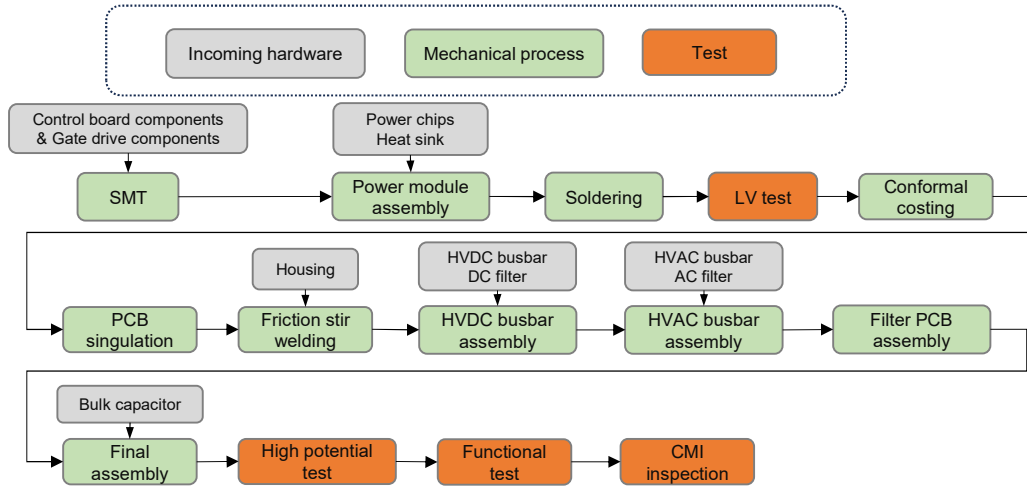


**Figure 3.2** PEC manufacturing process

Surface mount technology (SMT) refers to manufacturing technique where electronic components are directly applied to the surface of a printed circuit board (PCB). For each manufacturing process, the cost of material and corresponding manufacturing expense will be estimated with predefined cost data.

The cost model is benchmarked against example inverters from the automotive industry to ensure that the cost is representative for high-volume production.

The cost data for the components can be found in Table 3.1.

**Table 3.1 Component cost for PEC**

Component	Cost
Si-IGBT die	1 units/ mm <sup>2</sup>
Sic MOSFET die	3 units /mm <sup>2</sup>
DC-link capacitor	2 units / $\mu$ F

Based on the cost data, the cost distribution for one PEC example is shown in Figure 3.3. The main cost driver is the power module, and the manufacturing cost takes a considerable amount of the total PEC cost.

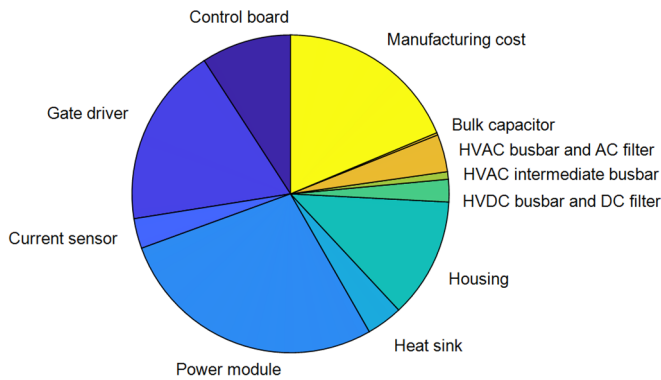


**Figure 3.3** PEC cost distribution

## 3.2. Transmission design

Mechanical transmission plays a crucial role in electric powertrains. It converts and adjusts the speed and torque from EM to the wheels. What's more, by adjusting the gear ratio, the transmission can help operate the EM within its most efficient operating point with the given drive cycle. The transmission model used in this thesis focuses on key component optimization, such as the gear design, which affects the efficiency and cost performance for

the transmission itself. There is also an optimization for the gear ratio to improve the EV's overall energy efficiency, extending the driving range under specific battery capacity.

### 3.2.1. MT Modelling

In this thesis, the transmission model is developed by [19], which includes the sizing of key components such as gears, shafts, and bearings, as well as the estimation of their power losses. The method is mainly developed by Borg Warner in collaboration with LTH and is summarized here for completeness. The primary goal of this transmission model is to simultaneously minimize both the mass of the transmission and its power losses.

The planetary layout and layshaft layout are two different designs used in transmission systems, primarily in automotive applications. A short overview of the different transmission layouts can be seen in Figure 3.4.

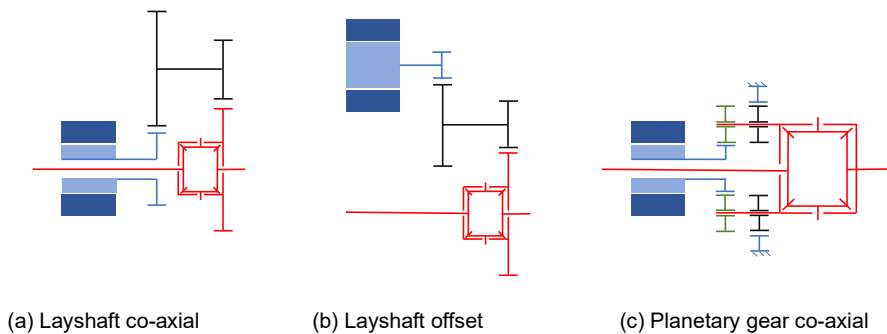


**Figure 3.4** Overview of different transmission layouts [83]

The layshaft layout, recognized for its affordability, good efficiency, and reduced complexity, has emerged as a popular choice for mass production in automotive industry. Meanwhile, co-axial solutions have a reduced package size as the entire system is aligned along the central axis. Although the co-axial planetary gear architecture presents the greatest complexity and requires the most effort for integration and manufacturing, thus cost the most among all candidates, its benefits are significant, mainly for the package space sensitive EV applications [83][84].

The transmission in a vehicle can be designed with either a single speed or multiple speeds. A single-speed transmission is much simpler in design compared to multi-speed transmissions, as it has fewer moving parts, leading to it being lighter and less expensive to manufacture. Additionally, single speed transmission can offer less wear and tear, lower maintenance costs, and increased reliability. Consequently, these advantages have led to the

single-speed transmissions being the dominant choice for passenger vehicles. However, there are EV applications using multi-speed transmission, benefiting from its ability to downsize the EM and make the EM operate in a more favorable efficiency range [85].

In this thesis, the focus is on single-speed and two-stage layshaft transmissions. Multi-stage layshaft is characterized by their arrangement of more than two offset gear-sets. A multi-stage layshaft transmission can achieve high overall gear ratios without having high gear ratios at each individual stage, leading to reduced size. The layout of this transmission, along with a description of the model inputs and outputs, are illustrated in Figure 3.5 and Figure 3.6.

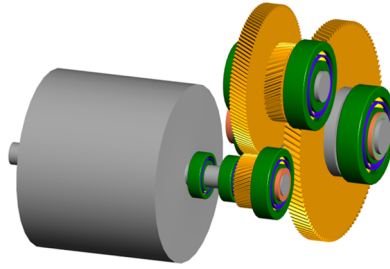


**Figure 3.5.** Structure of the single-speed with two-stage layshaft configuration transmission [19]

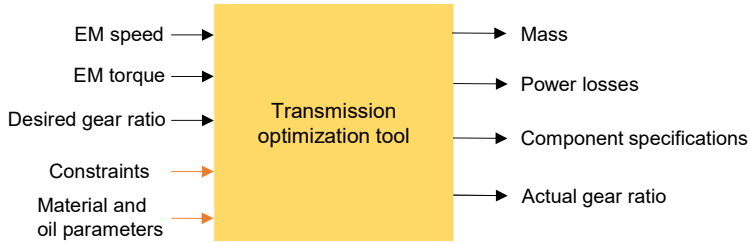


**Figure 3.6.** Inputs and outputs of the model

In the model, an iteration-based gear-set optimization process is introduced to find the trade-off between transmission mass and power losses. The total transmission mass is estimated by (3.4), which is adapted from [86].

$$M_{tot} = \pi\rho \sum_{n=1}^2 \frac{2(gr_n+1)T_{p,n}}{gr_n k_{0n}} \frac{(e_1+e_2 gr_n^2)}{4} \quad (3.4)$$

$$T_{p,2} = gr_1 T_{p,1} \quad (3.5)$$

$$gr_2 = gr/gr_1 \quad (3.6)$$

where  $T_{p,n}$  is the allowable torque on the shaft,  $k_{0n}$  is the allowable load intensity factor,  $\rho$  is the density of the gears,  $gr$  is the desired gear ratio for the transmission,  $gr_n$  is the gear ratio for each stage, and  $e_1$  and  $e_2$  is the volume coefficients of pinion and wheel, respectively.

As some parameters are fixed values, (3.3) can be simplified to (3.7) as follows.

$$M_{tot} \propto 2gr_1 + \frac{gr_1^2}{gr} + \frac{gr^2}{gr_1} + gr + 1 + \frac{1}{gr_1} + gr_1^2 \quad (3.7)$$

When the total desired gear ratio is defined, the partial gear ratios  $gr_1$  and  $gr_2$  will be determined by minimizing the total mass of the whole transmission with the iteration-based optimization.

The transmission losses are split up into load and non-load dependent losses. It mainly includes gear loaded losses, gear non-loaded losses, bearing loading losses, bearing non-loaded losses and losses caused by oil seals.

The gear loaded losses are primarily a result of friction in the gear mesh, which are related with the torque applied to the pinion, the rotational speed, and other mechanical properties as detailed in [87][88]. It can be expressed in (3.8).

$$P_{gr} = \frac{f_m T_p n_p \cos(\beta)^2}{9549M} \quad (3.8)$$

where  $P_{gr}$  is the mesh power loss,  $f_m$  is the mesh friction coefficient,  $T_p$  is the torque on the pinion,  $n_p$  is the rotational speed of the pinion,  $\beta$  is the operating helix angle, and  $M$  is the mesh mechanical advantage, which is a ratio of the force amplified by the gear mesh.

The bearing loaded losses are related with the bearing dynamic load, rotational speed and bearing type, as expressed in (3.9) and (3.10).

$$M_b = \frac{f_b P^i d_m^j}{1000} \quad (3.9)$$

$$P_b = \frac{M_b n}{9549} \quad (3.10)$$

Where  $f_b$  is the coefficient of friction,  $P$  is the bearing dynamic load,  $d_m$  is the bearing mean diameter, and  $i$  and  $j$  are exponents related with bearing type.

The non-load dependent losses within the transmission system consists of windage losses and oil churning losses [89][90]. These losses typically arise from the gear faces and tooth surfaces, influenced by factors such as the rotational speed, oil properties, how deep the gear is dipped in the oil.

$$P_{GW1} = \frac{1.474f_gvn^3D^{5.7}}{A_g10^{26}} \quad (3.11)$$

$$P_{GW2} = \frac{7.37f_gvn^3D^{4.7}b\frac{R_f}{\sqrt{\tan\beta}}}{A_g10^{26}} \quad (3.12)$$

Where  $P_{GW1}$  is the loss from the face of the gears,  $P_{GW2}$  is the loss from the tooth surface,  $f_g$  is the gear dip factor,  $\nu$  is the oil viscosity,  $n$  is the rotational speed of the element,  $A_g$  is the arrangement constant,  $R_f$  is the roughness factor,  $b$  is the total face width and  $D$  is the outside diameter of the element.

Given that the transmission model is expected to be executed millions of times during the powertrain optimization, its computational efficiency is critical. To address this, the model optimizes two key parameters: the normal module ( $m_n$ ) and the number of teeth ( $z_p$ ) for each gear. These parameters are important in defining the mechanical characteristics and performance of the transmission. Other design parameters such as the helix angle, pressure angle, and face width coefficient are maintained as constant values. These constants are chosen based on empirical experience and previously validated values, ensuring both reliability and practicality in the design process.

### 3.2.2. Desired gear ratio determination

To identify the optimal gear ratio for each stage of the transmission [91], the total desired gear ratio should be determined before designing and optimizing the transmission.

Given the specific drive cycle and vehicle specifications, which are described in detail in a subsequent section, achieving the desired gear ratio for the transmission involves an internal optimization process. This process utilizes the scaled EM and designed PEC, both of which should meet the vehicle's performance requirements. Then the internal optimization explores the optimal gear ratio among all feasible options, ensuring that the picked gear ratio of the MT, together with the EM and PEC, can offer the lowest energy consumption.

For single-speed transmission, the feasible gear ratios of the transmission are determined with satisfying the torque and speed requirements of the studied EV application, which is shown in (3.13).

$$\frac{T_{max,wheel}}{T_{max,EM}} \leq g_r \leq \frac{n_{max,EM}}{n_{max,wheel}} \quad (3.13)$$

During the internal gear ratio determination, the transmission efficiency is predefined as fixed values for all possible gear ratios, without evaluating the complete transmission model and achieving the corresponding efficiency maps. The use of pre-defined transmission efficiency is a compromise that the system efficiency can be estimated while keeping the computational time low.

Figure 3.7 shows an example of how desired gear ratio affects the system efficiency.

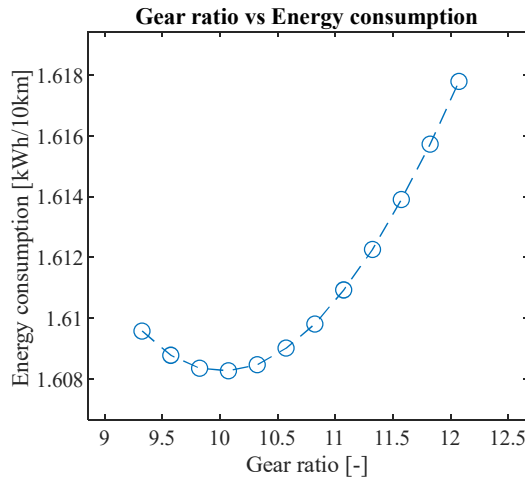


**Figure 3.7** Gear ratio vs energy consumption

It can be observed that among all feasible gear ratios, there is an optimal option bringing the lowest energy consumption by adjusting the EM to operate in its most efficient area.

### 3.2.3. Cost model

The cost estimation of the transmission is derived from a collection of data sourced from the transmission performance model. It contains extensive information of various components, including gears, shafts, bearings, and housing, etc. The cost data employed within the model is acquired directly from the suppliers, ensuring a high degree of accuracy. Additionally, the model incorporates the manufacturing process, providing a comprehensive view for the MT cost.

Similar to the EM cost model, the transmission cost consists of material and manufacturing cost, and the manufacturing process is illustrated in Figure 3.8.

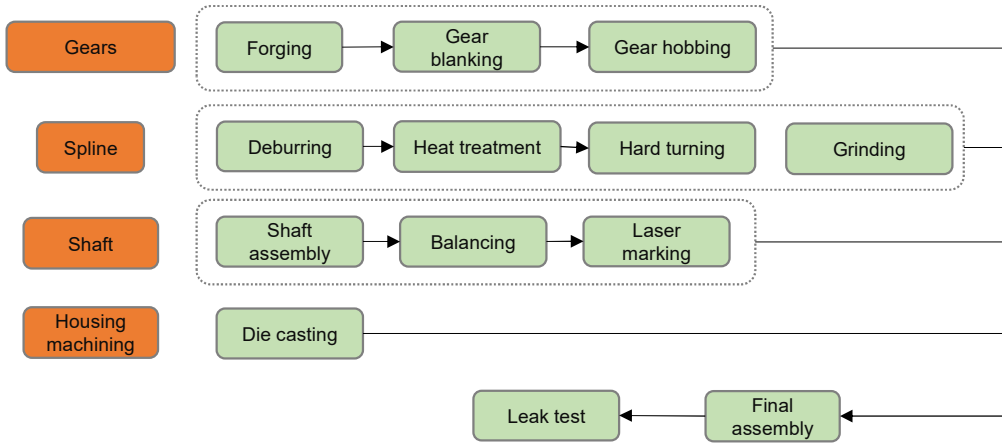


**Figure 3.8** Manufacturing process for transmission

Figure 3.9 (a) represents the transmission cost distribution with a production volume of 10,000 units. Figure 3.9 (b) illustrates the manufacturing cost, focusing on the cost associated with producing a single gear. This figure presents a more detailed perspective, highlighting the cost structure relevant to gear manufacturing.

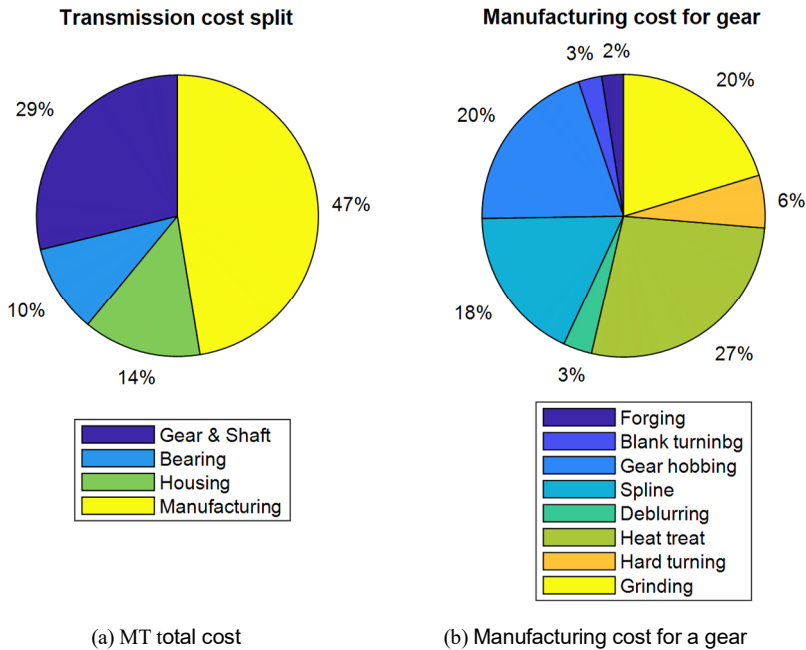


**Figure 3.9** Transmission cost





# Chapter 4 Optimization Methodology

As discussed in the introduction, in most cases optimizing the components in the powertrain individually and integrating them together does not lead to an optimal system design. The interactions between each component are often underestimated. For example, EV energy consumption is strongly influenced by the efficiency of all components of the powertrain. Hence the additional cost for a more efficient EM or inverter can often bring more competitive powertrain design.

However, due to high system complexity it is not possible for an expert to consider all relevant correlations for a holistic design with given requirements on vehicle level. Therefore, a system level powertrain optimization methodology is presented in this thesis.

The goal of the powertrain optimization is to provide a system design, including EM, PEC and MT, which should be able to satisfy all the vehicle requirements and design constraints, while minimizing or maximizing the objective function.

An overview regarding the structure and workflow of the optimization tool with the optimization target is shown in Figure. 4.1. The system optimization involves three steps:

- I. Optimization initialization: initial setups for all components should be made, including fixed settings such as cost data to evaluate each component cost, material selections, thermal settings, voltage level, etc. The base EMs with different 2D geometries in the database are the key inputs of the optimization process. The requirements of the EV under analysis should be evaluated before the optimization begins.
- II. System optimization: an optimizer is selected to explore the optimal solution by picking the design providing the minimum objective function (e.g. total cost of ownership) with parallel computing technique.
- III. With the obtained optimal and suboptimal powertrain designs, finer optimization exploration can be an option for the designer.

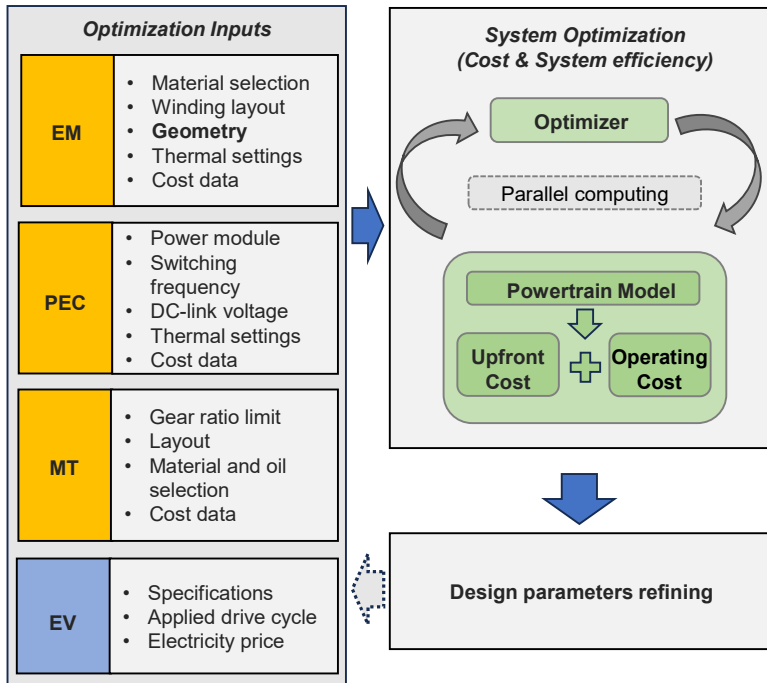


Figure 4.1 Structure of the powertrain optimization

A more detailed optimization process is illustrated, as shown in Figure 4.2.

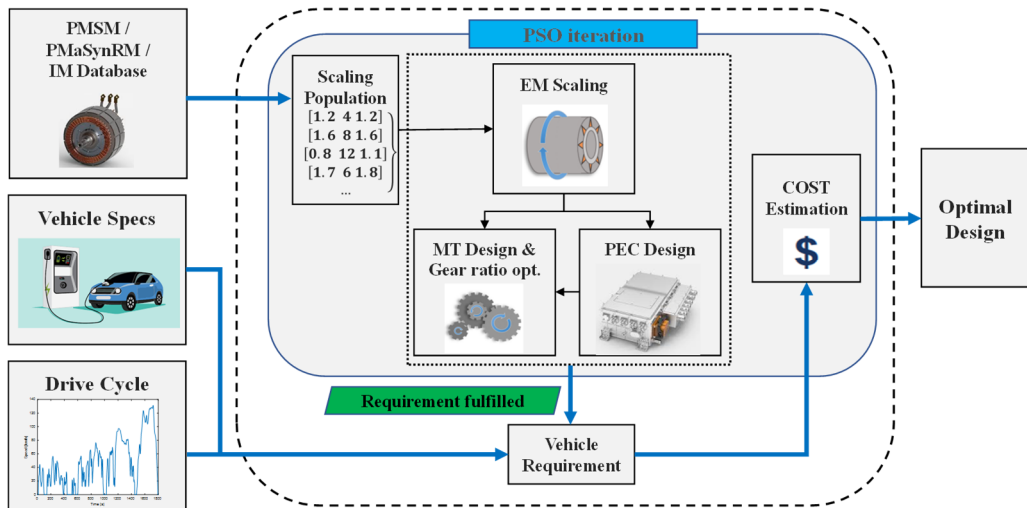


Figure 4.2. Optimization process

The input parameters for each component are set as fixed values except for the EM 2D geometry. The vehicle specification and the drive cycle are defined to evaluate the vehicle requirements and energy consumption. As one EM is selected from the database, the optimizer generates several particles with random or predefined positions (i.e., the values of the three scaling factors). How the optimizer works is introduced later in this chapter. Every time a particle changes its position in the search space, a scaled EM is generated together with the corresponding optimized PEC and MT design, and the new set of gear ratios is also optimized to minimize the energy consumption. If the powertrain design cannot satisfy the vehicle requirements and constraints ( $G_m$ ), this design is discarded. The powertrain cost and operating cost for the designs that meets all the requirements are calculated as the objective function. This process is repeated until the optimization converges to a minimum objective function value or the maximum iteration number is reached.

## 4.1. Optimization inputs

As depicted in Figure 4.1 and 4.2, the optimization framework integrates inputs from various components and the targeted application. The primary input for the EM is ‘base’ machines stored in the database with different 2D geometries. The generation of database of the EMs is discussed in Chapter 4.1.3. The data stored in an EM from the database contains all information needed for the further investigation, including torque, currents, all losses and other electromagnetic, mechanical and thermal data.

Supplementary parameters, including lamination and magnet materials, winding layouts, and cost data, are predetermined prior to initiating the optimization process. Furthermore, the framework allows for the selection of multiple alternatives, such as traditional versus hairpin winding techniques, IGBT or SiC semiconductors, and varying thermal management settings, etc. These selections enable a comprehensive comparative analysis within the optimization procedure. However, it is important to note that incorporating such a wide range of variables increases the computational time. This trade-off between computational efficiency and analytical depth must be carefully considered during the optimization process. In this study, a workstation with 32 cores is applied to run the optimization with parallel computing.

### 4.1.1. Powertrain configuration

Battery electric vehicles are propelled exclusively by electric powertrains, drawing power from onboard batteries that can be recharged from external electrical sources. There are

variations in BEV powertrain configurations, mainly between two-wheel-driven (2WD) and four-wheel-driven (4WD) systems.

For 2WD BEVs, the powertrain can either be front-wheel drive (FWD) or rear-wheel drive (RWD), which can be seen in Figure 4.3 (a) and (b). FWD BEVs have their EM or EMs mounted at the front, driving the front wheels. This configuration is often preferred for its efficiency in space utilization and cost-effectiveness, making it a common choice for compact and city cars. On the other hand, RWD BEVs feature the EM or EMs at the rear, driving the rear wheels. This setup is typically favored for performance-oriented vehicles, as it provides higher traction and a more even weight distribution, which is advantageous for acceleration and cornering dynamics [92].

4WD BEVs employ a dual-motor setup, with each pair of wheels being driven by its own powertrain, shown in Figure 4.3 (c). This configuration allows for superior traction performance [93]. A good selection of powertrain configuration and torque distribution management between two powertrains can also bring better system efficiency performance and potential cost reduction. While 4WD EVs tend to be more complex and expensive than their 2WD counterparts, they are often found in higher-end BEV models.

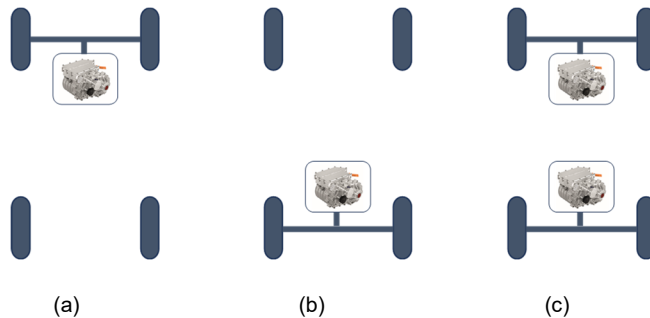


**Figure 4.3** Powertrain configurations

In summary, the choice between FWD, RWD, and 4WD in BEVs is largely dictated by the desired balance between cost, performance, and driving conditions, with each configuration offering its own set of advantages. As the EV market continues to grow, these diverse powertrain options enable a wide range of EV applications to cater to various consumer preferences and needs.

### 4.1.2. EV requirements

The vehicle requirements are the fundamental input of the optimization process. These requirements primarily include two aspects: the peak and continuous power, and the peak and continuous torque at different speeds. The peak power and torque are essential for enabling the vehicle to accelerate from 0 to 100 km/h in a matter of seconds. Continuous torque, on the other hand, ensures the vehicle maintain certain speeds on both flat and sloped roads for a long time.

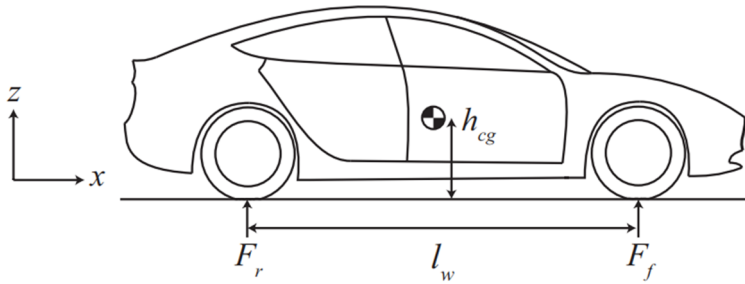


**Figure 4.4** Vehicle layout [20]

The acceleration ability of an EV is influenced by several factors. The power and torque generated by the electric powertrain are fundamental in determining its acceleration. Higher output torque of the powertrain, especially at low speeds, contributes to quicker acceleration. The grip or traction of the tires on the road surface, which is called adhesive force, also affects the acceleration. It allows for higher torque transfer to the road without tire slip.

Given a RWD EV and a flat road, the adhesive force can be defined as the maximum force that the tire can exert against the ground. This force can be calculated by (4.1).

$$F_{\phi\_RWD} = \frac{m_u M_v g (l_f - f h_{cg})}{l_w - m_u h_{cg}} \quad (4.1)$$

For a FWD EV, the adhesive force can be estimated by (4.2).

$$F_{\phi\_FWD} = \frac{m_u M_v g (l_r + f h_{cg})}{l_w + m_u h_{cg}} \quad (4.2)$$

Where  $m_u$  is the friction coefficient,  $M_v$  is the vehicle's weight,  $g$  is the gravity,  $h_{cg}$  is the height of the centroid of the vehicle,  $l_w$  is the wheelbase,  $l_f$  is the length between the centroid and front wheel,  $l_r$  is the length between the centroid and rear wheel. As the rolling resistance ( $f$ ) is relatively small,  $l_f - fh_{cg}$  and  $l_r + fh_{cg}$  can be approximated to  $l_f$  and  $l_r$  respectively. This reveals that RWD EVs have an advantage over FWD vehicles in terms of acceleration, as they can sustain higher traction torque before the tires slip.

For 4WD EVs, the mass of the vehicle can be fully utilized, so the maximum traction force is dependent on friction coefficient in (4.3).

$$F_{\varphi\_4WD} = m_u M_v g \quad (4.3)$$

By this, a rough estimation of the acceleration time limit for 4WD vehicles can be made without introducing customized tires or an extra aerodynamic kit.

$$t_{ACC\_4WD\_lim} = 2.83/m_u \quad (4.4)$$

To maximize the utilization of this traction limit (i.e., the adhesive force), it is assumed that the peak torque requirement equals the traction limit. The peak torque requirement determines the powertrain output torque, thus the size of each component, especially for the EM or EMs. The base speed of the EM can be found by minimizing the maximum power that meets the acceleration requirement. The continuous torque requirements [94] can be estimated with different speed and road slope combinations. Figure 4.5 illustrates the peak and continuous torque requirements on wheel side for a RWD EV example.

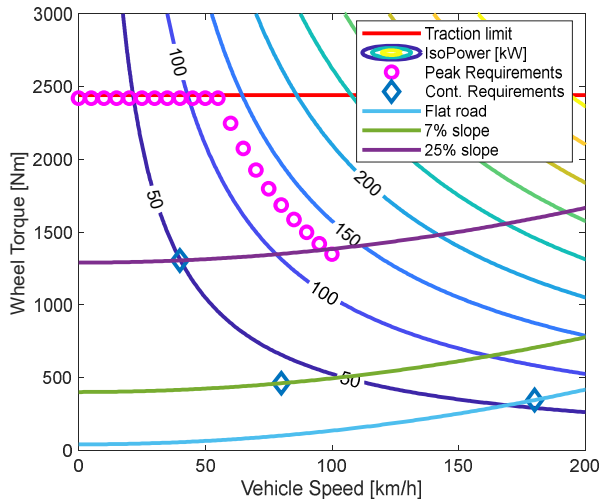


**Figure 4.5** Wheel torque requirements for a RWD EV

### 4.1.3. EM database

As mentioned in Chapter 2, for different EV applications, the requirements for the EM or EMs are diverse, covering electromagnetic performance, thermal behaviour, efficiency performance and cost considerations. Considering the various constraints and requirements, a large-scale exploration for the EM design is required. This thesis provides a method to generate databases for PMSM, PMSynRM, and IM with various 2D geometries. The aim of creating these databases is to provide an extensive design space, thereby enabling an optimization algorithm to effectively search for and identify the optimal EM configurations for specific EV applications.

In Chapter 2, the EM topologies and the geometry parameter definitions are clearly illustrated. A list of the parameters varied to generate the databases for the four different EM topologies is shown in Table 4.1.

**Table 4.1. Parameters to generate the database**  
**Single-V shape PMSM**

Parameter	Values	Units
$r_{so}$	[90 100 110 120]	mm
$r_{ro}/r_{so}$	[0.6 0.65]	-
$N_p$	[6 8]	-
$q$	[2 3]	-
$K_{iron}$	[0.95 1 1.05]	
$d_{pn}$	[0.06 0.08 0.1 0.12]( $2\pi r_{ro}/N_p$ )	mm
$d_{mi}$	[0.4 0.45 0.5]( $r_{ro} - r_{ri}$ )	mm
$h_{pm}$	[4.5 5 5.5 6]	mm

**Double-V shape PMSM**

Parameter	Values	Units
$r_{so}$	[90 100 110 120]	mm
$r_{ro}/r_{so}$	[0.6 0.65]	-
$N_p$	[6 8]	-
$q$	[2 3]	-
$K_{iron}$	[0.95 1 1.05]	
$d_{pn1}$	[0.06 0.08 0.1]( $2\pi r_{ro}/N_p$ )	mm
$d_{mi1}$	[0.4 0.45 0.5]( $r_{ro} - r_{ri}$ )	mm
$d_{pn2}$	[0.06 0.08 0.1]( $2\pi r_{ro}/N_p$ )	mm
$d_{mi2}$	[0.4 0.45 0.5]( $r_{ro} - r_{ri}$ )	mm
$h_{pm}$	[4 5 5.5]	mm



**PMSynRM**

Parameter	Values	Units
$r_{so}$	[90 100 110 120]	mm
$r_{ro}/r_{so}$	[0.6 0.65]	-
$N_p$	[6 8]	-
$q$	[2 3]	-
$K_{iron}$	[0.95 1 1.05]	
$n_{hl}$	[2 3]	mm
$\beta$	[0.4 0.45 0.5]( $r_{ro} - r_{ri}$ )	mm
$h_{pm}$	[4.5 5 5.5 6]	mm

**IM**

Parameter	Values	Units
$r_{so}$	[90 100 110 120]	mm
$r_{ro}/r_{so}$	[0.6 0.65]	-
$N_p$	[4]	-
$q$	[4 5]	-
$K_{iron}$	[0.95 1 1.05]	
$N_{bar}$	[30 34 38 42 46 50 54 58 62 66 70 74]	mm
$A_{bar}$	[0.1 0.12 0.14]	mm

The parameters not listed in the tables are set as fixed values. It is important to highlight that the decision to fix certain geometry parameters is primarily driven by considerations of computational efficiency. Conducting analysis with these parameters as variables is feasible but would require significantly greater computational resources. Such analysis could be effectively implemented using more powerful workstations or leveraging cloud computing capabilities.

Upon incorporating these parameters, the total number of different 2D EM geometries is 1152 for Single-V PMSM, 2592 for double-V PMSM, 864 for PMSynRM and 900 for IM.

The complete process to generate the database is shown in Figure. 4.6. All the base EMs in the database are stored in Matlab as mat files for further optimization.

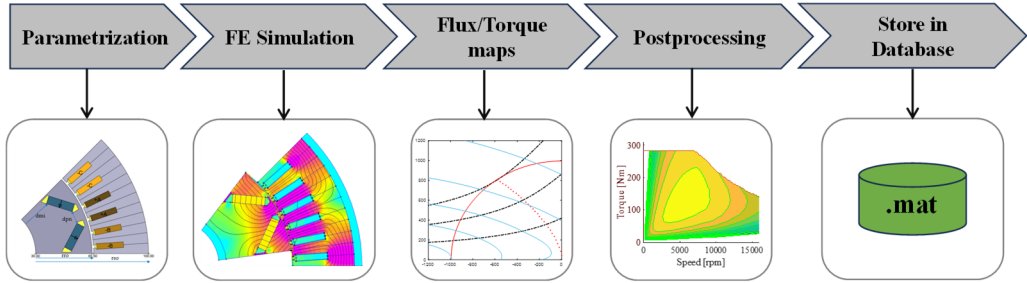


**Figure 4.6** Electrical machine database generation

## 4.2. Objective function

The objective function to be optimized can be various powertrain properties. These properties include, but are not limited to, individual component costs, overall powertrain cost, system efficiency, total system weight, etc. The prioritization of these attributes varies according to the intended EV application.

For instance, for cost-sensitive EV applications, the emphasis is often placed on minimizing the total cost of the powertrain. This often leads to the selection of EMs that utilize less or no rare-earth magnets, such as PMaSynRMs or IMs. However, this cost-driven choice may result in a trade-off with system efficiency. The lower or non-utilization of rare-earth materials in these EMs can potentially diminish system efficiency, subsequently increasing overall energy usage and require a larger battery capacity, thus increasing the operational cost.

It is essential to recognize that such decisions in powertrain design involve a complex relation, where optimizing one aspect may lead to compromises in another. Consequently, the selection of optimization objective must be carefully aligned with the specific performance and economic considerations of the EV application. What's more, due to the system complexity, it is not possible for the designer to consider all relevant aspects when designing the powertrain. Therefore, a multi-objective function is selected in this thesis, as expressed in (4.5).

$$f(x) = \sum_{i=1}^n k_i f_i(x) \quad (4.5)$$

Where  $f(x)$  is the objective function,  $f_i(x)$  is the sub-objective (powertrain cost, operating cost, etc.),  $k_i$  represents the weighting factor for each objective. It should be noted that the sum of  $k_i$  equals to 1.

When optimizing a drivetrain this way, the parameter sets are likely to be different for e.g. a normal car vs a sports car, a private car vs a bus or a truck etc. The setting of the weighing factors is thus not a purely technical choice.

#### 4.2.1. Powertrain cost

Powertrain cost consists of cost of each key components in the system, as shown in (4.6).

$$C_{PT} = C_{EM} + C_{PEC} + C_{MT} \quad (4.6)$$

Where  $C_{EM}$ ,  $C_{PEC}$  and  $C_{MT}$  represents the cost for EM, PEC and MT, respectively. It should be noted that the cost for all components is achieved under the same production volume and manufacturing cost assumptions.

In the automotive industry, the research and development (R&D) expenses for powertrain systems constitute a significant portion of the overall investment, directly impacting the final pricing of EVs. More details will be discussed when dealing with platform-based powertrain optimization in Chapter 6.

#### 4.2.2. Operating cost

The operating cost is estimated based on the energy consumption over one year and the energy price. Before evaluating the energy consumption for the vehicle, a drive cycle should be introduced.

The selection of a drive cycle for estimating the energy consumption of EVs is a critical step in understanding and predicting their real-world performance. The selected drive cycle should accurately represent the typical driving conditions the EV is expected to encounter. For instance, the New European Driving Cycle (NEDC) and the Worldwide Harmonized Light Vehicles Test Procedure (WLTP) [95] are commonly used in Europe, while the U.S. uses the EPA's drive cycles and China Light-duty vehicle Test Cycle (CLTC) is used in China.

The intended use of the EV plays a crucial role in drive cycle selection. For example, a commercial delivery EV would require a different cycle compared to a passenger vehicle, due to different load conditions and stop-start patterns. In this thesis, the passenger EV is studied and the WLTP drive cycle is applied. The drive cycle can be used to estimate energy

consumption with analytical method or a simulation tool. The curve generated with Simulink-based driver model shows a mismatch in speed with the reference drive cycle, as depicted in Figure 4.7. Despite this discrepancy, the impact on the overall energy consumption is minimal when compared to the results obtained using the analytical method.

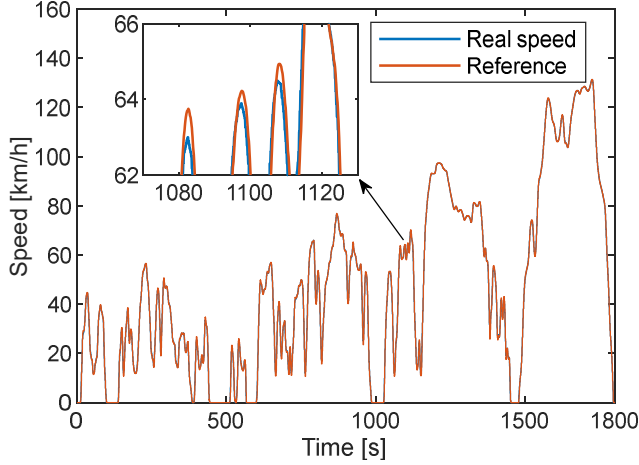


**Figure 4.7.** Reference speed of WLTP drive cycle vs Speed with Simulink model.

Estimating the energy consumption of an EV using the selected drive cycle also requires the EV specifications, including its weight, aerodynamic drag coefficient, rolling resistance coefficient, and powertrain efficiency, etc.

Due to the consideration of computational time, the analytical method is used to estimate the energy consumption, expressed in (4.7)-(4.10).

$$P_{wheel}(k) = (ma(k) + mg \sin \theta + mg C_r \cos \theta + \frac{1}{2} C_d \rho A_v v^2(k))v(k) \quad (4.7)$$

$$P_{Batt}^+(k) = P_{wheel}(k) + P_{EM}(k) + P_{Inv}^+(k) + P_{MT}(k) \quad (4.8)$$

$$P_{Batt}^-(k) = P_{wheel}(k) - P_{EM}(k) - P_{Inv}^-(k) - P_{MT}(k) \quad (4.9)$$

$$EC = \sum_{k=0}^n (P_{Batt}^+(k) + P_{Batt}^-(k)) \Delta t \quad (4.10)$$

Where  $P_{wheel}(k)$  is the power delivered to the wheels at instant  $k$ ,  $P_{Batt}^+(k)$  and  $P_{Batt}^-(k)$  are the power delivered by the battery at instant  $k$  in motor and generation modes respectively,  $m$  is the mass of the vehicle,  $a(k)$  is the vehicle acceleration at instant  $k$ ,  $g$  is

the gravity acceleration,  $\theta$  is the angle of the road,  $C_r$  is the rolling resistance coefficient,  $C_d$  is the air drag coefficient,  $\rho$  is the density of air,  $A_v$  is the frontal area of the vehicle,  $v(k)$  is the vehicle speed at instant  $k$  and  $EC$  is the energy consumption over the drive cycle, Finally, the operating cost is estimated by the product of the total annual distance travelled, the energy consumption per kilometer and the energy (electricity) price.

### 4.3. Optimizer

In the context of powertrain optimization for EVs, the role of the optimizer is critical. Once the objective function is set, the optimizer can explore the potential design space, which includes all possible combinations of powertrain components. This exploration is to identify the optimal design that meets the requirements and constraints. In this thesis, the EM design space refers to the base EMs in the database and all feasible scaled EMs for each EM topology.

In any optimization process, there are trade-offs to be considered. The optimizer evaluates these trade-offs to understand the impact of prioritizing one objective over another, such as the trade-off between cost and efficiency. The optimization is often an iterative process. The optimizer uses algorithms to iteratively refine the design, gradually moving towards an optimal solution. It assesses each iteration against the objective function and constraints, and then makes the necessary adjustments. The choice of the optimization algorithm decides how effectively and efficiently the optimizer can find the best solution.

In this work, particle swarm optimization (PSO) is used as the optimizer. It is known to effectively solve large-scale nonlinear optimization problems [96]. In this work, the optimizer has three dimensions (variables): the axial scaling factor  $k_a$ , the number of turns  $N_t$  and the overloading factor  $k_{ov}$ , which are the inputs for the scaling process. The values of these three variables and resulted powertrain design should respect some boundary conditions as below.

**Optimization Target:**  $\min ( f(EM_{ind}, x) )$

$$x = (k_a, N_t, k_{ov})$$

$$s. t: k_a > 0, \quad k_a \in R$$

$$N_t > 0, \quad N_t \in N_{t\_feasible} \tag{4.11}$$

$$k_{ov} > 1, \quad k_{ov} \in R$$

$$G_m(x) > 0$$

Where  $f(EM_{ind}, x)$  is the objective function,  $EM_{ind}$  is the index of the EMs in the database,  $x$  is the vector representing the scaling factors.  $G_m$  represents all powertrain specific constraints such as overloading time limit ( $t_{ov}^*$ ), desired gear ratio boundary ( $g_r^*$ ), maximum allowed temperatures for winding ( $T_{wind\_max}^*$ ), etc. The constraints are expressed in (4.12).

$$G_m(x) = \begin{cases} t_{ov} - t_{ov}^* \\ g_r^* - g_r \\ T_{wind\_max}^* - T_{wind} \\ P_{max} - P_{max}^* \end{cases} \quad (4.12)$$

The vehicle requirements are compared against the performance of the designed powertrain. Any powertrain configuration that fails to meet the requirements is consequently eliminated from consideration.

Before initiating the optimization, the search space will be predefined by (4.11). Assuming there are  $N$  particles, the position of particle  $i$  at iteration  $t$  is defined as in (4.13),

$$X_i(t) = (X_i^{k_a}(t), X_i^{N_t}(t), X_i^{k_{ov}}(t)) \quad (4.13)$$

Besides the position, the velocity for each particle is defined as in (4.14),

$$V_i(t) = (V_i^{k_a}(t), V_i^{N_t}(t), V_i^{k_{ov}}(t)) \quad (4.14)$$

At the next iteration, the position of each particle will be updated as

$$X_i(t+1) = X_i(t) + V_i(t+1) \quad (4.15)$$

and the velocity is updated by the rule (4.16).

$$V_i(t+1) = \omega_{inertia} \cdot V_i(t) + C_1 \cdot rand \cdot (X_{best,i} - X_i(t)) \\ + C_2 \cdot rand \cdot (X_{best} - X_i(t)) \quad (4.16)$$

Where  $\omega_{inertia}$ ,  $C_1$  and  $C_2$  are used to make the particles move to control the algorithm's performance,  $rand$  is a random number between 0 and 1,  $X_{best,i}$  is the position that gives the best  $f(EM_{ind}, x)$  explored by particle  $i$ ,  $X_{best}$  is the position that gives the best objective function explored by all particles.

The inertia weight factor,  $\omega_{inertia}$ , is between 0 and 1. It determines how much should the particle keep on with its previous velocity. The parameters  $C_1$  and  $C_2$  are called the

cognitive and the social coefficients respectively. They control how much weight should be given between refining the search result of the particle itself and recognizing the search result of the whole swarm.

# Chapter 5 Comparison analysis for PMSM, PMaSynRM and IM from system level

In this chapter, a comparison between three EM topologies (PMSM, PMaSynRM and IM) in an optimized EV powertrain perspective is made. In this comparison all powertrain systems fulfil the same wheel performance requirements, and the MT and the PEC are optimized together with the selected EM type. The thermal performance is considered throughout the optimization process to ensure a fair assessment across all topologies. The sum of the powertrain cost and the operating cost are used as the objective function.

The optimization methodology and detailed optimization process is explained in Chapter 4. The optimization inputs for this case study are illustrated in this chapter.

## 5.1. Vehicle Specifications and optimization targets

The target application in this study is selected to be a RWD electric passenger car. The specifications can be seen in Table 5.1.

**Table 5.1 Vehicle specifications**

<b>Parameter</b>	<b>Value</b>	<b>Unit</b>
Vehicle mass	1850	<i>kg</i>
Wheel radius	0.35	<i>m</i>
Drag coefficient	0.26	-
Rolling coefficient	0.008	-
Front area	2.36	<i>m</i> <sup>2</sup>
Top speed	180	<i>km/h</i>
Acceleration (0-100km/h)	7	<i>s</i>



Based on the specifications, the required peak wheel torque is calculated to be 3100 Nm and peak power to be 135 kW with an overloading time duration of 20s, by means of drive cycle simulation. The continuous performance is estimated to be about 55 kW at 180 km/h. The performance requirements are presented in Figure 5.1, which also includes the operating points for WLTC drive cycle used for estimating the operating cost.

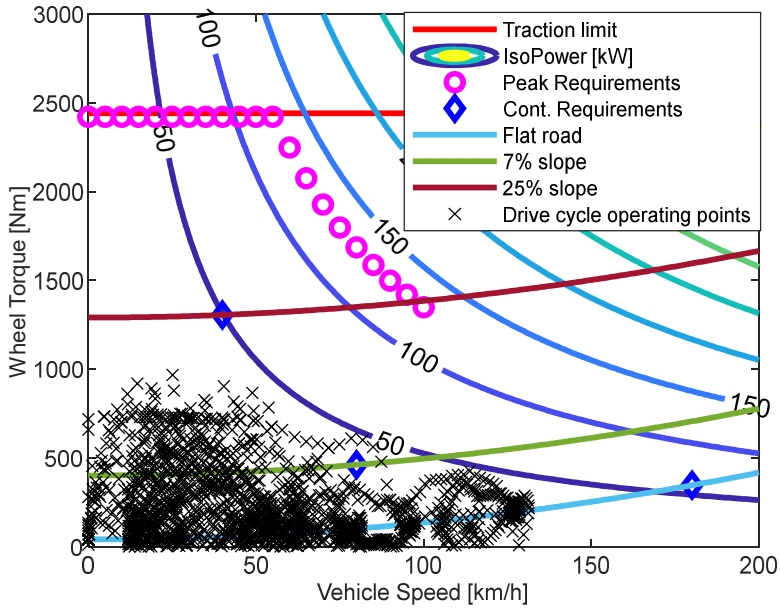


**Figure 5.1.** Vehicle requirement on wheel side

The objective of this optimization is to conduct a comparative analysis of various EM topologies from a system level. The objective function is the total cost of the powertrain cost and operating cost over one year, expressed as in (5.1).

$$f = (C_{EM} + C_{PEC} + C_{MT}) \cdot k_c + C_{Op} \cdot (1 - k_c) \quad (5.1)$$

The vehicle operating cost is estimated based on the energy consumption of the resulting powertrains, energy price (assumed electricity price: 0.5€/kWh) and the annual mileage (assumed value: 20,000km/year). The weighting factor plays a vital role in determining the relative importance of the two objectives in the function, balancing the powertrain cost and operating costs (system efficiency). In this study,  $k_c$  is assigned with a value of 0.5, which means the powertrain cost is depreciated over one year and is explained in results.

Subsequently, all EMs in the databases are evaluated. This evaluation seeks to identify the optimized EMs for each considered topology, facilitating a comparative analysis for all EM topologies, including cost competitiveness and overall system efficiency. For instance, with the same EM power rating, the PMASynRM benefits from the utilization of low-cost magnets, which in turn contributes to a reduction in the EM cost compared to the PMSM. However, the PMASynRM's lower power factor requires a larger, and consequently more costly PEC unit.

Moreover, selecting optimal EM designs for the comparative study serves to mitigate the impact of different EM structures on the research outcomes. For example, a well-designed PMASynRM may demonstrate comprehensive advantages over an unoptimized PMSM. By analyzing these aspects at the system level, the trade-offs in applying different EM topologies can be effectively highlighted.

In addition to the aforementioned data, other relevant settings and constraints are outlined in Table 5.2.

**TABLE 5.2 Extra Settings and constraints**

<b>Component</b>	<b>Settings/Constraints</b>	<b>Value</b>
<b>PEC</b>	DC-link voltage	800 (V)
	Semiconductor technology	SiC-MOSFET
	Switching frequency	10 kHz
<b>EM</b>	Winding type	hairpin
	Possible number of layers	4, 6, 8
	Maximum allowed winding temperature	180 (°C)
	Minimum overloading time	20 (s)
<b>MT</b>	Maximum gear ratio	19

In this study, the DC-link voltage is set to 800V, with SiC being the chosen semiconductor material due to its superior thermal and efficiency performance. For EM, the minimum overloading time ensures that the optimized EM are capable of sustaining peak performance for a duration longer than 20 seconds. The maximum gear ratio for the MT is constrained by the limits of the maximum gear ratio for each gear stage.

## 5.2. Results

### 5.3.1. Optimization results for all types of EMs

To have a better understanding of how  $k_c$  affects the optimization results, a comparison is done with two weighting factors:  $k_c$  equals 0.5 and 0.1, meaning that the powertrain cost is depreciated over one year and nine years. Figure 5.2 shows the optimization results with over 1000 single-V PMSMs under two weighting factors.

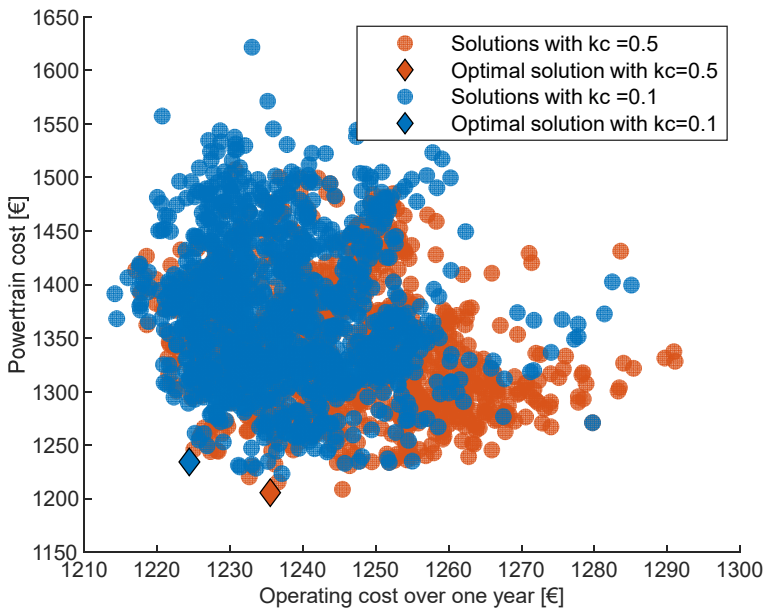


**Figure 5.2.** Designs with single-V PMSM under two weighting factors

Each circle in the graph represents an optimal powertrain solution corresponding to a specific 2D EM geometry. The results demonstrate that when  $k_c$  is set to 0.1, the optimizer favors solutions with more efficient powertrains, as the powertrain cost is depreciated over nine years. In contrast, when  $k_c$  is set to 0.5, the optimizer selects powertrain solutions with lower powertrain cost but higher operating cost. As the powertrain cost is directly linked to powertrain sizing, which is also a key performance indicator (KPI), a  $k_c$  value of 0.5 is chosen to reflect the impact of cost on overall performance.

The optimization outcomes for all machines are depicted in Figure 5.3.

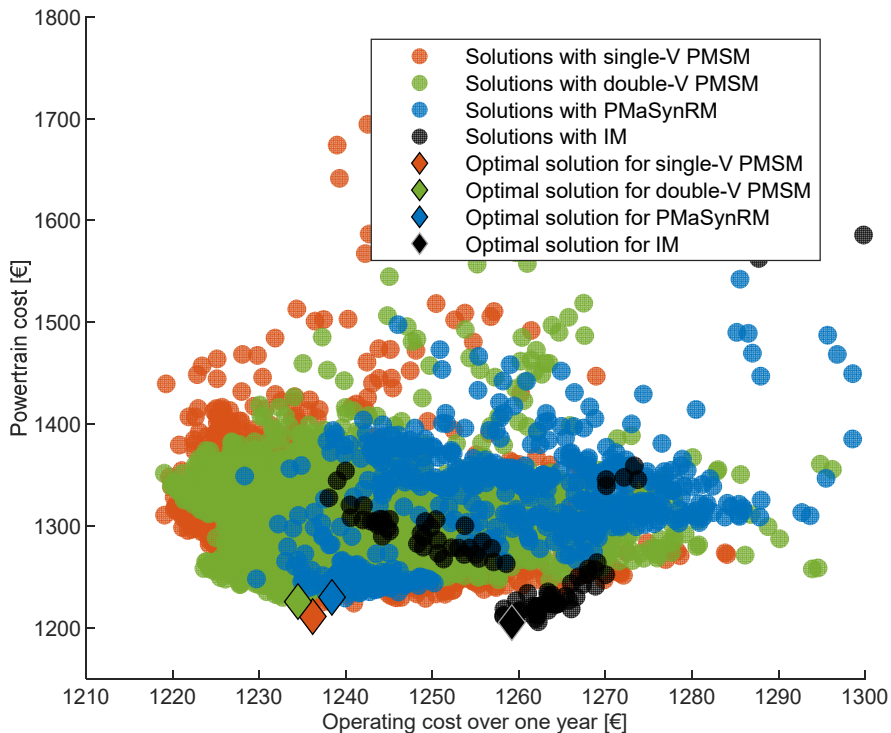


**Figure 5.3.** Optimal designs with all 2D geometries for each machine

In Figure 5.3, it can be seen that the feasible powertrain solutions with different EM topologies overlap with each other. For example, even if the PMSM is known for having better efficiency performance, it is observed that there are optimized IM-based powertrains outperforming plenty of PMSMs regarding system efficiency.

Nonetheless, it is evident that the PMSM designs tend to demonstrate better efficiency performance, and consequently, lower operating cost, in comparison to the other machine types. With the same torque level, the PMSynRM demands increased current to meet the torque requirement, leading to higher copper losses and diminished efficiency performance. Due to its lower torque and power density, larger PMSynRMs are needed to fulfill the requirements, offsetting the cost benefits brought by the cheaper magnets.

For IM, due to the extra losses generated from the rotor cage, it is less efficient compared with the PM machines. However, it has the advantage of having low drag losses under the

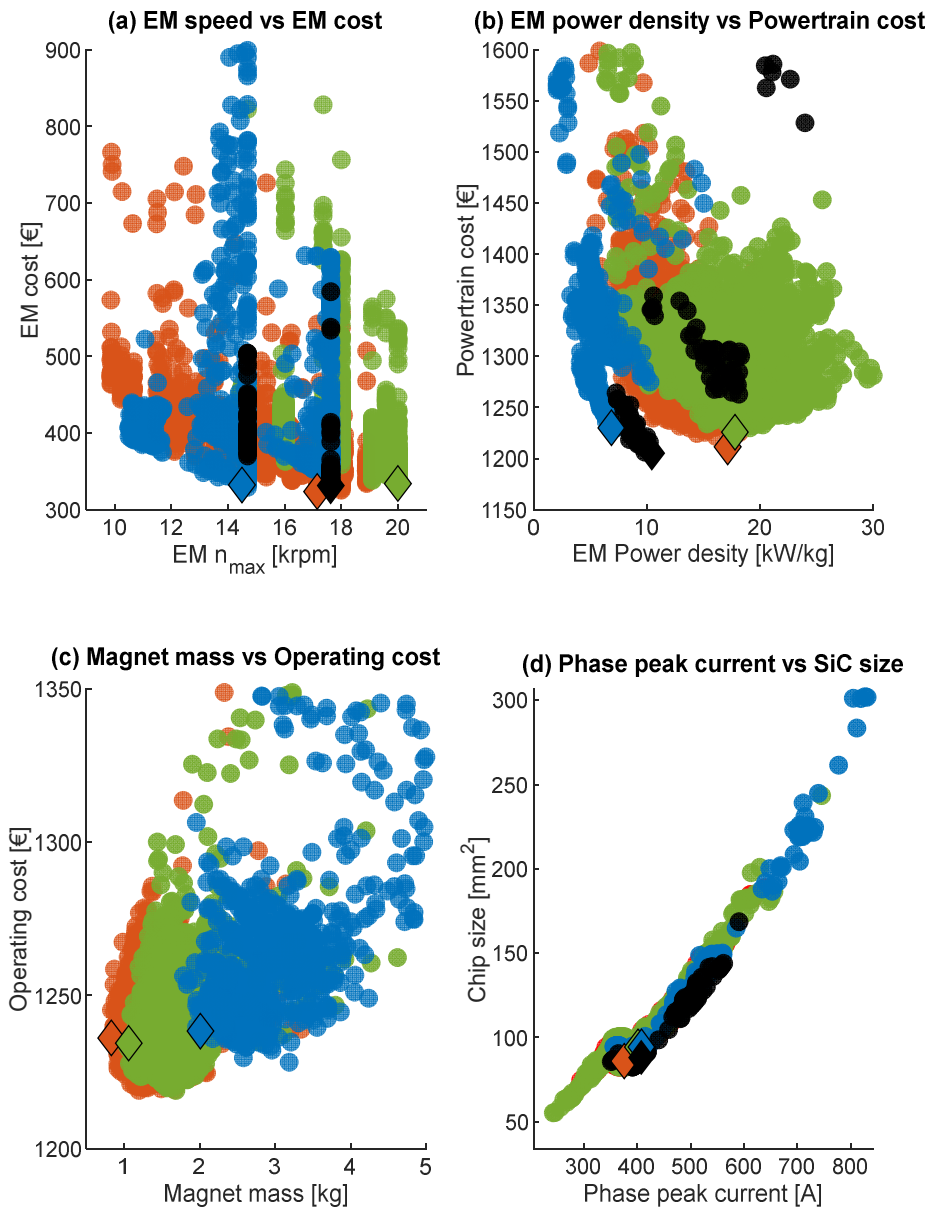
inactive state, making it potentially well-suited as secondary drive unit in dual-motor EV configurations.

Figure 5.4 offers a comprehensive analysis of how various component parameters influence performance across different EM designs.

An interesting observation from Figure 5.4 (a) is the impact of rotor topology on the maximum mechanical speed achievable by each EM, assuming uniform mechanical strength of the laminations. The analysis indicates a nuanced variation in maximum speed performance among the different rotor configurations. Specifically, the double-V PMSM, as depicted in Figure 2.2 (c), incorporates a broader rib for the air pocket at the bottom compared to its single-V counterpart. This structural enables a higher mechanical speed capability, which can be evaluated with the speed estimation equation in Chapter 2. However, this is not a general conclusion that double-V PMSM shares advantage over maximum mechanical speed, it is just led by the initial geometry settings for these two types of machines.

Figure 5.4 (a) illustrates a trend that as the maximum speed of the EMs increases, the EM cost shows a tendency to decrease. This highlights the industry's drive towards developing faster EMs as a means for achieving lower cost (smaller 3D size) and improving power density. It should be noted that the rib widths are predefined for all EM topologies. Modifications to rib width are found to influence the electromagnetic performance of EMs significantly. For example, employing a narrower rib and bridge or rib-less and bridge-less rotor structure can contribute to a reduction in leakage flux around the magnets, albeit at the cost of compromised mechanical strength of the rotor, which requires laminations with stronger mechanical strength or extra methods, such as carbon fiber sleeve, to ensure the rotor's mechanical robustness. This balance between structural design choices and their impacts on EM performance highlights the complexity of optimizing EM designs for enhanced efficiency and cost-effectiveness.

In Figure 5.4 (b), the relation between the EM power density and powertrain cost is explored. It becomes apparent that PMSMs generally exhibit higher power density compared to PMSynRMs and IMs. This superior power density is a significant factor contributing to the widespread popularity of PMSMs in the automotive industry. Furthermore, among the PMSMs, the figure shows that the double-V shape PMSMs demonstrate power density advantage over the single-V PMSMs. The higher power density



**Figure 5.4** Comparison for EM types with different component parameters. Single-V PMSM (red), double-V PMSM (green), PMaSynRM (blue), IM (black)

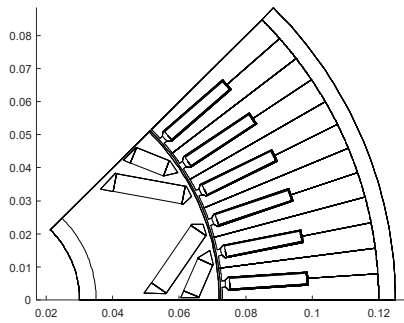
in double-V shape PMSMs is attributed to their ability to accommodate more magnets, as illustrated in Figure 5.4 (c), and achieve higher reluctance torque. It should be noted that the total EM mass only includes the weight of magnets, laminations, and windings. The other parts, such as housing, bearing, shaft and other accessory parts are not included.

Figure 5.4 (d) shifts the focus towards the correlation between the total chip area of the power module and the EM peak phase current. An obvious trend can be observed that the chip area is proportional to the peak phase current of the EM, which is the most challenging operating point for the inverter. However, certain solutions exhibit a relatively higher peak current, yet a smaller total chip area compared to those with less peak current. It is found that if the peak current is below a specific threshold, one single chip ( $A_{chip} < A_{chip,max}$ ) can handle the requirements (the maximum chip area for single chip is predefined in the PEC internal optimization iteration). However, as the current increases, larger chips are needed to maintain the junction temperature below the limitation. Then the chip area surpasses the predefined area limit, leading to additional chips introduced in the power module. The integration of multiple chips, arranged in parallel within the power module, enhances the heat dissipation [17], thereby reducing the junction temperature rise for each chip and thus smaller chips are allowed.

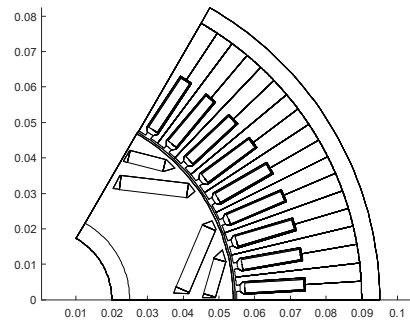
It is also noteworthy that, solutions employing PMSMs can exhibit lower phase current and, consequently, a reduced total chip area compared to those utilizing PMSynRMs and IMs, which is due to PMSMs' higher power factor. However, the optimal PMSM design, represented as red and green diamonds in Figure 5.4 (d), are not positioned among the solutions featuring lower current. Instead, they are situated at a higher current level, thus driving the peak power of the two optimized PMSMs to exceed the necessary requirements.

To better explain this result, a powertrain solution employing a double-V PMSM, distinguished by its lowest phase current, has been selected for comparison against the optimal solution, which achieves the minimum total cost.

Figure 5.5 shows the 2D geometries for the optimized EMs with minimum phase current and the minimum total cost. Table 5.3 illustrates the detailed information of the two powertrains.



(a) Double-V PMSM with minimum peak current



(b) Optimal Double-V PMSM with minimum total cost

**Figure 5.5** 2D geometries of the two selected double-V PMSM

**TABLE 5.3** Comparison for two selected powertrains

Parameter	Double-V PMSM with min. phase current	Optimal double-V PMSM
Active length (mm)	72	104
Max speed (rpm)	15910	20000
Peak power (kW)	154	202
Peak torque (Nm)	271	198
Phase peak current (A)	260	401
EM cost (€)	388	334
PEC cost (€)	616	636
MT cost (€)	291	255
Operating cost (€)	1260	1234
Total cost (€)	2555	2459

The PMSM with min. phase current exhibits a significantly lower peak power in comparison to the optimal PMSM, showing a phase current and therefore inverter sizing and EM power, closer to the actual requirements of the studied application, which can be seen in Figure 5.6.



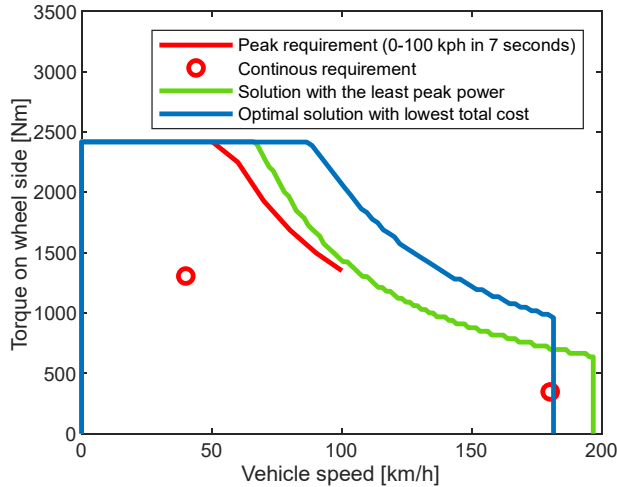


**Figure 5.6** Torque envelope of two selected PMSMs

The optimal PMSM demonstrates a higher maximum speed due to its smaller rotor, resulting in a reduced torque requirement and thus 3D dimension, subsequently a lower EM cost. Moreover, the transmission also benefits from the reduced torque input from EM, contributing to a MT cost reduction. Notably, the optimal PMSM exhibits better efficiency performance, presenting the most cost-effective solution across all evaluated powertrain solutions.

Variations in the material costs for both the EM and the PEC have a significant impact their costs, which in turn, influences the outcomes of the optimization process. For example, an increase in the price of SiC chips, leading to an escalation in PEC costs relative to EM costs, drives the optimizer to prefer solutions characterized with lower current.

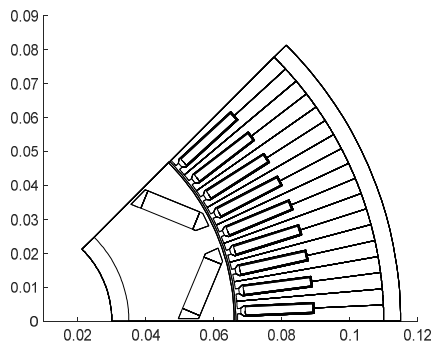
What's more, the significance of the objective function in this context cannot be overlooked. The selection of specific optimization objectives fundamentally shapes the optimization direction and determines results of the optimization process.

As in this thesis, the sum of powertrain cost and EV operating cost is considered as the optimization target. The optimal powertrain solutions for each EM topology have been identified and are denoted by diamond symbols in Figure 5.4. The optimal 2D EM geometries for each optimized solution are shown in Figure 5.8 and the detailed information of the optimized solution is provided in Table 5.4.

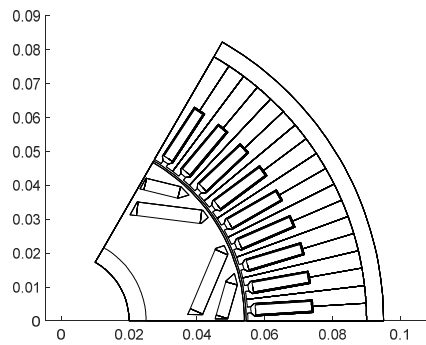
**Table 5.4. Optimal EM design comparison**

Parameter	Single-V PMSM	Double-V PMSM	PMSynRM	IM
Active length (mm)	75.6	104	120.4	155.6
Max speed (rpm)	17150	20000	14490	17630
Max torque (Nm)	233	198	278	225
Base speed (rpm)	7069	9711	5836	8995
Peak power (kW)	172	202	170	212
Phase peak current (A)	375	401	398	407
EM mass	8.81	8.92	21.94	17.59
EM cost (€)	323	334	332	331
PEC cost (€)	626	636	637	628
MT cost (€)	262	255	261	245
Gear ratio	10.35	12.14	8.56	10.82

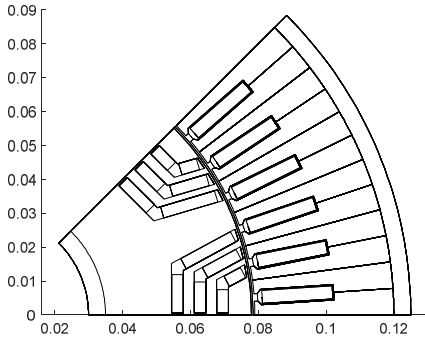
It reveals that the optimal EM designs demonstrate distinct 2D geometries and performance characteristics. The peak power of the four optimized solutions all exceeds the actual vehicle requirements, a decision aimed at achieving a more favorable overall cost.



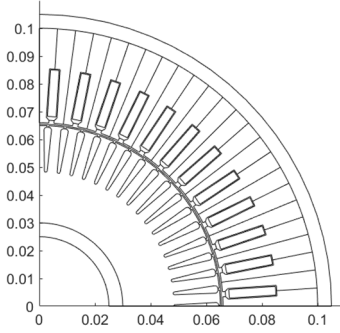
(a) Optimal geometry of single-V PMSM



(b) Optimal geometry of double-V PMSM



(c) Optimal geometry of PMaSynRM



(d) Optimal geometry of IM

**Figure 5.8** Optimal geometry of the optimized EM

The inherent high-power density of PMSM enables the optimizer to select comparatively smaller-sized PMSMs. The difference in EM rotational speeds, especially when a single-speed transmission is utilized, significantly influences the performance of the EMs, as shown in Figure 5.9. The optimized PMaSynRM, characterized by a lower maximum rotational speed, requires higher torque to meet the vehicle's top speed and acceleration demands at the same time.

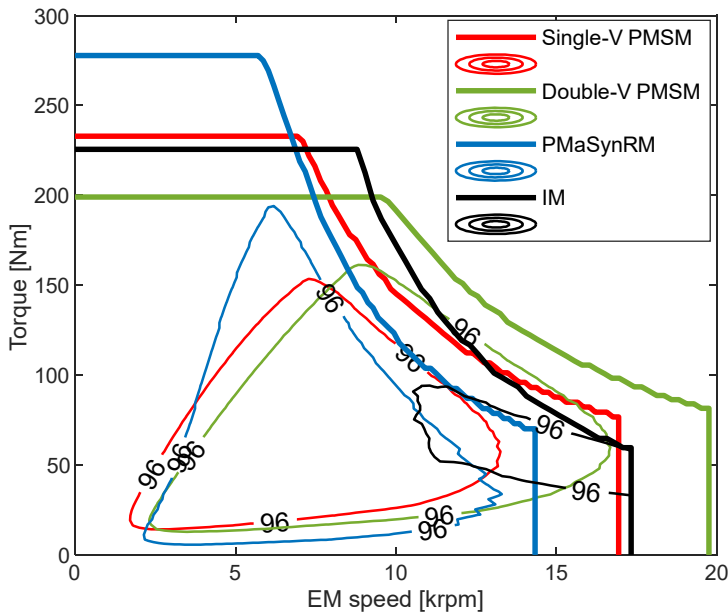


**Figure 5.9.** Performance comparison among three optimized machines

In terms of effective mass, the PMSMs present the lowest total mass, with 8.81 kg for single-V PMSM and 8.92 kg for double-V PMSM, respectively, showing outstanding advantages over the other two EMs. Figure 5.10 presents a detailed material utilization for each optimized EM.

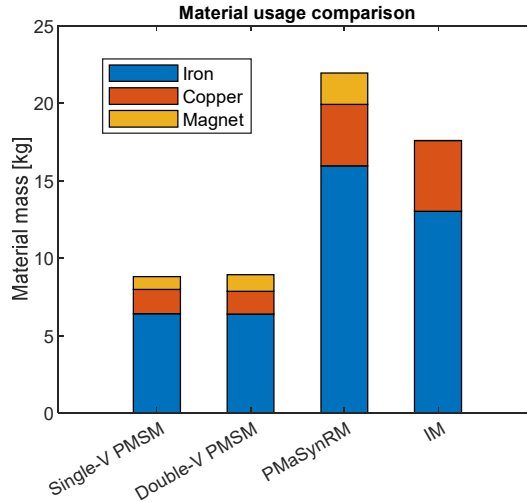


**Figure 5.10** The material usage comparison

Given the significant cost associated with rare-earth permanent magnets [97], the total cost of the two PMSMs are nearly equivalent to that of the larger PMaSynRM. The structure of the IM results in the absence of permanent magnets, replaced instead by the copper rotor cage, leading to more copper usage.

In terms of the EM efficiency, the IM is characterized by higher total copper losses and lower iron losses relative to the PMSM and PMaSynRM. This results in a narrower high-efficiency region for the IM, and high efficiency area shifting towards higher speed region. Most operational points of the drive cycle fall outside the IM's high-efficiency zone, leading to a greater energy consumption throughout a cycle, as illustrated in Figure 5.11.

Figure 5.11 also indicates that the PMaSynRM based powertrain exhibits the lowest EM cycle losses. However, as depicted in Figure 5.3, numerous PMSMs outperform the PMaSynRM in terms of efficiency, though this comes at the cost of increased powertrain expenses. As a result, the optimization algorithm selects solutions that sacrifice EM efficiency to minimize powertrain costs, thereby identifying the optimal trade-offs under the selected objective function.

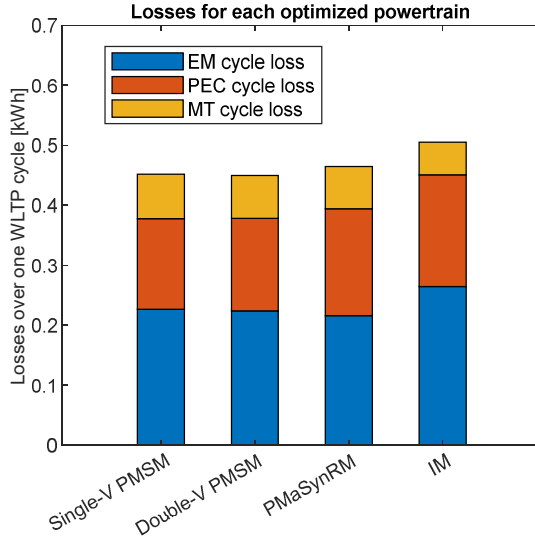
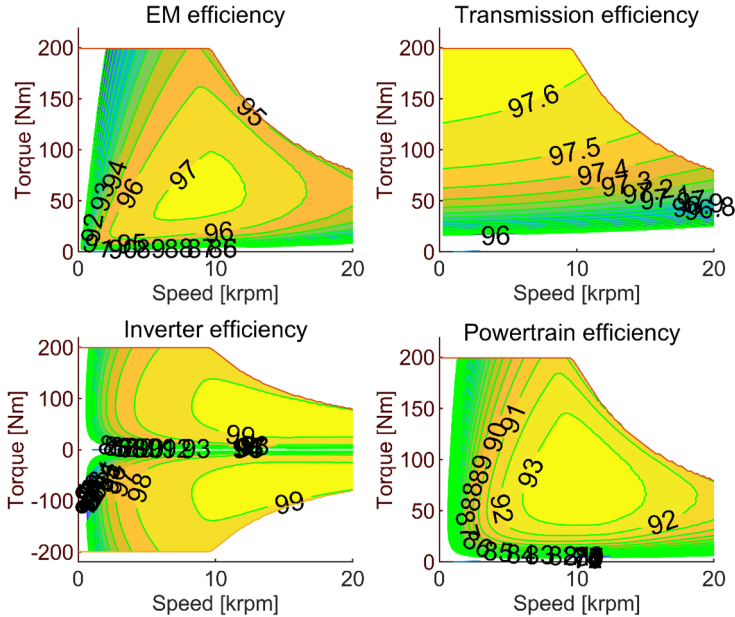


**Figure 5.11** Losses for each optimized powertrain

Table 5.5 takes the optimal double-V PMSM based powertrain as an example and gives a more detailed description of powertrain configuration with the efficiency maps of each component.

**TABLE 5.5 Optimal powertrain design with double-V PMSM**

EM design		Transmission design	
Active length ( <i>mm</i> )	104	Gear ratio	12.14
Num. of turns	12	Num. of teeth for gear stage 1	31/118
Num. of winding layers	8	Num. of teeth for gear stage 2	37/118
Num. of parallel path	2	PEC design	
Peak current density ( $A/mm^2$ )	25.5	Num. of chips	2
		Single chip area ( $mm^2$ )	47.2
Efficiency map			



### 5.3.2. Demagnetization analysis for PMSynRM

As introduced in Chapter 2, PMSynRMs are easy to be demagnetized when using magnets with lower coercivity. This phenomenon typically occurs when a significant negative  $d$ -axis current is applied, which can be the case in the field weakening region or during a fault condition.

The structure of the optimal PMSynRM from the optimization is shown in Figure 5.8 in which the demagnetization is not considered. However, when the demagnetization evaluation during the normal operation is included, it is found that there are no feasible solutions which can fulfill the demagnetization requirements. The flux density distribution of the optimal PMSynRM shows that the magnets embedded in the sides of the flux barrier are easily demagnetized, leading to all the solutions exceeding the EM dimension constraints.

It is known that from Figure 2.16 that the magnets situated in the first layer (the layer closer to the rotor surface) and the sides of the flux barrier are particularly susceptible to demagnetization. This requires a reconsideration of the PMSynRM design to ensure its reliability under various operating conditions. Consequently, several geometry improvements are made to prevent irreversible demagnetization. A new generated

PMASynRM database is introduced for the demagnetization analysis and one example of the new geometry in the database is shown in in Figure 5.12.

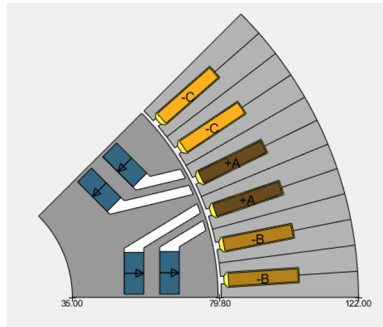


Figure 5.12 PMASynRM model

It can be seen that the magnets in the sides of the flux barrier are removed and the magnets in the middle of the flux barriers are also placed further from the rotor surface. Furthermore, thicker magnets are used within the generation of the new database.

An example of the flux density distribution for the selected PMASynRM model is illustrated in Figure 5.13.

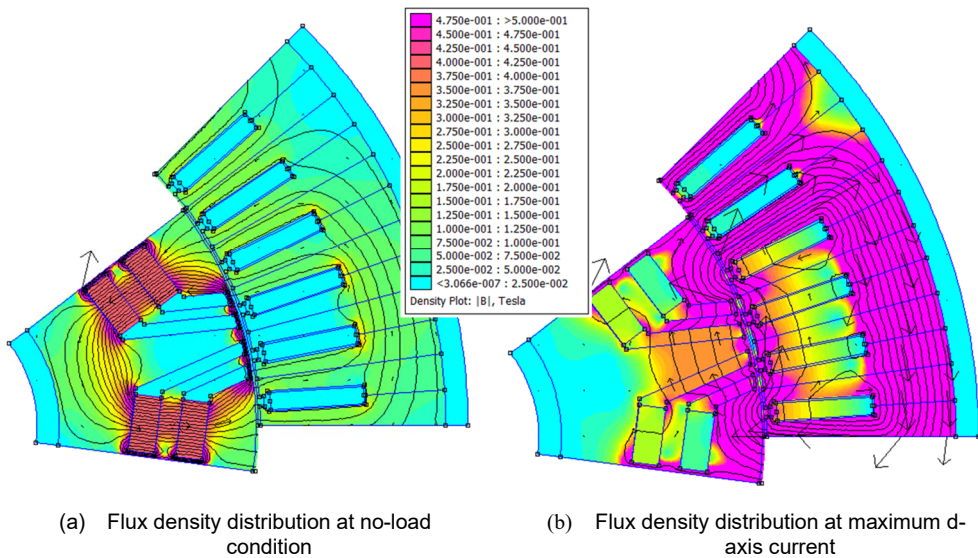
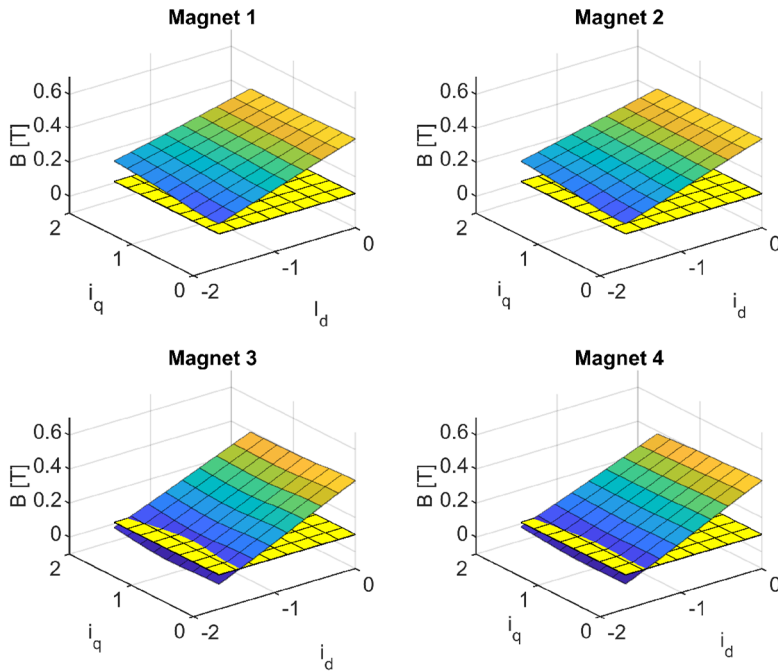


Figure 5.13 Flux density distribution under no-load and  $i_d = -2 p.u.$  condition

The flux density data along the magnetization direction is collected for all magnets at the selected positions, as shown in Figure 5.14.



**Figure 5.14** Flux density in magnetization direction for all magnets at selected position (20 °C).

With the new generated PMSynRM database, the powertrain optimization is performed with introducing the maximum MMF allowed as one constraint. The optimization results with the new database are shown in Figure 5.15.

It can be seen that the EM designs considering the demagnetization have worse efficiency and increased EM cost. This is due to the fact that the total MMF is limited, which can be seen in Figure 5.15 (b), to reduce the risk of irreversible demagnetization for all magnets. However, to satisfy the vehicle torque requirements, the dimension of PMSynRMs in axial direction need to be increased to output the required torque, leading to a higher machine cost.

To evaluate how the demagnetization affects the PMSynRM design, the optimal PMSynRM geometries for the optimal solutions are shown in Table 5.6.

Although PMSynRMs in previous database exhibited comparative performance with PMSMs, the advent of demagnetization concerns finds the rotor topologies unsuitable.



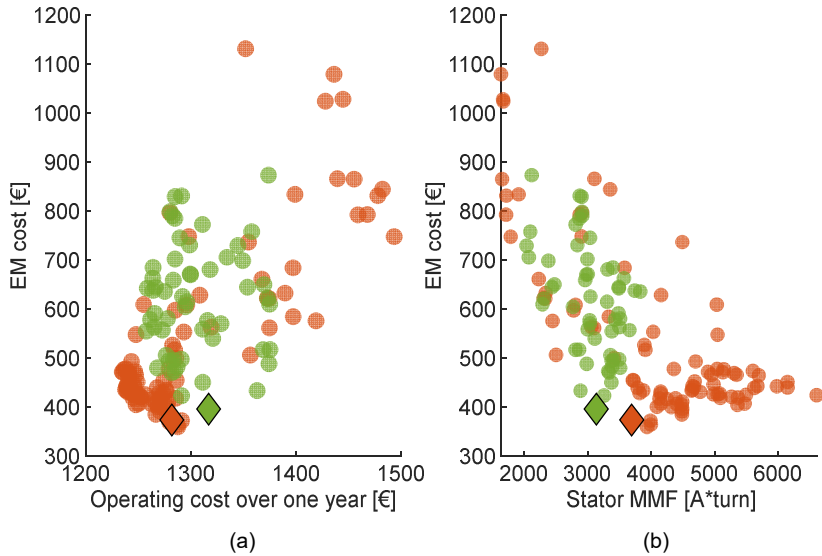
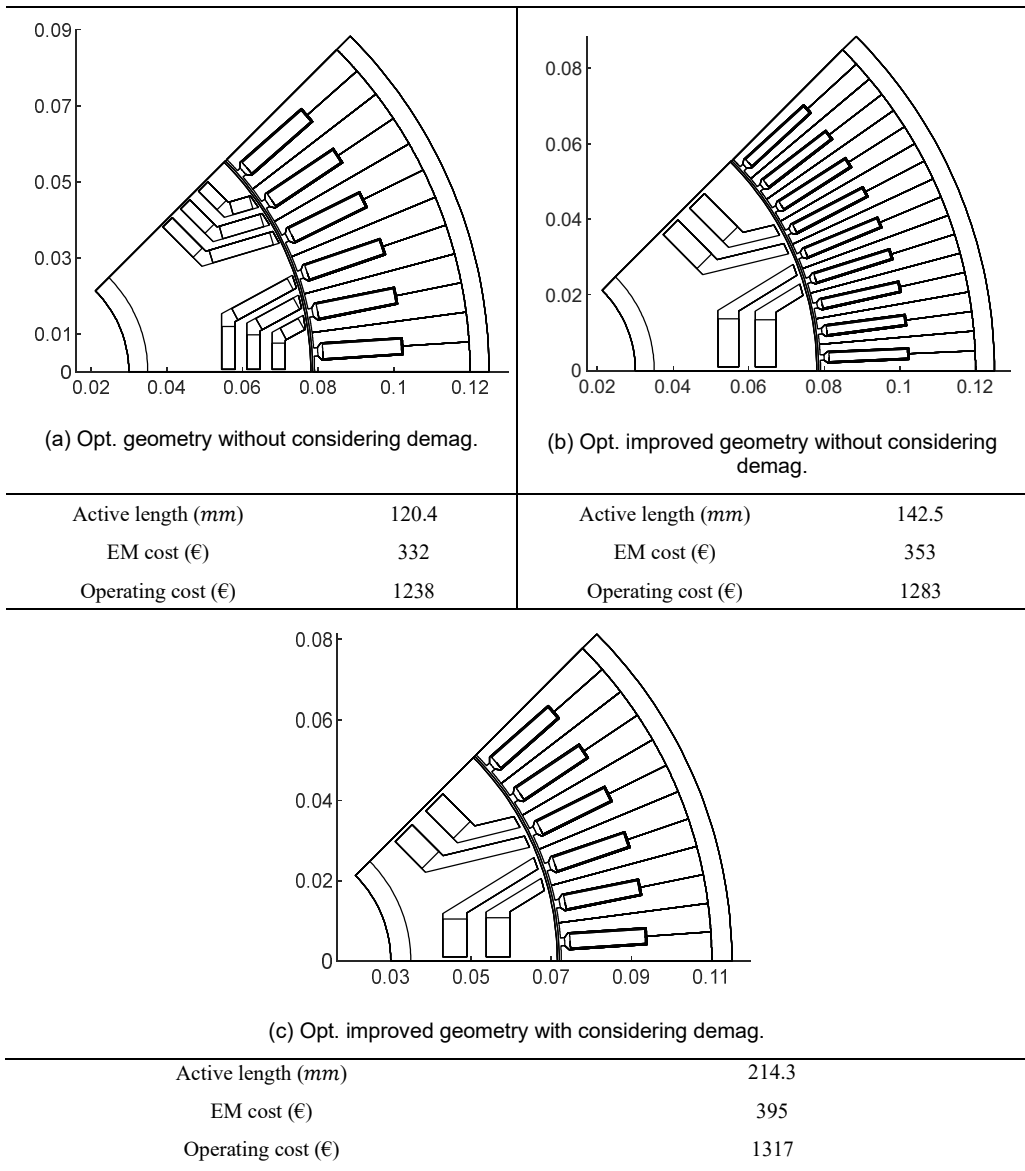


**Figure 5.15** Optimization results with the new EM database.  
 Red/Green circles and diamonds: PMA SynRM solutions without / with considering the demagnetization.

This stems from the fact that even under low stator MMF conditions, all machines in the previous database fail to prevent demagnetization.

In response to this challenge, an improved rotor design has been developed, enabling the new PMA SynRMs to withstand the demagnetization MMF. However, this enhancement comes at a cost: fewer magnets are embedded in the flux barrier, resulting in reduced torque and a decline in powertrain efficiency when performing powertrain optimization without considering demagnetization. What's more, while the demagnetization limitation is introduced to ensure the system reliability, the optimal PMA SynRM must lower its stator MMF, thereby compromising overall system performance.

**TABLE 5.6** Optimal PMaSynRM geometries under three scenarios



It's worth noting that the demagnetization analysis in this thesis primarily focuses on the maximum current condition, with the current phase angle set at 90 degrees. However, the risk of irreversible demagnetization could escalate further in the event of a short circuit [98] [99][100]. Transient currents associated with such an event can be over twice the maximum current rating, intensifying the risk of demagnetization.

### 5.3. Conclusions

With all the discussions about the advantages and disadvantages of all types of EM, it can be concluded that the optimal designs identified by the optimization process should not be taken as the final solution. There are several powertrain alternatives that offer performance closely aligned with those of the optimal designs. Moreover, the outcomes of the optimization are influenced by a variety of factors, including but not limited to, the inputs fed into the optimization algorithm, the objective function itself and demagnetization analysis.

Given these considerations, a more refined optimization approach can be beneficial. This could involve narrowing the scope of the EM database to focus on a subset of EMs that are most relevant to the specific application requirements. Such a targeted approach can help in filtering out less relevant options and concentrating the optimization efforts on the most promising candidates.

# Chapter 6 Platform-based System Optimization

This chapter presents a method to optimize an electric powertrain platform, capable of addressing the needs of a wide range of vehicle types while taking advantage of economies of scale and reducing time to market.

There are many efforts focusing on the electric powertrain optimization. In [63] and [101], they employ holistic approaches to investigate the optimal design of electric powertrains, considering multiple objectives. In [102], powertrain optimization methods are applied to demonstrate how cross-platform optimization can help the original equipment manufacturers (OEMs) create product strategies that are cost effective across a variety of vehicle classes. In [103], a design method able to consider multiple electric powertrain design problems and reduce the system costs by utilizing commonalities between the single designs is proposed. In [104], a concurrent optimization framework to design shared modular powertrain components for a family of battery electric vehicles is presented to reduce the powertrain cost due to the higher volumes of the same component.

The implications of platform-based powertrain optimization extend beyond the automotive sector, potentially benefiting the environment and society. By reducing the development time and cost of powertrains, automakers can bring electric vehicles to market more quickly and at more affordable prices, making them more accessible to a broader population.

In this chapter, when estimating the cost for the EM, the R&D cost is introduced to examine its influence on the broader strategy of platform-based powertrain optimization for EVs. Finally, this case study explores the benefits and constraints of platform-based powertrain optimization by identifying the optimal powertrain designs with different commonalities with EMs across three distinct vehicle classes.

## 6.1. Optimization process

The process of platform-based powertrain optimization is depicted in Figure 6.1. The optimization process for single EV powertrain is the same as the process explained in Chapter 5. The optimizer strives to find the optimal combination of scaling factors that minimizes the objective function, denoted as  $f_1$ .

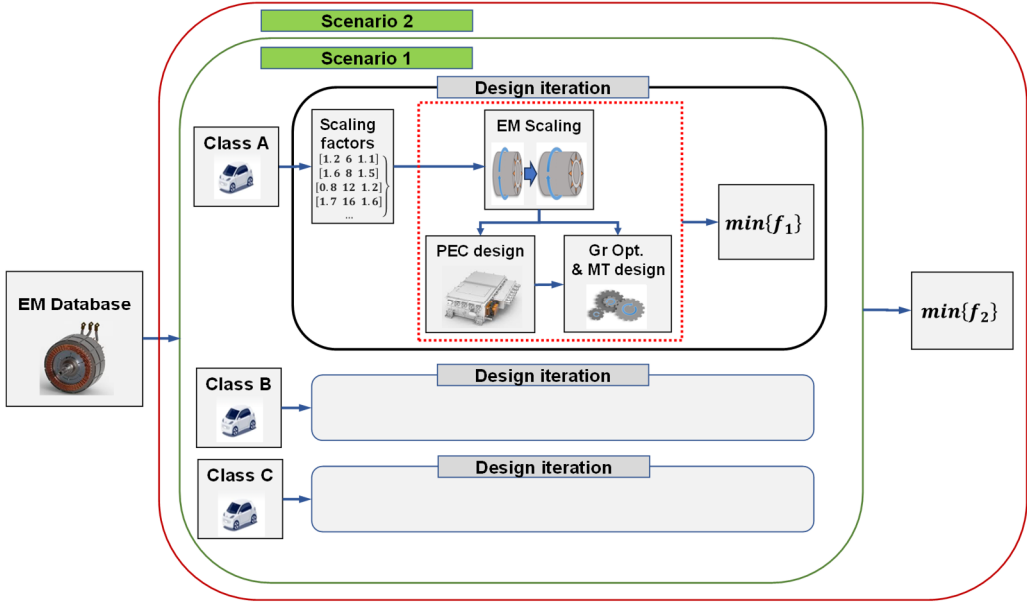


Figure 6.1 Platform-based powertrain optimization methodology

As it can be seen in Figure 6.1, the inner most loop contains optimizations for several distinct EV classes. The optimization targets each EV class individually, aiming to achieve the optimized powertrain configuration for each. This inner loop optimization is then defined as Scenario 1. The objective function of Scenario 1 is expressed in (6.1),

$$\text{Optimization goal of S1: } \min ( f_1 (EM_{ind}, x)) \quad (6.1)$$

Following the evaluation of all EMs in the database for all vehicle classes, the 2D EM geometry that provides the lowest objective function,  $f_2$ , is selected as the best EM solution for the platform, which is defined as Scenario 2. The goal of this outermost loop of the optimization is formulated in (6.2), aiming to find the optimal platform-based powertrain design.

**Optimization goal of S2:**  $\min (f_2(EM_{ind}))$

$$f_2(EM_{ind}) = \sum_{i=1}^N [V_i \cdot \min\{f_1(EM_{ind}, x_i)\}] \quad (6.2)$$

The number of vehicle classes is depicted by  $N$ . For each class,  $V_i$  represents the yearly production volumes. However, as the optimal EM 2D geometry is identical for all classes with scenario 2, the production volumes for many of the EM manufacturing steps are increased. So, when estimating the EM cost with scenario 2, a crucial adjustment should be made to reflect the benefits of economies of scale: the production volume for EM is  $\sum_{i=1}^N V_i$ .

Consequently, a unique optimization run for scenario 2 becomes necessary. This run is tailored to account for the increased production volumes and their impact on the EM cost.

## 6.2. Vehicle specifications for EV platform

The first step of platform-based powertrain optimization involves the identification of the EV classes and representative EVs. This is crucial for acquiring a better understanding of the requirements of each EV class.

Representative vehicles within these classes are then selected as benchmarks. In [105], two distinct EV segments are examined, with the peak power of the EMs and maximum wheel torque being determined from a large number of EV applications to perform the platform-based optimization. In this chapter, specifications of several single-motor-driven EV applications are collected and the weight, acceleration time and maximum speed of them are illustrated in Figure 6.2, offering a clear overview of the varying specifications across the selected EV applications.

Based on the work in [105] and the collected EV specifications, this study formulates three classes of single-motor-driven EVs to perform an in-depth investigation into platform-based powertrain optimization. The specifications for the three EV classes are shown in Table 6.1.

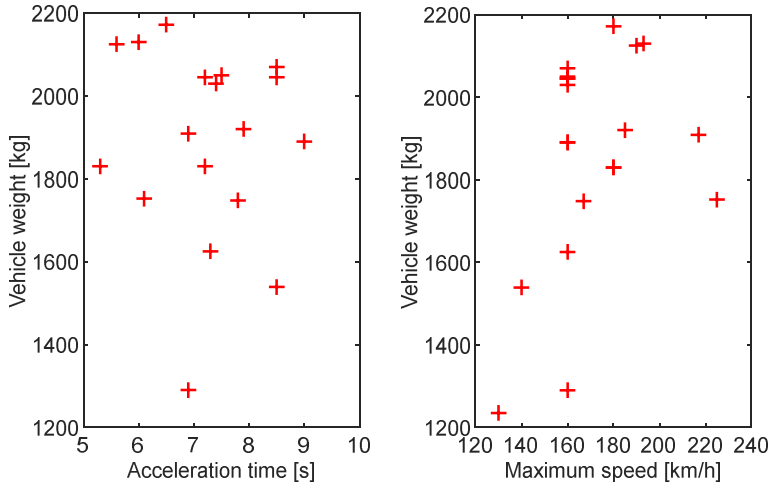
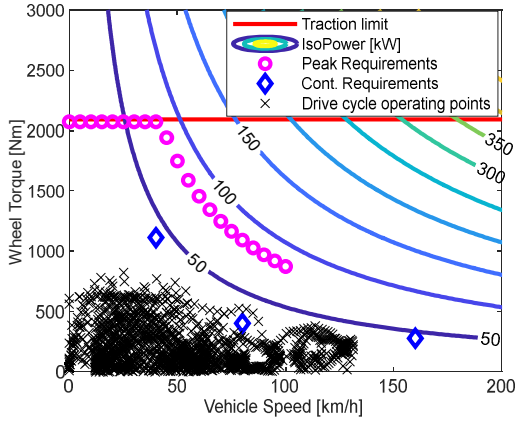


**Figure 6.2.** Key specifications for single-motor-driven EV applications

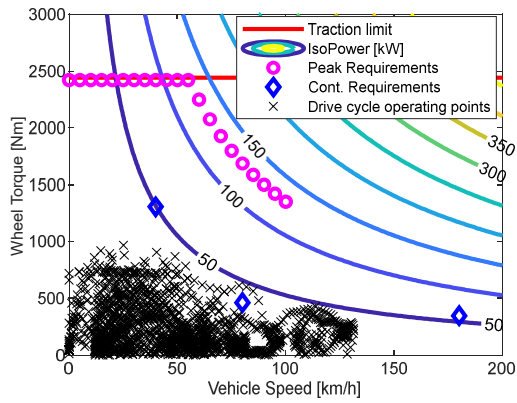
**TABLE 6.1 EV specifications for three classes**

Parameter	Class A	Class B	Class C
Weight ( <i>kg</i> )	1450	1650	1850
Front area ( $m^2$ )	2.11	2.20	2.36
Drag Coefficient	0.32	0.31	0.267
Rolling resistance	0.008	0.008	0.008
Max speed ( <i>km/h</i> )	160	180	225
Acceleration 0-100kph (s)	9	7.5	6.5
Gradeability	25% @40 kph 7% @ 80 kph		

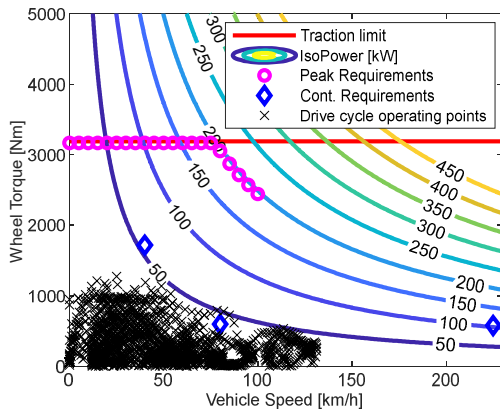
Based on the vehicle specifications listed in Table 6.1 and employing the WLTP as the drive cycle, this study calculates the requirements for each EV class at the wheel side and identifies the operating points of the drive cycle, which are depicted in Figure 6.3.



(a) EV Class A



(b) EV Class B



(c) EV Class C

**Figure 6.3.** Vehicle requirements for EV Class A, B and C



### 6.3. Objective function

In the automotive industry, the research and development (R&D) expenses for powertrain systems constitute a significant portion of the overall investment, directly impacting the final pricing of EVs. This section introduces and quantifies the R&D costs associated with EMs to explore the influence of these costs on the strategy of platform-based powertrain design for EVs, particularly analyzing the potential cost reductions in powertrain systems achieved by distributing the investments in EM development across multiple EV classes.

For a single EM product, the R&D cost is estimated at 10 million euros, including the personnel cost, expenses for equipment and facilities, cost incurred during prototyping and testing, etc. In the platform-based powertrain design process, where all EVs from the given platform share the same EM topology, only one EV class bears the full R&D cost. For the rest of the EV classes, certain cost segments are divided, leading to an estimated R&D cost of 3 million euros for each.

The objective function for each presented EV application in Scenario 1, denoted as  $f_1(x)$ , is same as the objective function defined in Chapter 5 and expressed as follows in (6.3):

$$f_1 = (C_{EM} + C_{PEC} + C_{MT}) \cdot k_c + C_{Op} \cdot (1 - k_c) \quad (6.3)$$

It should be noted that the EM cost in this study includes material cost ( $C_{EM\_material}$ ), manufacturing cost ( $C_{EM\_manufacturing}$ ) and the R&D cost ( $C_{EM\_RD}$ ) amortized over the corresponding production volume ( $V_i$ ), as expressed in (6.4) and (6.5):

$$C_{EM} = C_{EM\_material} + C_{EM\_manufacturing} + C_{EM\_RD} \quad (6.4)$$

$$C_{EM\_RD} = \frac{C_{RD\_tot}}{V_i} \quad (6.5)$$

The production volume and R&D cost for all EM products of corresponding EV classes under two scenarios are listed below in Table 6.2.

**TABLE 6.2 EV specifications for three classes**

		EM for Class A	EM for Class B	EM for Class C
S 1	Volume	100 k	100 k	100 k
	R&D cost (€)	10 M	10 M	10 M
S 2	Volume	300 k	300 k	300 k
	R&D cost (€)	10 M	3 M	3 M

## 6.4. Results

This study only picks the database of double-V PMSM as input. The full optimization process involves optimization for each EV class (scenario 1) and platform-based optimization for three different classes of EVs (scenario 2), taking approximately one week, showing the complexity and computational intensity of the task.

In order to facilitate an in-depth analysis and a better understanding of the optimization process, the Class B application under Scenario 1 is selected as an example.

The objective function for Scenario 1 allows for exploring different weightings between the two objectives: powertrain cost and operating cost (system efficiency). Figure 6.4 illustrates the optimization results for the Class B EV, where two different weighting factors were applied to the objective function.

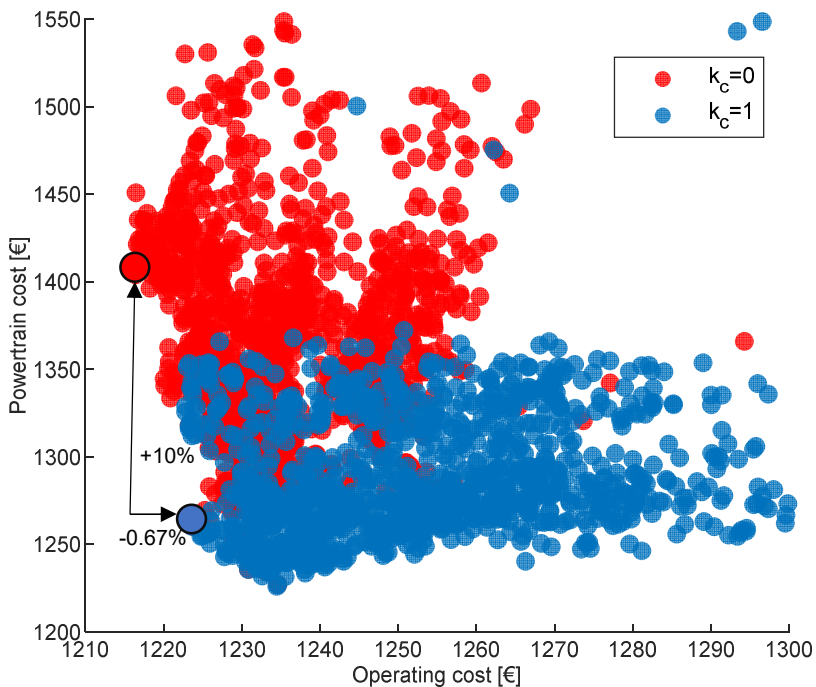


**Figure 6.4** Powertrain designs with different weighting factors for Class B

Each circle depicted on the graph represents the optimal powertrain solution with a specific 2D EM geometry. The results clearly demonstrate that prioritization of powertrain cost ( $k_c = 1$ ) leads the optimizer to favor minimization of the powertrain cost, at the expense

of system efficiency. Conversely, setting the weighting factor  $k_c$  to 0 results in the selection of powertrain solutions that exhibit superior system efficiency performance while more costly. Notably, the most efficient solution, achieved when the weighting factor  $k_c$  is set to 0, demonstrates a nearly 0.67% reduction of the operational cost compared to the solution obtained with a weighting factor of 1, at the cost of a 10% increase in overall system cost.

To have a comprehensive evaluation for the powertrain, the weighting factors for powertrain cost and operating cost are set to 0.5 for each, meaning that the powertrain cost is depreciated over one year.

The optimization process, as previously outlined, is conducted twice for scenario 1, each time considering different EM production volumes. The optimal solutions (red and blue stars) lay on the pareto front of each EV class under scenario 1 but different EM production volumes, as shown in Figure 6.5. The EM cost will benefit from the larger economies of scale. However, the cost reduction of the EM is not significant despite the increased economies of scale. This can be seen in Figure 2.23, the EM cost benefit achieved by increasing the production volume from 100 k to 300 k is limited. The solutions with blue circles in Figure 6.5 are evaluated with the EM production volume of 300 k units per year considering the R&D reduction benefits, which has a significant impact on the EM cost even at a high volume. It's worth noting that if each EV class takes their own optimized powertrain, the EM cannot benefit from reduced R&D cost, meaning that the optimal solutions marked with blue diamonds do not exist but are included as references.

The platform-based powertrain optimization results are illustrated in Figure 6.6 by searching for the lowest objective function,  $f_2$ , for the entire platform. The operating and powertrain cost are average costs for each EV class. In this scenario, as the powertrain solution is designed and optimized for the platform, it is inevitable that the system efficiency or the powertrain cost is compromised, leading to higher operating costs or powertrain cost compared with the reference solutions from scenario 1, which can be seen in Figure 6.5.

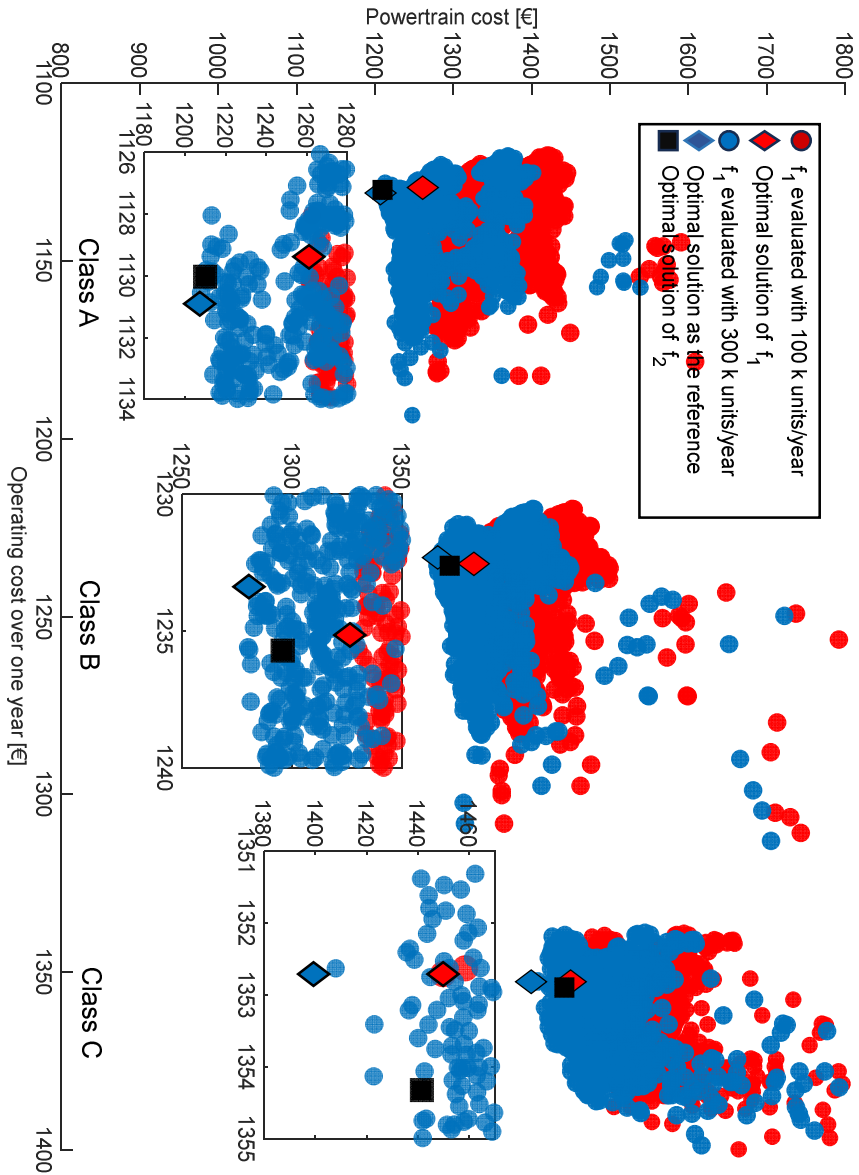
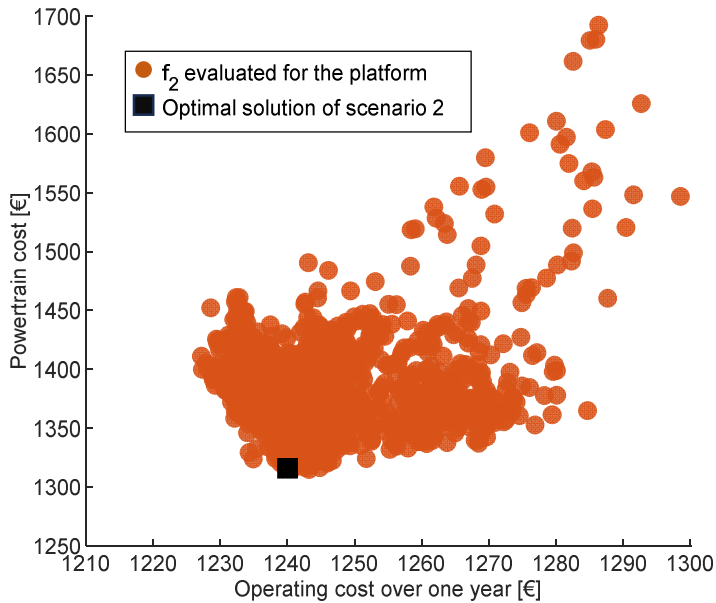


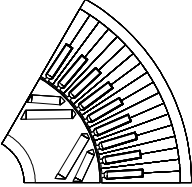
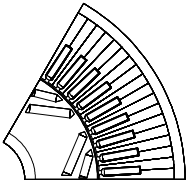
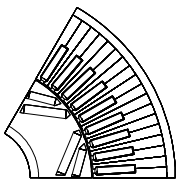
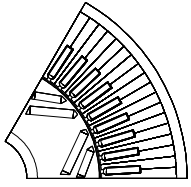
Figure 6.5. Optimization results for all vehicle classes with different production volumes under scenario 1.



**Figure 6.6.** Optimization results for all vehicle classes under scenario 2

Table 6.3 demonstrates the optimal EM 2D geometries for each class with two scenarios. With scenario 1, each EV class shares their own optimized EM topologies and active length. For scenario 2, all EV classes share the same EM topology but different active lengths to satisfy corresponding EV requirements.

**Table 6.3 EM geometries with two scenarios**

Scenario 1			Scenario 2
<i>Class A</i>	<i>Class B</i>	<i>Class C</i>	<i>Class A / B / C</i>
			
Ø90 × 81mm	Ø90 × 104mm	Ø110 × 85mm	Ø90 × 81/109/155mm

As previously noted, the reference optimal solutions primarily demonstrate the impact of R&D costs on powertrain expenses. When comparing the optimal solutions in two

different scenarios – represented by red diamonds (Scenario 1) and black squares (Scenario 2) – it becomes evident that Scenario 2, which involves sharing the same EM topology, offers a significant cost advantage over Scenario 1. However, this cost benefit comes with a compromise in powertrain efficiency for some applications. For Class A, while the operating cost, in terms of powertrain efficiency, sees a marginal increase of 0.1%, there is a significant reduction in powertrain costs of 4.1%.



# Chapter 7 4WD optimization

As previously established, EMs have significantly higher efficiency than ICEs, and can be designed to have a torque-speed profile that allows them to use single speed transmission. This is the dominant solution in passenger vehicles. However, this limits the system flexibility to adapt to conflicting requirements. High accelerations and curb climbing requirements demand high wheel torques and top speed requirements result into high wheel speeds. From a powertrain design perspective, these requirements need to be balanced through the optimization of the EM, inverter and transmission, as outlined in previous chapters.

For single-motor-driven EV, the EM can maintain high efficiency under most conditions. The peak efficiency can be over 95% but differs with different EM topologies, as discussed in Chapter 5. However, their efficiency can drop by 10-20% in situations of low-speed heavy load or high-speed light load compared to their high-efficiency area. Dual-motor 4WD configuration can expand the system's high-efficiency range through various powertrain combinations, thereby enhancing the system efficiency if equal vehicle performance is assumed. Alternatively, if 4WD is used to improve system performance, as commonly done in today's EV market, a clever optimization of the primary and secondary drive can mitigate the efficiency impact derived from having two electric powertrains when compared with a single driven axle. For example, an IM can be introduced as the secondary drive for 4WD EV, taking advantage of its attributes of higher efficiency at low torque and high-speed region and lower no-load losses, while PMSM as the main drive unit.

The exploration on this subject attracts a lot of attention from academia and industry. Research in [106] explored a 4WD system incorporating two identical IMs, employing numerical EM loss models. Study in [108] concludes that evenly distributing torque between two identical PMSMs has better efficiency performance. In [107]-[113], EMs of differing power ratings and various power distribution control strategies for 4WD system are analyzed, demonstrating enhanced efficiency in comparison to powertrains driven by a single EM.

This Chapter investigates the 4WD system optimization, including several cases with different system configurations, aiming to identify the optimal power rating for EMs on each axle and optimal torque distribution strategy for a given 4WD EV application. This



study tries to answer what would be a good way to compare the 4WD systems regarding the trade-off between system cost and energy consumption.

## 7.1. Vehicle configuration

As shown in Table 7.1, the selected EV applications offered in the market with two motors share outstanding dynamic performance, with acceleration time varying from 4.4s to 3.6s.

**Table 7.1 Examples of EVs with 4WD system [114]**

EV applications	Weight (kg)	Acceleration 0-100km/h (s)	Maximum power (kW)
Audi e-tron GT	2420	4.1	390 (175 PMSM + 215 PMSM)
Polestar 4 DM	2180	3.8	400 (200 PMSM + 200 PMSM)
BYD Seal	2260	3.8	390 (160 IM + 230 PMSM)
BYD Han	2325	3.9	380 (180 PMSM + 200 PMSM)
Tesla Model 3 DM	1899	4.4	331 (137 IM + 194 PMSM)
Nio ET5 Touring	2265	4.0	360 (150 IM + 210 PMSM)
Volvo EX30	1960	3.6	315 (-)

The application investigated in this study is also a 4WD high performance electric passenger car. The powertrain architecture is shown in Chapter 4, Figure 4.2 (c), where each EM drives an axle with fixed gear ratios. The specifications of the 4WD EV example are shown in Table 7.2.

This 4WD EV can take full advantage of the traction torque, which can be seen from Figure 7.1 that over 350 kW peak power is needed to have the acceleration time lower than 3.8 seconds. The continuous power demand is around 100 kW when the vehicle operates at maximum speed on flat road.

**Table 7.2 Vehicle specifications**

Parameter	Value	Unit
Vehicle mass	2270	kg
Wheel radius	0.35	m
Drag coefficient	0.26	-
Rolling coefficient	0.008	-
Front area	2.36	m <sup>2</sup>
Top speed	225	km/h
Acceleration (0-100km/h)	3.8	s

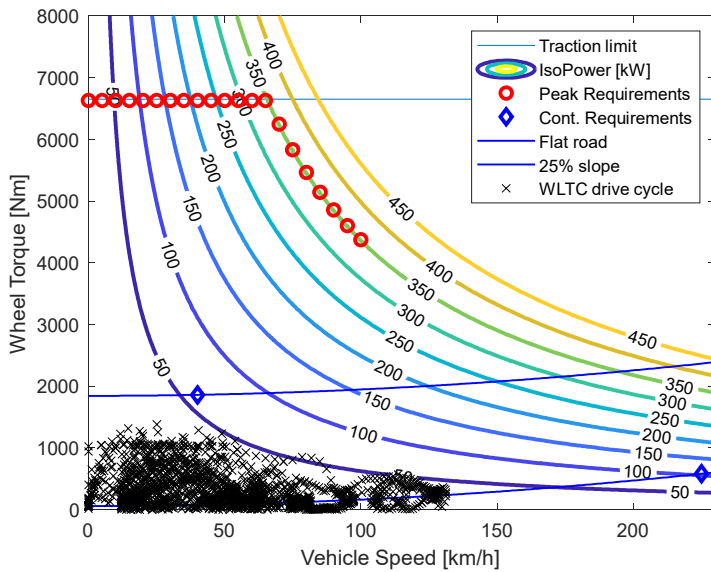


**Figure 7.1 4WD torque requirements on the wheels**

## 7.2. Methodology

For 4WD EVs, there are applications using two identical PMSMs or one PMSM and one IM with different power rating. Two identical EMs can help reduce the R&D efforts and lower the cost compared to the configuration with two individually designed EMs. However, by introducing two distinct types of EMs or two EMs with different sizes, the system can take advantage of their different attributes and thus lower the system cost and energy consumption. In this study, several 4WD configurations are selected to explore the differences and potential benefits among all the study cases, which can be seen in Table 7.3.

Case 1 utilizes two identical PMSMs, one for the front and one for the rear axle, as the benchmark of this study. Case 2 still employs PMSM but with different power ratings, varying from the minimum to maximum power rating factor. Case 3 introduces IM as the secondary drive, trying to explore the potential of increasing system efficiency and lower EM cost by taking advantage of IM's different attribute.

**TABLE 7.3 4WD system configurations**

	EM1	EM2	Power rating factor	Notes
Case 1	PMSM	PMSM	$\alpha_1 = 0.5$	Two identical PMSMs
Case 2	PMSM	PMSM	$\alpha_1 \in (\alpha_{1,min}, \alpha_{1,max})$	Optimal PMSM power rating determined through optimization
Case 3	PMSM	IM	$\alpha_1 \in (\alpha_{1,min}, \alpha_{1,max})$	Optimal PMSM and IM power rating determined through optimization

The powertrain optimization process for the 4WD system is then illustrated in Figure 7.2. The optimization process contains two independent sections: power rating determination and torque distribution optimization. The purpose of the 4WD optimization is to find the optimal torque distribution strategy between two EMs with optimal power rating for each, resulting in the lowest 4WD system cost and operating cost.

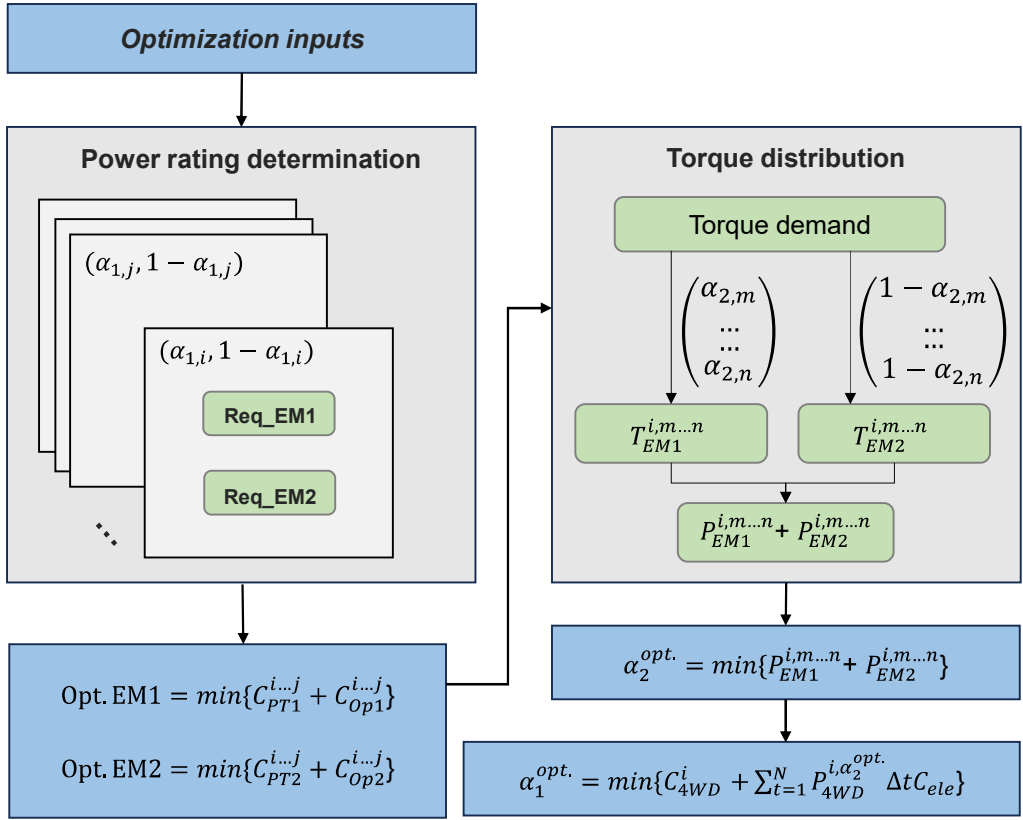


**Figure 7.2** Powertrain optimization methodology for 4WD EV

In the power rating determination section, the factor defining the power rating for each EM is termed as  $\alpha_1$ . The peak and continuous requirements for each EM are expressed by (7.1).

$$\left\{ \begin{array}{l} P_{pk_{EM1}} = \alpha_1 P_{pk_{tot}} \\ P_{pk_{EM2}} = (1 - \alpha_1) P_{pk_{tot}} \\ T_{pk_{EM1}} = \alpha_1 T_{pk_{tot}} \\ T_{pk_{EM2}} = (1 - \alpha_1) T_{pk_{tot}} \\ T_{con_{EM1}} = T_{cont} \\ T_{con_{EM2}} = T_{cont} \end{array} \right. \quad (7.1)$$

Where  $P_{pk_{tot}}$  is the total power requirement,  $T_{pk_{tot}}$  is the peak torque requirement. Each EM should be able to provide the continuous torque needed by the EV.

The power rating factor should follow the rule expressed in (7.2) to make sure the peak power of each EM is larger than its continuous power.

$$\frac{P_{cont}}{P_{peak}} < \alpha_1 < 1 - \frac{P_{cont}}{P_{peak}} \quad (7.2)$$

Once the power and torque requirements for each EM are allocated, two independent powertrain optimizations will be performed. It is important to know that the two EMs are independently optimized, assuming they are independently driving the EV. The optimization goal of the two optimizations is to find the optimal powertrain solution on each axle, which is evaluated by the objective function in (7.3),

$$f(x) = C_{PT}(EM_{ind}, x) + C_{Op}(EM_{ind}, x) \quad (7.3)$$

With the two optimized powertrains/EMs, the second section of the 4WD optimization process is involved. In this section, the torque distribution factor,  $\alpha_2$ , is introduced to split the total torque demand from the EV to each axle. The torque demand for each EM can be substituted as:

$$\begin{cases} g_{EM1}T_{d1} = \alpha_2 T_d \\ g_{EM2}T_{d2} = (1 - \alpha_2)T_d \end{cases} \quad (7.4)$$

Where  $g_{EM1}$  and  $g_{EM2}$  are the transmission gear ratio for each powertrain,  $T_d$  is the total torque demand with the given drive cycle,  $T_{d1}$  and  $T_{d2}$  are the distributed torque for each EM.

Then an offline map search method [115][116] is introduced to find the optimal torque distribution between the two powertrains. With certain  $\alpha_2$  value, the losses for each powertrain at all operating points of the drive cycle can be interpolated with the powertrain efficiency map optimized from the first optimization section. With all  $\alpha_2$  value evaluated, the optimal distribution ratio,  $\alpha_2^{opt.}$ , can be found at each operating point to minimize the total losses of the two powertrains.

The torque distribution optimization problem can therefore be formalized as follows:

$$\min: \{ f(\alpha_2) = P_{loss,EM1}(\omega_{EM1}, T_{d1}) + P_{loss,EM2}(\omega_{EM2}, T_{d2}) \} \quad (7.5)$$

$P_{loss,EM1}$  are the losses for EM1 and  $P_{loss,EM2}$  for EM2,  $\alpha_2$  can be varied within the range of 0 to 1, where 0 and 1 signify FWD or RWD, respectively. Values greater than 0 but less than 1 correspond to 4WD mode.

It should be noted that it is assumed that there are clutches between the powertrain and wheel of each axle, activated when one powertrain is disengaged ( $\alpha_2 = 0$  or  $1$ ), to avoid the no-load losses. However, the incorporation of such clutches inevitably leads to elevated cost and system complexity. Despite these considerations, due to the exploratory nature of this research, the consequential effects and considerations related to the clutches are not examined.

Once the optimal  $\alpha_2$  is explored for all the 4WD systems with different power rating, the optimal  $\alpha_1$  can be derived by (7.6)

$$\min: \{ f(\alpha_1) = C_{4WD} + \sum_{t=1}^N \left( P_{EM1}^{\alpha_2^{opt.}} + P_{EM2}^{\alpha_2^{opt.}} \right) \Delta t C_{ele} \} \quad (7.6)$$

Where  $N$  is the total amount of the operating points of the drive cycle,  $\Delta t$  is the time step size and  $C_{ele}$  is the electricity price.

### 7.3. Results

In the optimization of the 4WD system, the computational complexity is significantly increased by the multiple power rating factors. The number of powertrain optimization processes will be several times the number of base EMs in the database. To mitigate the computational load for the 4WD optimization, a limited number of base EMs for PMSM and IM are selected for the optimization.

For case 1, two identical PMSMs are utilized, meaning that the power rating factor is fixed to 0.5. This simplifies the optimization process. The torque distribution strategy in case 1 is straightforward: a 50%:50% ratio is selected. This denotes an equal distribution of the torque demand across both the front and rear axles.

Subsequently, the optimization for case 1 is carried out with the methodology proposed in Figure 7.2 and the results are shown in Table 7.4.

**TABLE 7.4 4WD system optimization results for Case 1**

	Peak Power (kW)	Powertrain cost (€)	Energy consumption (kWh/100km)
EM1	202	1486	14.7
EM2	202	1486	

The optimization process explored two identical powertrains, each with a peak power output of 202 kW. The total power output of the optimized 4WD system amounts to 404 kW, surpassing the specified power demand. As discussed in Chapter 5, the optimizer is aiming to explore the powertrain solution with minimizing the total cost, including the operating cost. This leads to the optimized powertrains present feasible combinations of winding layers and parallel paths that result in the base speed does not match exactly with vehicle requirements, as shown in Figure 7.3.

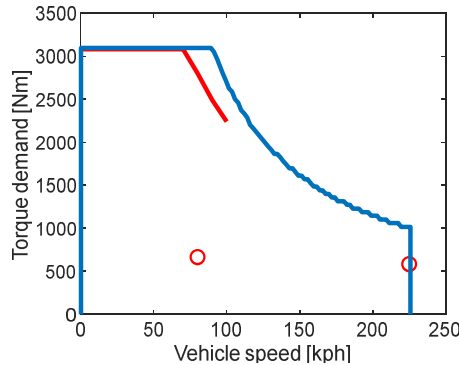


**Figure 7.3** Speed-torque curve of optimized EM under case 1 (Blue) vs EV requirements (Red)

Case 2 expands the scope of the investigation to find the optimal power rating for the two powertrains, while exploring the optimal torque distribution strategy. This analysis encompasses the power rating factor of 0.5. It is important to distinguish that, unlike Case 1 where the EMs on each axle employed identical 2D geometries, the optimized EMs for each axle in Case 2 may exhibit variations in their 2D geometrical configurations.

The outcomes of this case yield a set of powertrain configurations that demonstrate interdependencies among EM geometries, power rating factors and the torque distribution strategies.

This optimization process identifies the optimal power rating factor as 0.5, yielding a maximum power output of 202 kW for EM1 and 202 kW for EM2, as shown in Table 7.5, with energy consumption 14.4 kWh/100km and 2.1% reduction compared to the result of Case 1.

For each combination of vehicle speed and vehicle torque demand, the optimal torque distribution ratio,  $\alpha_2^{opt}$ , can be derived based on the loss information of the powertrains. The optimal torque distribution ratio for the two optimized powertrains is shown in Figure 7.4. When two powertrains with different efficiency characteristics are deployed, the optimal torque distribution ratio is not always 0.5. This underscores the necessity of

**TABLE 7.5 4WD system optimization results for Case 2**

	Peak Power (kW)	Powertrain cost (€)	Energy consumption (kWh/100km)
EM1	202	1486	14.4 (-2.1%)
EM2	202	1486	

tailoring the torque distribution to match the efficiency profiles of the powertrains on each axle.

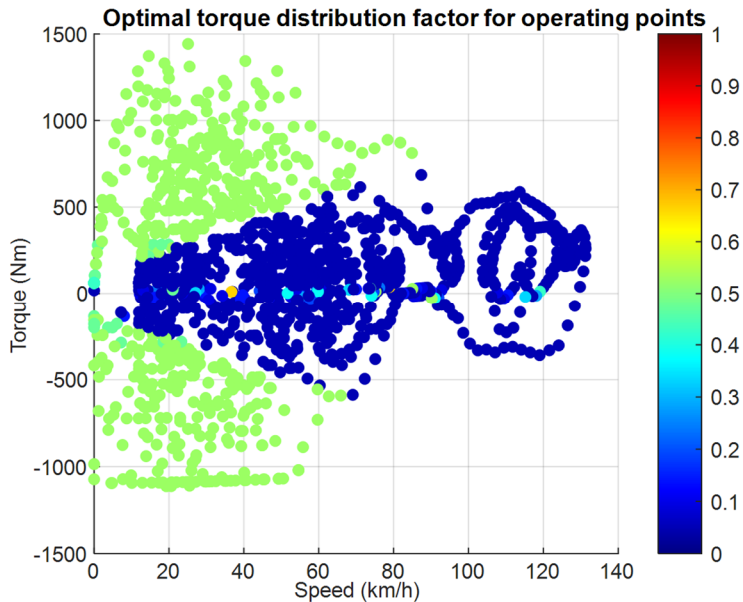


**Figure 7.4** Optimal torque distribution strategy for case 2

It should be noted that the optimal torque distribution factor is explored within the applied drive cycle. When the peak torque and power is required, the two powertrains are equally involved at the same time.

As discussed before, the 4WD system can benefit from the different characteristics of EM on each axle. In comparison to PMSMs, IMs present a more cost-effective solution, primarily due to their lower manufacturing costs. Notably, the efficiency profile of IMs typically peaks in regions at high speed. This differential in performance characteristics between PMSMs and IMs allows for an allocation of working tasks within the 4WD system, where each EM type can be utilized that aligns closely with its high-efficiency region. For



instance, the IM's optimal efficiency at high speeds makes it particularly suited for EV cruising.

With this in mind, an optimized PMSM and optimized IM are identified with the power rating factor of 0.41. The maximum power output of PMSM is 185 kW and 268 kW for IM, as shown in Table 7.6. With introducing IM, the 4WD system cost can be decreased compared to that in Case 2, where two PMSMs are employed.

**TABLE 7.6 4WD system optimization results for Case 3**

	Peak Power (kW)	Powertrain cost (€)	Energy consumption (kWh/100km)
<b>EM1 (PMSM)</b>	185	1343	13.9 (-5.8% to case 1 -3.6% to case 2)
<b>EM2 (IM)</b>	268	1442	

In case 3, the torque distribution for the 4WD system is shown in Figure 7.5, where most operating points characterized by low torque and high speed are allocated to the IM, while the majority of other operating points are assigned to the PMSM. This takes advantage of the efficiency characteristics of each EM type.

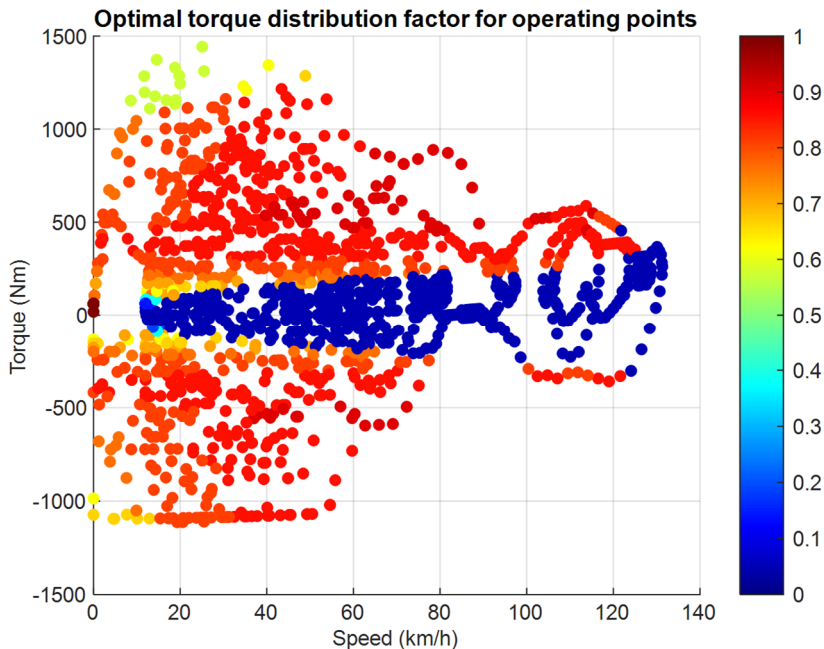


**Figure 7.5** Optimal torque distribution strategy for case 2

The energy consumption of Case 3 demonstrates a reduction (3.6%) compared to that in Case 2, as illustrated in Table 7.6. Furthermore, the cost of powertrain utilizing IM in Case 3 reveals a 6.7% reduction compared to the powertrain employed in Case 2. This cost reduction is a direct consequence of the employment of IM, which are generally less expensive than PMSMs due to the absence of rare-earth materials. By effectively integrating the IM, the 4WD system achieves a more economical solution without compromising on performance or efficiency.

Overall, the energy consumption in Case 1 is the highest among the evaluated scenarios, it offers the most straightforward solution by employing two identical powertrains. However, this approach simplifies the powertrain design process, reducing the effort required for development. Case 3 offers the best performance regarding the powertrain cost and system efficiency. Nevertheless, it increases the system complexity by employing two different powertrain systems.

This study aims to address several critical questions, including determining the optimal power rating between axles and exploring the most effective torque distribution strategy. Throughout the optimization process of the 4WD system, various factors influence the outcomes.

For example, the database comprising only 50 base IMs and 100 PMSMs constrains the potential to explore a better solution for the 4WD powertrain system. Better solutions can be achieved with larger database and customized constraints for the three cases.

Furthermore, the assumption of two clutches on each axle introduces additional considerations. Following the optimal torque distribution strategy between the two powertrains could lead to frequent mode shifts. This is likely to incur extra energy losses associated with clutch operation and potentially impact the Noise, Vibration, and Harshness (NVH) performance of the vehicle.



# Chapter 8 Conclusion and Future work

## 8.1. Conclusion

In this thesis, detailed powertrain optimization is performed from a system level for electric passenger cars. Chapter 2 introduces three different types of EMs and the method to evaluate the EM's performance from various aspects, including electromagnetic, thermal and cost. Chapter 3 discusses the modelling for PEC and MT, which not only covers the estimation of power losses but also internal sizing and optimization process. Chapter 4 briefly introduces the optimization structure, including the optimization inputs, objectives and how the optimizer operates. In Chapter 5, a complete comparison analysis for the three EM types is conducted, showing the advantages and disadvantages among the optimized EMs with given EV application. In Chapter 6, an equally concerned problem in automotive industry, the platform-based powertrain design is raised. With the selected EV platform (three different EV classes), a series of powertrain products, which has the same EM 2D topology, is designed by the methodology, showing good cost competitiveness against the three individually optimized powertrains. The studies in Chapter 5 and 6 are with 2WD EVs. Chapter 7 expands the analysis from 2WD EV to 4WD EV, trying to find the optimal powertrain power rating for each axle and the optimal torque split ratio to have the optimal system cost and efficiency.

The additional development of the tool based on FEMM has facilitated the design of various types of EMs, including PM machines with various rotor topologies, IM, SRM and EESM. Through postprocessing the raw data collected from the FE models using selected algorithms, the EM power losses and other electromagnetic characteristics are derived.

Nevertheless, achieving optimal EM design requires a multi-disciplinary approach. For example, the efforts to improve the EM's performance, such as introducing new winding techniques, thinner lamination materials and more efficient cooling system, inevitably leads to a cost rise, which is also a concern in automotive industry. Balancing these factors demands expertise in electromagnetics, materials, thermal dynamics, and cost analysis.

Furthermore, thinking from a system perspective during the powertrain design and optimization is crucial, due to the complex interactions among EM, PEC and MT. For example, increasing the EM mechanical speed can help downsize the EM and thus lead to

higher power density. However, this may introduce elevated speed-dependent losses both for the EM and MT.

Introducing hairpin winding increases these complexities. The discrete nature of number of turns and the intervals between feasible winding configurations significantly influence the phase current, thereby affecting power module design of the PEC, which is critical to PEC cost and performance. These interactions complicate the task of finding an optimal powertrain solution.

A comprehensive optimization approach requires both the performance and cost models. With EM databases comprising thousands of base EMs as input, each subject to thousands of powertrain solutions generated through the scaling methods and PEC/MT models, swift evaluation becomes imperative. Consequently, all of these requires the applied models have fast evaluation time.

In this thesis, the primary optimization input involves the base EMs, supplemented by fixed input parameters for other components and the vehicle requirements. However, the optimization tool possesses broader capabilities. Explorations can extend to different material selections, alternative winding techniques, power module variants, multi-speed transmissions and diverse thermal settings.

## 8.2. Future work

The efficiency of the powertrain is crucial in vehicle design, significantly impacting the required battery capacity with a given range requirement. A more efficient powertrain reduces the amount of energy drawn from the battery, thereby potentially decreasing the battery size and cost. Introducing a battery model into the study allows for a more comprehensive evaluation of the powertrain design, considering both performance and economic factors.

With regard to the iron loss estimation, it is derived with the flux density data collected from two positions in stator yoke and tooth, leading to lower accuracy compared to the losses estimated by FEA method. Introducing supplementary data collection points across the stator is worthy of being explored.

The choice of switching frequency in inverter can affect its losses. There are applications using discrete or continuous switching frequency to reduce the PEC losses [22] [117], compared to the fixed switching frequency in this thesis. The impact of varying switching frequency on the PEC losses can be investigated in the future.

The optimizations in this thesis have done on a balance between powertrain cost and operational cost. Other aspects, like environmental impact could also be included in the optimization process.

EESMs are emerging as a viable alternative to PMSMs in EV applications. This shift is primarily due to their non-rare-earth material usage and superior field weakening capabilities. Expanding the model to include EESMs will allow for an in-depth study of these advantages.

As previously discussed, the size of the database significantly influences the optimization process, with larger databases offering a greater possibility of identifying better powertrain solutions. However, the generation of such databases through FE simulations is inherently time-consuming. Furthermore, increasing the database size by reducing the geometry variable intervals requires substantial computational resources, leading to significant time escalation for database generation.

To address these challenges in future research, a hybrid strategy incorporating both FE simulations and machine learning techniques can be adopted [118][119][120]. This strategy could accelerate the database generation process, reducing both time and computational resource requirements, thereby improving the powertrain optimization.



# Appendice





# Appendix A

## Magnet loss estimation

Without the stator current, the magnetic field in magnets can be seen as constant. However, with the influence of alternating current in the stator, the flux density waveforms in magnets also vary with different rotor positions and stator current. However, the static magnetic field does not contribute to the magnet losses. Therefore, the alternating magnetic field can be expressed as sine waveform and uniform in magnetization direction. in (A.1).

$$B_z = B_a \cdot \sin(\omega t) \hat{z} \tag{A.1}$$

The magnetic field can be described as a homogenous and periodical square-wave field in  $xy$ -plane. The magnitude of the magnetic field in  $xy$ -plane changes along with the B-field in  $z$  direction. That is, the B-field in  $xy$ -plane can be seen as constant along  $x$ - and  $y$ -axis under certain time, which can be seen in Figure A.1.

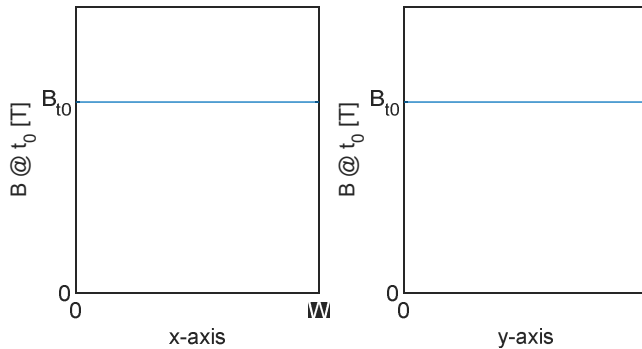


**Figure A.1** Magnetic field in  $x$ - and  $y$ -axis of the magnet

The B-field in  $xy$ -plane can be formulated as a two-dimensional Fourier series in (A.2).

$$B_{z,xy} = B_a \left(\frac{4}{\pi}\right)^2 \sum_{m=1,3,5\dots}^{\infty} \frac{1}{m} \sin\left(\frac{m\pi}{w}x\right) \sum_{n=1,3,5\dots}^{\infty} \frac{1}{n} \sin\left(\frac{n\pi}{l}y\right) \sin(\omega t) \quad (\text{A.2})$$

Where  $m$  and  $n$  is the order of the magnetic field harmonics, and  $\omega$  is the frequency of the B-field in z direction. To simplify the equation, we define:

$$B_{mn} = B_a \left(\frac{4}{\pi}\right)^2 \frac{1}{mn}$$

$$\bar{m} = \frac{m\pi}{w} \quad (\text{A.3})$$

$$\bar{n} = \frac{n\pi}{l}$$

In Faraday's law, the B-field is linked to the electrical field.

$$-\frac{\partial \mathbf{B}}{\partial t} = \begin{vmatrix} \hat{x} & \hat{y} & \hat{z} \\ \frac{\partial}{\partial x} & \frac{\partial}{\partial y} & \frac{\partial}{\partial z} \\ E_x & E_y & E_z \end{vmatrix} \quad (\text{A.4})$$

Because only the z-direction of the induced field is considered, the solution of that equation is:

$$-\frac{\partial \mathbf{B}}{\partial t} = \frac{\partial E_y}{\partial x} - \frac{\partial E_x}{\partial y}$$

$$= -\omega B_{mn} \sum_{m=1,3,5\dots}^{\infty} \sin(\bar{m}x) \sum_{n=1,3,5\dots}^{\infty} \sin(\bar{n}y) \cos(\omega t) \quad (\text{A.5})$$

To satisfy the given partial differential equation, it is assumed that the electrical field can be expressed in (A.6 and A.7)

$$E_x = a \sum_{m=1,3,5\dots}^{\infty} \sum_{n=1,3,5\dots}^{\infty} \sin(\bar{m}x) \cos(\bar{n}y) \cos(\omega t) \quad (\text{A.6})$$

$$E_y = b \sum_{m=1,3,5\dots}^{\infty} \sum_{n=1,3,5\dots}^{\infty} \cos(\bar{m}x) \sin(\bar{n}y) \cos(\omega t) \quad (\text{A.7})$$

The partial derivative can be calculated.

$$\frac{\partial E_y}{\partial x} - \frac{\partial E_x}{\partial y} = (-\bar{m}b + \bar{n}a) \sum_{m=1,3,5\dots}^{\infty} \sum_{n=1,3,5\dots}^{\infty} \sin(\bar{m}x) \sin(\bar{n}y) \cos(\omega t)$$

Let

$$(-\bar{m}b + \bar{n}a) = -\omega B_{mn}$$

We can get:

$$a = -\frac{\bar{n}\omega B_{mn}}{\bar{m}^2 + \bar{n}^2}$$

$$b = \frac{\bar{m}\omega B_{mn}}{\bar{m}^2 + \bar{n}^2}$$

Thus, the electrical field can be expressed as in (A.8) and (A.9)

$$E_x = -\frac{\bar{n}\omega B_{mn}}{\bar{m}^2 + \bar{n}^2} \sum_{m=1,3,5\dots}^{\infty} \sum_{n=1,3,5\dots}^{\infty} \sin(\bar{m}x) \cos(\bar{n}y) \cos(\omega t) \quad (\text{A.8})$$

$$E_y = -\frac{\bar{m}\omega B_{mn}}{\bar{m}^2 + \bar{n}^2} \sum_{m=1,3,5\dots}^{\infty} \sum_{n=1,3,5\dots}^{\infty} \cos(\bar{m}x) \sin(\bar{n}y) \cos(\omega t) \quad (\text{A.9})$$

The loss due to the eddy current distribution for one frequency component is:

$$P_{mag} = \int_{z=0}^h \int_{y=0}^l \int_{x=0}^w \sigma (E_x^2 + E_y^2) dx dy dz$$

$$= lhw \frac{\sigma \omega^2 B_{mn}^2}{8(\bar{m}^2 + \bar{n}^2)}$$

So, the magnet losses considering all the harmonics is expressed in (A.10)

$$\begin{aligned}
 P_{mag} &= lhw \sum_{m=1,3,5\dots}^{\infty} \sum_{n=1,3,5\dots}^{\infty} \frac{\sigma \omega^2 B_{mn}^2}{8(\bar{m}^2 + \bar{n}^2)} \\
 &= \frac{32l^3 h W^3 \sigma \omega^2 B_a^2}{\pi^6} \sum_{m=1,3,5\dots}^{\infty} \sum_{n=1,3,5\dots}^{\infty} \frac{1}{(L^2 m^2 + W^2 n^2) m^2 n^2}
 \end{aligned} \tag{A.10}$$

# Reference

- [1] Neil King, EVs Forecast to Account for Two Thirds of Global Light-Vehicle Sales in 2035, *ev-volumes*, November 21, 2023.
- [2] IEA (2023), *Global EV Outlook 2023*, IEA, Paris <https://www.iea.org/reports/global-ev-outlook-2023>.
- [3] The global electric vehicle market overview in 2024: statistics & forecasts. *Virta.global*. <https://www.virta.global/en/global-electric-vehicle-market>.
- [4] Guide to Chinese climate policy: Electric Vehicles, Oxford Institute of Energy Studies. <https://chineseclimatepolicy.oxfordenergy.org/book-content/domestic-policies/vehicles/electric-vehicles/>
- [5] Federal EV policy, Electrification Coalition, <https://electrificationcoalition.org/work/federal-ev-policy/>
- [6] EU ban on the sale of new petrol and diesel cars from 2035 explained. <https://www.europarl.europa.eu/news/en/headlines/economy/20221019STO44572/eu-ban-on-sale-of-new-petrol-and-diesel-cars-from-2035-explained> .
- [7] Mauler, Lukas & Duffner, Fabian & Zeier, Wolfgang & Leker, Jens. (2021). Battery cost forecasting: A review of methods and results with an outlook to 2050. *Energy & Environmental Science*. 14. 10.1039/D1EE01530C.
- [8] Jianping Wen, Dan Zhao, Chuanwei Zhang, An overview of electricity powered vehicles: Lithium-ion battery energy storage density and energy conversion efficiency, *Renewable Energy*, Volume 162,2020,Pages 1629-1648.
- [9] Trends in charging infrastructure, *Global EV Outlook 2023*, <https://www.iea.org/reports/global-ev-outlook-2023/trends-in-charging-infrastructure>
- [10] An, J., Gemeinder, Y. & Binder, A. Downsizing possibilities of a PM synchronous motor for a hybrid vehicle. *Elektrotech. Inftech*. 136, 143–152 (2019).
- [11] J.M.D. Coey, Perspective and Prospects for Rare Earth Permanent Magnets, *Engineering*, Volume 6, Issue 2, 2020, Pages 119-131, ISSN 2095-8099.
- [12] C. Du-Bar, A. Mann, O. Wallmark and M. Werke, "Comparison of Performance and Manufacturing Aspects of an Insert Winding and a Hairpin Winding for an Automotive

- Machine Application," 2018 8th International Electric Drives Production Conference (EDPC), Schweinfurt, Germany, 2018, pp. 1-8.
- [13] K. Zhou, A. Ivanco, Z. Filipi and H. Hofmann, "Finite-Element-Based Computationally Efficient Scalable Electric Machine Model Suitable for Electrified Powertrain Simulation and Optimization," in IEEE Transactions on Industry Applications, vol. 51, no. 6, pp. 4435-4445, Nov.-Dec. 2015.
- [14] S. Stipetic, D. Zarko and M. Popescu, "Scaling laws for synchronous permanent magnet machines," 2015 Tenth International Conference on Ecological Vehicles and Renewable Energies (EVER), Monte Carlo, Monaco, 2015, pp. 1-7.
- [15] G. Dilevrano, P. Ragazzo, S. Ferrari, G. Pellegrino and T. Burrell, "Magnetic, Thermal and Structural Scaling of Synchronous Machines," 2022 IEEE Energy Conversion Congress and Exposition (ECCE), Detroit, MI, USA, 2022, pp. 1-8.
- [16] C. Marchand, M. Djami, M. H. Hassan, G. Krebs, P. Dessante and L. Belhaj, "Metamodel-Based Electric Vehicle Powertrain Optimization : A Drive Cycle Approach," 2023 IEEE International Electric Machines & Drives Conference (IEMDC), San Francisco, CA, USA, 2023, pp. 1-5.
- [17] H. Bydén, E. Bourniche, G. Domingues, M. Alaküla, A. Leblay and F. Marquez, "Electro-thermal Models of Power Modules for Stochastic Optimization of Inverters," 2023 IEEE Transportation Electrification Conference & Expo (ITEC), Detroit, MI, USA, 2023, pp. 1-6.
- [18] M. G. Tehrani, J. Kelkka, J. Sopanen, A. Mikkola and K. Kerckänen, "Transmission configuration effect on total efficiency of Electric Vehicle powertrain," 2014 16th European Conference on Power Electronics and Applications, Lappeenranta, Finland, 2014, pp. 1-9.
- [19] L. Jacob and H. Johanna, Transmission Modelling for Optimization of Electric Powertrains, Master thesis, Lund University, 2021.
- [20] Fyhr, P. Electromobility: Materials and Manufacturing Economics. PhD thesis, Lund University, Sweden, 2018
- [21] Ralph, Burkart & Kolar, Johann. (2013). Component cost models for multi-objective optimizations of switched-mode power converters. 2013 IEEE Energy Conversion Congress and Exposition, ECCE 2013. 2139-2146. 10.1109/ECCE.2013.6646971.
- [22] G. Domingues. Modelling, Optimization and Analysis of Electromobility Systems. PhD thesis, Lund University, Sweden, 2018
- [23] M. S. Rafiq and J. -W. Jung, "A Comprehensive Review of State-of-the-Art Parameter Estimation Techniques for Permanent Magnet Synchronous Motors in Wide Speed Range," in IEEE Transactions on Industrial Informatics, vol. 16, no. 7, pp. 4747-4758, July 2020.
- [24] J.M.D. Coey, Perspective and Prospects for Rare Earth Permanent Magnets, Engineering, Volume 6, Issue 2,2020, Pages 119-131, ISSN 2095-8099.

- [25] Peyman Niazi, "Permanent Magnet Assisted Synchronous Reluctance Motor Design and Performance Improvement," Texas A&M University, PhD. Thesis 2005.
- [26] Reinap, A., Hagstedt, D., Márquez, F., Loayza, Y., Alaküla, M. (2008), "Development of a radial flux machine design environment". International Conference on Electrical Machines (ICEM2008), Vilamoura, Portugal, Sept. 6-9, 2008.
- [27] D. C. Meeker, Finite Element Method Magnetics, Version 4.2
- [28] Vijayakumar, K., Karthikeyan, R., Paramasivam, S., Arumugam, R., & Srinivas, K. N. (2008). Switched reluctance motor modeling, design, simulation, and analysis: a comprehensive review. *IEEE Transactions on Magnetics*, 44(12), 4605-4617.
- [29] Estenlund, Samuel & Alakula, Mats & Reinap, A. (2016). PM-less machine topologies for EV traction: A literature review. 1-6. 10.1109/ESARS-ITEC.2016.7841341.
- [30] S. Estenlund, A. Tokat, J. Engqvist and M. Alaküla, "Dovetail Design for Direct Cooled Rotor: Design and Manufacturing," 2022 International Conference on Electrical Machines (ICEM), Valencia, Spain, 2022, pp. 2121-2127.
- [31] G. Joksimović, A. Kajević, M. Mezzarobba and A. Tessoro, "Optimal Rotor Bars Number in Four Pole Cage Induction Motor with 36 Stator Slots - Part I: Numerical Modeling," 2020 International Conference on Electrical Machines (ICEM), 2020, pp. 502-508.
- [32] T. Aho, J. Nerg and J. Pyrhonen, "The Effect of the Number of Rotor Slits on the Performance Characteristics of Medium-Speed Solid Rotor Induction Motor," 2006 3rd IET International Conference on Power Electronics, Machines and Drives - PEMD 2006, 2006, pp. 515-519.
- [33] M. Valtonen, A. Parviainen and J. Pyrhonen, "The Effects of the Number of Rotor Slots on the Performance Characteristics of Axial-Flux Aluminium-Cage Solid-Rotor Core Induction Motor," 2007 IEEE International Electric Machines & Drives Conference, 2007, pp. 668-672.
- [34] Rasmus Andersson. On the design of Electric Traction Machines, PhD thesis, Lund University, Lund, Sweden, 2014.
- [35] A. Arzillo et al., "An Analytical Approach for the Design of Innovative Hairpin Winding Layouts," 2020 International Conference on Electrical Machines (ICEM), Gothenburg, Sweden, 2020, pp. 1534-1539.
- [36] Shams Ghahfarokhi, Payam & Podgornovs, Andrejs & Kallaste, Ants & Vaimann, Toomas & Belahcen, Anouar & Cardoso, A.J.M. (2021). Oil Spray Cooling with Hairpin Windings in High- Performance Electric Vehicle Motors. 10.1109/IWED52055.2021.9376390.
- [37] Xue, S. Maximising E-Machine Efficiency with Hairpin Windings; White Paper (Report); motor design Ltd.: Wrexham, UK, 2021; pp. 1-7.
- [38] Zhao, Y.; Li, D.; Pei, T.; Qu, R. Overview of the rectangular wire windings AC electrical machine. *CES Trans. Electr. Mach. Syst.* 2019, 3, 160-169.



- [39] Bianchi, N.; Berardi, G. Analytical Approach to Design Hairpin Windings in High Performance Electric Vehicle Motors. In Proceedings of the 2018 IEEE Energy Conversion Congress and Exposition, ECCE 2018, Portland, OR, USA, 23–27 September 2018; pp. 4398–4405.
- [40] Preki, E.; Nuzzo, S.; Valente, G.; Gerada, D.; Barater, D.; Degano, M.; Buticchi, G.; Gerada, C. Segmented Hairpin Topology for Reduced Losses at High Frequency Operations. *IEEE Trans. Transp. Electr.* 2021, 8, 688–698.
- [41] C. Du-Bar; O. Wallmark. Eddy Current Losses in a Hairpin Winding for an Automotive Application. 2018 XIII International Conference on Electrical Machines (ICEM), Alexandroupoli, 2018, pp. 710-716.
- [42] T. Gerlach; R. Steckel; T. Hubert; A. Kremser. Eddy current loss analysis in permanent magnets of synchronous machines. 2016 6th International Electric Drives Production Conference (EDPC), Nuremberg, 2016, pp. 246-252.
- [43] M. Lu, G.Domingues-Olavarria, F.J.Márquez-Fernández, P. Fyhr and M. Alaküla, "Electric Drivetrain Optimization for a Commercial Fleet with Different Degrees of Electrical Machine Commonality," *Energies* 2021, 14, 2989.
- [44] "Breakthrough! Haosen has mastered key technology for 10-layer Hair-pin motor stator production, speeding up the commercialization steps for new energy customers," <https://www.yizhanglian.com/en/?news/367.html>
- [45] T. Zou et al., "A Comprehensive Design Guideline of Hairpin Windings for High Power Density Electric Vehicle Traction Motors," in *IEEE Transactions on Transportation Electrification*, vol. 8, no. 3, pp. 3578-3593, Sept. 2022.
- [46] Power Electronics. Devices, Converters, Control and Applications. 2019. Mats Alaküla, Per Karlsson and Hans Bångtsson.
- [47] Du-Bar, C.; Wallmark, O. Eddy Current Losses in a Hairpin Winding for an Automotive Application. In Proceedings of the 2018 XIII International Conference on Electrical Machines (ICEM), Alexandroupoli, Greece, 3–6 September 2018; pp. 710–716.
- [48] T. Gerlach, R. Steckel, T. Hubert and A. Kremser, "Eddy current loss analysis in permanent magnets of synchronous machines," 2016 6th International Electric Drives Production Conference (EDPC), Nuremberg, Germany, 2016, pp. 246-252.
- [49] Gyselinck, Johan & Dular, Patrick & Geuzaine, Christophe & Sabariego, Ruth. (2009). Direct Inclusion of Proximity-Effect Losses in Two-Dimensional Time-Domain Finite-Element Simulation of Electrical Machines.
- [50] P. Mancinelli, S. Stagnitta and A. Cavallini, "Qualification of Hairpin Motors Insulation for Automotive Applications," in *IEEE Transactions on Industry Applications*, vol. 53, no. 3, pp. 3110-3118, May-June 2017.

- [51] A. Krings, 'Iron Losses in Electrical Machines - Influence of Material Properties, Manufacturing Processes, and Inverter Operation', PhD dissertation, KTH Royal Institute of Technology, Stockholm, 2014.
- [52] G. Bertotti, "General properties of power losses in soft ferromagnetic materials," in IEEE Transactions on Magnetics, vol. 24, no. 1, pp. 621-630, Jan. 1988.
- [53] C. Steinmetz, "On the law of hysteresis (originally published in 1892), " Proceedings of the IEEE, vol. 72, no. 2, pp. 197-221, 1984.
- [54] L. Colombo, A. Tokat, K. Bitsi, F. J. Márquez-Fernández and M. Alaküla, "Performance Degradation due to Cut Edge Effect for an Axial-Flux Induction Machine," 2022 International Conference on Electrical Machines (ICEM), Valencia, Spain, 2022, pp. 1253-1259.
- [55] Z. Huang, J. Fang, X. Liu, and B. Han, "Loss calculation and thermal analysis of rotors supported by active magnetic bearings for high-speed permanent-magnet electrical machines," IEEE Trans. Ind. Electron., vol. 63, no. 4, pp. 2027–2035, Apr. 2016.
- [56] R. Wrobel, G. Vainel, C. Copeland, T. Duda, D. Staton, and P. H. Mellor, "Investigation of mechanical loss components and heat transfer in an axial-flux PM machine," IEEE Trans. Ind. Appl., vol. 51, no. 4, pp. 3000–3011, Jul./Aug. 2015.
- [57] Morimoto, S.; Tong, Y.; Takeda, Y.; Hirasu, T. Loss minimization control of permanent magnet synchronous motor drives. IEEE Trans. Ind. Electron. 1994, 41, 511–517.
- [58] Kang, Gyu-Hong, Jin Hur, Hyuk Nam, Jung-Pyo Hong and Gyu-Tak Kim. "Analysis of irreversible magnet demagnetization in line-start motors based on the finite-element method." IEEE Transactions on Magnetics 39 (2003): 1488-1491.
- [59] Boldea, I, and Nasar. S.A. (2009). The Induction Machines Design Handbook. (2nd ed.), CRC Press.
- [60] Selema, A.; Ibrahim, M.N.; Sergeant, P. "Electrical Machines Winding Technology: Latest Advancements for Transportation Electrification. " Machines 2022, 10, 563.
- [61] S. -H. Park, E. -C. Lee, J. -C. Park, S. -W. Hwang and M. -S. Lim, "Prediction of Mechanical Loss for High-Power-Density PMSM Considering Eddy Current Loss of PMs and Conductors," in IEEE Transactions on Magnetics, vol. 57, no. 2, pp. 1-5, Feb. 2021, Art no. 6300205.
- [62] Stipetic S, Zarko D, Popescu M. Ultra-fast axial and radial scaling of synchronous permanent magnet machines[J]. IET Electric Power Applications, 2016, 10(7): 658-666.
- [63] G. Domingues-Olavarría, F. J. Márquez-Fernández, P. Fyhr, A. Reinap, M. Andersson and M. Alaküla, "Optimization of Electric Powertrains Based on Scalable Cost and Performance Models," in IEEE Transactions on Industry Applications, vol. 55, no. 1, pp. 751-764, Jan.-Feb. 2019.

- [64] M. Sanada, Y. Inoue and S. Morimoto, "Rotor structure for reducing demagnetization of magnet in a PMASynRM with ferrite permanent magnet and its characteristics," 2011 IEEE Energy Conversion Congress and Exposition, Phoenix, AZ, USA, 2011, pp. 4189-4194.
- [65] G. Choi and T. M. Jahns, "Demagnetization characteristics of permanent magnet synchronous machines," IECON 2014 - 40th Annual Conference of the IEEE Industrial Electronics Society, Dallas, TX, USA, 2014, pp. 469-475.
- [66] T. A. Huynh and M. -F. Hsieh, "Irreversible Demagnetization Analysis for Multilayer Magnets of Permanent Magnet-Assisted Synchronous Reluctance Machines Considering Current Phase Angle," in IEEE Transactions on Magnetics, vol. 55, no. 7, pp. 1-9, July 2019, Art no. 8106609.
- [67] Øyvind Sommer Klyve, Magnetic Modelling of Saturated IPMSMs, for Improved Torque Estimation and Accurate MTPA Control. Master thesis, Norwegian University of Science and Technology, 2021
- [68] P. -O. Gronwald and T. A. Kern, "Traction Motor Cooling Systems: A Literature Review and Comparative Study," in IEEE Transactions on Transportation Electrification, vol. 7, no. 4, pp. 2892-2913, Dec. 2021.
- [69] Marquez, F., Reinap, A., Huang, Z., & Alaküla, M. (2011). "Dynamic Evaluation of the Overloading Potential of a Convection Cooled Permanent Magnet Synchronous Motor," IEMDC 2011, pp. 13-18.
- [70] Gunnar Kylander. Thermal modelling of small cage induction motors. PhD thesis, Chalmers Institute of Technology, 1995.
- [71] Jeon, K.; Park, M.; Park, J.; Choi, H.; Lee, K.-D.; Lee, J.-J.; Kim, C.-W. Analysis of Cooling Characteristics of Permanent Magnet Synchronous Motor with Different Water Jacket Design Using Electromagnetic–Thermal Fluid Coupled Analysis and Design of Experiment. *Machines* 2023, 11, 903.
- [72] NdFeB magnet, Currency Euro, Accessed 2023-08-14, Available: <https://www.magnet-shop.com>.
- [73] Emile Detry, Five Steps for Solving the Rare-Earth Metals Shortage. BCG analysis, <https://www.bcg.com/publications/2023/five-steps-for-solving-the-rare-earth-metals-shortage>.
- [74] Copper Prices - 45 Year Historical Chart, <https://www.macrotrends.net/1476/copper-prices-historical-chart-data>. (2024-02-19).
- [75] J.-E. Ståhl, C. Andersson, and M. Jönsson, "A basic economic model for judging production development," in Proceedings of the 1st International Swedish Production Symposium, 2007.
- [76] J. Hagedorn, F. S.-L. Blanc, and J. Fleischer, *Automation*. Berlin, Germany: Springer, 2018, pp. 245–300.

- [77] Riedel, Andreas & Masuch, Michael & Weigelt, Michael & Gläbel, Tobias & Kühn, Alexander & Reinstein, Sebastian & Franke, Jörg. (2018). Challenges of the Hairpin Technology for Production Techniques. 10.23919/ICEMS.2018.8549105.
- [78] John S. Agapiou, Development on Die-Cast Copper Motor Rotors – Casting Considerations, *Manufacturing Letters*, Volume 33, Supplement, 2022, Pages 310-321, ISSN 2213-8463.
- [79] Mechler GC, Manufacturing and Cost Analysis for Aluminium and Copper Die Cast Induction Motors for GM's Powertrain and R&D Divisions, Master thesis, MIT, USA, 2010.
- [80] X. She, A. Q. Huang, Ó. Lucía and B. Ozpineci, "Review of Silicon Carbide Power Devices and Their Applications," in *IEEE Transactions on Industrial Electronics*, vol. 64, no. 10, pp. 8193-8205, Oct. 2017.
- [81] A. Wintrich, U. Nicolai, W. Tursky and T. Reimann, Application manual power semiconductors, Semikron International, 2015.
- [82] R. Burkart and J. W. Kolar, 'Component cost models for multi-objective optimizations of switched-mode power converters,' 2013 IEEE Energy Conversion Congress and Exposition, Denver, CO, USA, 2013, pp. 2139-2146.
- [83] Volk, Andreas & Leighton, Michael. (2020). Integrated Development Program for Electrified Drivetrains. *ATZ worldwide*. 122. 40-45. 10.1007/s38311-020-0251-8.
- [84] State of the art development methods for EV drivelines. Report. [https://www.avl.com/documents/4053291/8226613/State+of+the+Art+Development+Methodologies+for+Hybrids+and+eDrives\\_Andreas+Volk.pdf](https://www.avl.com/documents/4053291/8226613/State+of+the+Art+Development+Methodologies+for+Hybrids+and+eDrives_Andreas+Volk.pdf)
- [85] Why the Porsche Taycan's Two-Speed Gearbox Is Such a Big Deal. <https://www.wired.com/story/electric-car-two-speed-transmission-gearbox/>
- [86] Vu N. A new study on the optimal prediction of partial transmission ratios of three-step helical gearboxes with second-step double gear-set. *WSEAS Transactions on Applied and Theoretical Mechanics*, 2007; 2:229–38.
- [87] ISO. ISO 6336-1:2019(E). Calculation of load capacity of spur and helical gears - Part 2: Basic principles, introduction and general influence factors. International Standard, 2019.
- [88] ISO. ISO 6336-3:2019(E). Calculation of load capacity of spur and helical gears - Part 3: Calculation of tooth bending strength. International Standard, 2019.
- [89] ISO. ISO/TR 14179-1:2001(E). Gears - Thermal capacity - Part 1: Rating gear drives with thermal equilibrium at 95 °C sump temperature. International Standard, 2001.
- [90] ISO. ISO/TR 14179-2:2001(E). Gears - Thermal capacity - Part 2: Thermal load-carrying capacity. International Standard, 2001.
- [91] Spanoudakis, P, Moschopoulos, G, Stefanoulis, T, Sarantinoudis, N, Papadokokolakis, E, Ioannou, I, Piperidis, S, Doitsidis, L, Tsourveloudis, N.C. "Efficient Gear Ratio Selection of a

Single-Speed Drivetrain for Improved Electric Vehicle Energy Consumption,” *Sustainability* 2020, 12, 9254.

- [92] Motorfinitly, Front-Wheel Drive vs. Rear-Wheel Drive: What do Consumers Prefer, Online, <https://www.motorfinitly.uk/blog/fwd-vs-rwd/#fwdvsrwd>
- [93] De Pinto, Stefano & Mantriota, Giacomo & Bottiglione, & Sorniotti, & Perlo, Pietro & Viotto, Fabio & Camocardi, Pablo. A Four-Wheel-Drive Fully Electric Vehicle Layout with Two-Speed Transmissions. 2014 IEEE Vehicle Power and Propulsion Conference, VPPC 2014. 10.1109/VPPC.2014.7006997.
- [94] Anselma, Pier Giuseppe. (2022). Electrified powertrain sizing for vehicle fleets of car makers considering total ownership costs and CO2 emission legislation scenarios. *Applied Energy*. 314. 118902. 10.1016/j.apenergy.2022.118902.
- [95] Fontaras, G., Ciuffo, B., Zacharof, N., Tsiakmakis, S., Marotta, A., Pavlovic, J. and Anagnostopoulos, K., The difference between reported and real-world CO2 emissions: How much improvement can be expected by WLTP introduction, In: World Conference on Transport Research, 10-15 July 2016, Shanghai, World Conference on Transport Research, 2017, ISSN 2352-1465, 25, p. 3933-3943, JRC104702.
- [96] Y. del Valle; G. K. Venayagamoorthy; S. Mohagheghi; J. Hernandez; R. G. Harley. Particle Swarm Optimization: Basic Concepts, Variants and Applications in Power Systems. in *IEEE Transactions on Evolutionary Computation*, vol. 12, no. 2, pp. 171-195, April 2008.
- [97] M. Lu, G. Domingues-Olavarria and M. Alakula, "Comparison of PMSM versus PMa-SynRM and IM from an Optimized Electric Vehicle Powertrain Perspective," 2023 26th International Conference on Electrical Machines and Systems (ICEMS), Zhuhai, China, 2023, pp. 4075-4080.
- [98] V. I. Patel and J. Wang, "Demagnetization assessment of 6-phase fractional-slot permanent magnet machines with low space harmonics under various fault conditions," in *Power Electronics, Machines and Drives (PEMD 2014)*, 7th IET International Conference on, 2014, pp. 1- 6.
- [99] V. I. Patel, J. Wang, and S. S. Nair, "Demagnetization Assessment of Fractional-Slot and Distributed Wound 6-Phase Permanent Magnet Machines," *Magnetics*, *IEEE Transactions on*, vol. 51, pp. 1-11, 2015.
- [100] G. Zhao, L. Tian, Q. Shen and R. Tang, "Demagnetization Analysis of Permanent Magnet Synchronous Machines under Short Circuit Fault," 2010 Asia-Pacific Power and Energy Engineering Conference, Chengdu, China, 2010, pp. 1-4.
- [101] A. Schonknecht, A. Babik, and V. Rill, "Electric powertrain system design of BEV and HEV applying a multi objective optimization methodology," *Transp. Res. Procedia*, vol. 14, pp. 3611–3620, 2016.
- [102] B. Falvy and M. Bryant, "Cross-platform electric powertrain optimisation for developing modular product families," *Drive System Design*, Leamington Spa, CV31 1NB, UK, 2021.

- [103] D. Lechleitner, M. Hofstetter and M. Hirz, “Cost Reduction of Electric Powertrains by Platform-Based Design Optimization,” IEEE Transportation Electrification Conference & Expo (ITEC), Chicago, IL, USA, 2020, pp. 139-146.
- [104] Clemente, M., Salazar, M., & Hofman, T, “Concurrent Design Optimization of Shared Powertrain Modules in a Family of Electric Vehicles,” IEEE Transactions on Transportation Electrification, early access.
- [105] G. Domingues-Olavarría, “From Specifications to Vehicle Demonstrator: System Optimization and Validation Process of an Integrated E-Drive Module,” BorgWarner Sweden AB, Aachen, Germany, Sustainable Mobility, Oct. 2020.
- [106] Xu, Yu & Kersten, Anton & Klacar, S. & Ban, Branko & Helling, J. & Sedarsky, David. (2023). Improved efficiency with adaptive front and rear axle independently driven powertrain and disconnect functionality. *Transportation Engineering*. 13. 100192. 10.1016/j.treng.2023.100192.
- [107] B. Sun, S. Gao, C. Ma, J. Li, System power loss optimization of electric vehicle driven by front and rear induction motors, *Int. J. Automot. Technol.* 19 (1) (2018) 121–134.
- [108] X. Yuan, J. Wang, Torque distribution strategy for a front-and rear-wheel-driven electric vehicle, *IEEE Trans. Veh. Technol.* 61 (8) (2012) 3365–3374.
- [109] Fujimoto, Hiroshi & Harada, Shingo. (2015). Model-Based Range Extension Control System for Electric Vehicles with Front and Rear Driving–Braking Force Distributions. *Industrial Electronics*, IEEE Transactions on. 62. 3245-3254. 10.1109/TIE.2015.2402634.
- [110] De Pinto, Stefano & Camocardi, Pablo & Sorniotti, Aldo & Gruber, Patrick & Perlo, Pietro & Viotto, Fabio. (2016). Torque-fill control and energy management for a 4-wheel-drive electric vehicle layout with 2-speed transmissions. *IEEE Transactions on Industry Applications*. PP. 1-1. 10.1109/TIA.2016.2616322.
- [111] M.V. Castro, S. Mukundan, C.L. Filho, G. Byczynski, B. Minaker, J. Tjong, N. Kar, Non-dominated sorting genetic algorithm-based determination of optimal torque–split ratio for a dual–motor electric vehicle. *IECON 2021 – 47th Annual Conference of the IEEE Industrial Electronics Society*, 2021, pp. 1–6.
- [112] X. Qi, Q. Wang, F. Xie, J. Cao, L. Chen, Q. Zhan, Researching of efficiency optimized torque distribution based on front and rear wheel independently drive electrical vehicle. 2016 19th International Conference on Electrical Machines and Systems (ICEMS), IEEE, 2016, pp. 1–6.
- [113] Z. Yang, J. Wang, G. Gao, X. Shi, Research on optimized torque-distribution control method for front/rear axle electric wheel loader, *Math. Probl. Eng.* 2017 (2017).
- [114] Electric Vehicle Database. <https://ev-database.org/>
- [115] C. Guo, C. Fu, R. Luo, G. Yang, Energy-oriented car-following control for a front- and rear-independent-drive electric vehicle platoon, *Energy* 257 (2022) 124732.

- [116] H.A. Yavasoglu, J. Shen, C. Shi, M. Gokasan, A. Khaligh, Power split control strategy for an EV powertrain with two propulsion machines, *IEEE Trans. Transp. Electrification*. 1 (4) (2015) 382–390.
- [117] Burrell, T A, Coomer, C L, Campbell, S L, Seiber, L E, Marlino, L D, Staunton, R H, and Cunningham, J P. Evaluation of the 2007 Toyota Camry Hybrid Synergy Drive System. United States: N. p., 2008. Web.
- [118] Gong, Yuancong & Gneiting, Andreas & Zhao, Chongshen & Parspour, Nejila. (2023). Comparative Study of Different Surrogate Models in the Multi-physics Optimization of Synchronous Reluctance Machine. 1284-1290. 10.1109/ICEMS59686.2023.10345114.
- [119] Luna, Ivan & Ribeiro, Bárbara & Santos, Stefan & Alarcon, Willy & Monteiro, J.R.B.A. (2023). Design Optimization of an Interior Permanent Magnet Synchronous Machine Applying the PSO Algorithm to a Surrogate Model Based on Artificial Neural Network. 1-6. 10.1109/SPEC56436.2023.10407848.
- [120] Tahkola, Mikko & Keränen, Janne & Sedov, Denis & Farzam Far, Mehrnaz & Kortelainen, Juha. (2020). Surrogate Modeling of Electrical Machine Torque Using Artificial Neural Networks. *IEEE Access*. 8. 220027 - 220045. 10.1109/ACCESS.2020.3042834.